6. Preparation of thin Pd and Pd/Ag Membranes on Porous Sintered Metal Supports via Alternate Synthesis Routes

6.1. Introduction

In order to achieve thin separation layers, the synthesis of composite Pd/Ag membranes throughout this dissertation work has been realized by the successful utilization of different methodologies including direct modification of the electroless plating process by the hole blowing technique and the use of novel grading techniques by gradual smoothing of the support metal surface via pre-activated alumina particles or an aluminum hydroxide, $Al(OH)_3$, solution.

Therefore, the main objective of the work described in this chapter is to provide detailed description and to understand fundamental concepts behind the different synthesis techniques used for the preparation of composite Pd and Pd/Ag membranes.

6.2. Annealing of thin Pd/Ag Multi-Layers formed by the Electroless Sequential Deposition

To evaluate the formation of Pd/Ag alloy layers, as well as the deposition morphology, a 2.4 μm Pd layer and a 0.75 μm Ag layer was formed sequentially by the

electroless deposition on a 0.5 µm media grade PSS support, which was oxidized at 400°C for 10 hours before the plating of the metals. The resulting Pd/Ag/PSS composite was annealed at 600°C for 10 hours in helium. Figure 6-1 shows a typical cross-section SEI micrograph of the sample after annealing.

The upper dark portion and lower gray regions in Figure 6-1 correspond to the phenolic mounting material and the PSS, respectively. The thin Pd and Ag layer lies between these two regions and is light gray in the micrograph. As can be seen from Figure 6-1, the Pd/Ag layer appeared to form a uniform thin layer on the PSS substrate, covering small gaps of the porous layer and even depositing into the large openings in the support, which ranged from 10-20 µm in width and 15-25 µm in depth.

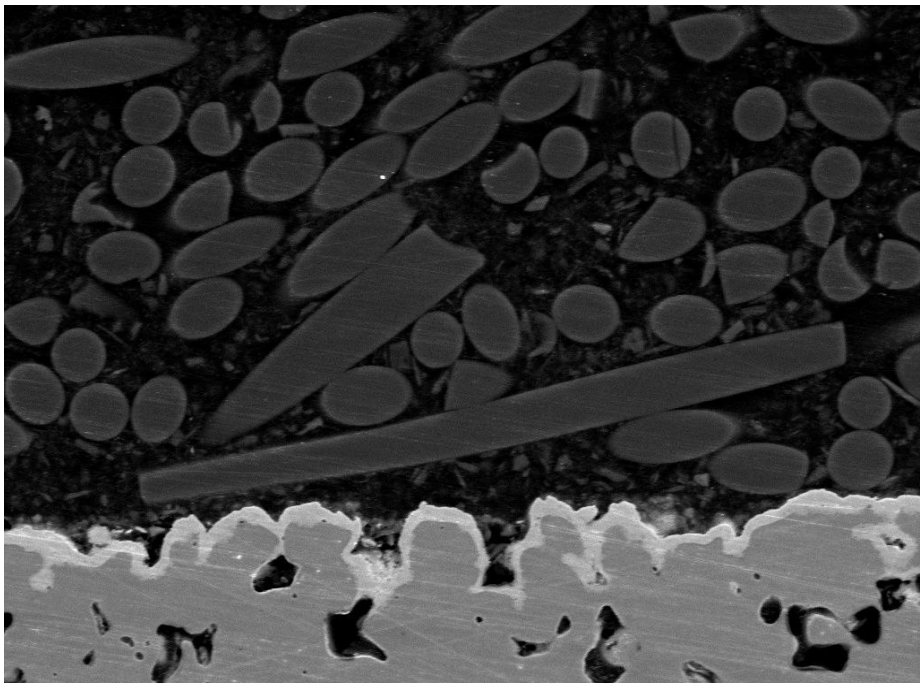

Figure 6-1: Cross-section view of Pd/Ag/PSS composite plate after annealing at 600°C in He for 10 hours (600X)

EDX spot scans were performed at various points in the layer to determine if a uniform alloy was produced by annealing at 600°C. Figure 6-2[a] shows the SEI micrograph of the annealed Pd/Ag layer in the region of a large pore opening in the support with indication of the location of several EDX spot scans. The elemental compositions of Pd, Ag and support metals (Fe, Ni and Cr) obtained from the spot scans

are presented in Figure 6-2[b]. Starting from spot number 1 in the upper left corner of Figure 6-2[a] and descending into the pore along the left wall to spot number 4, the EDX spot scans indicated a steady decrease in Ag content and a steady increase in Pd. Indeed, the three spots located in the deepest section of the large pore (spots 4, 5 and 6) in Figure 6-2[b] had almost no Ag, indicating that Ag was not deposited inside the pores and openings during electroless plating.

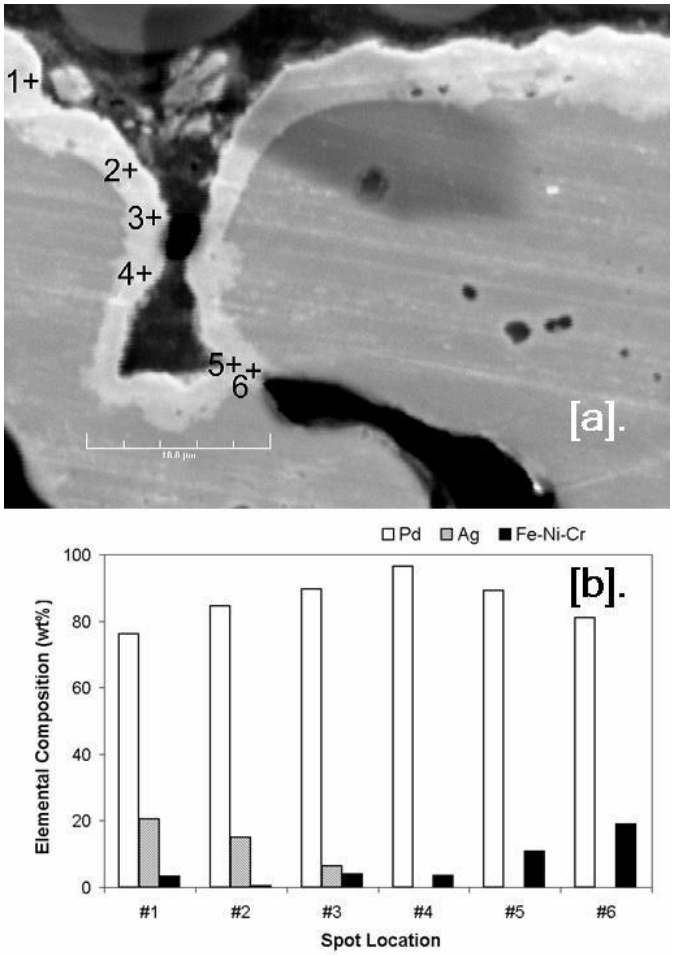

Figure 6-2: [a]. SEI micrograph for the annealed Pd-Ag layer in the region of a large pore opening in the support at 3kX (Locations for EDX spot scans were annotated by numbered crosses) [b]. EDX spot scan compositions for points indicated in [a] (Data for the support metals is the sum of the compositions for Fe, Ni and Cr)

An additional point of interest in Figure 6-2[a] is the small pore opening at the bottom right of the larger pore, which appears to have been closed in the plating process. The amount of the diffusion of the support metals (Fe, Ni and Cr) into this region (spots 5 and 6) appeared to be greater than that in the other regions as shown in Figure 6-2[b]. This

might have resulted from the fact that this region had support walls in close proximity on all but two sides. It was noted by Ma *et al.* (2004a) that the *in-situ* oxidation process at relatively mild temperatures (i.e., 400°C) led to an oxide coverage that was predominantly on and near the surface of the support and too thin to be detected by the SEI micrographs. Therefore, it is also possible that the oxide coverage in this small pore (spots 5 and 6 in Figure 6-2[a]) beneath the surface was insufficient to protect the Pd/Ag alloy layer from the intermetallic diffusion in these locations. During testing at high temperatures, an apparent increase in the intermetallic diffusion at these points could significantly reduce the hydrogen permeability.

While detailed microstructure analysis discussed in Chapter 5 indicated that the "Ag directed" electroless deposition morphology led to the formation of 5-20 μm thick dendritic clusters that grew perpendicular to the surface, the heterogeneous nature of the sequential Ag deposition process resulted in a poor deposition at the pore mouths and valleys, which causes compositional variance and might present an additional challenge to attaining a homogeneous Pd/Ag alloy membrane on porous sintered metal supports.

6.3. Hole Blowing Technique (HBT)

Since the conventional plating of Ag produces a heterogeneous rough surface coverage and non-uniform and thick deposition layers due to the dendritic cluster growth, the concept of blocking the large pores on the surface of the support metal by simply taking advantage of the dendritic growth characteristics of the Ag clusters, was utilized as an alternate synthesis route to form thin Pd/Ag layers with uniform compositional distribution within the membrane layer. Therefore, the main objective of the Hole Blowing Technique (HBT) was to selectively deposit Pd and Ag metals by targeting only the pore mouth and valleys that narrows to 1-3 μm wide at a depth of 20-30 μm from the outer surface of the metal support. This was attained by processing both the activation and plating solutions, particularly Ag, through the tube-side of the membrane support by the use of pressurized air.

It should be noted that the HBT is not a surface modification technique. Instead, HBT was initially exploited to enrich Ag composition within the pores of the support metal to

achieve uniform distribution of Pd and Ag metals and specifically to avoid dendritic cluster growth on the surface of the support. However, HBT was effective in partial blockage of the support pores as evidence by the cross-sectional SEI micrographs.

The pressurized air source required for the HBT process was supplied by an industrial grade air tank through a Tygon tube connection and attached to the support tube with a stainless steel adapter having a 1" to ½" Swagelok reducing union. A typical synthesis via HBT consisted of three loops of activation, two loops of Ag and/or Pd plating, followed by the regular Pd and/or Ag plating. During HBT, both the activation and plating solutions were admitted and processed in part from the tube-side of the membrane support (~15 mL for ½" OD supports). In order to avoid chloride contamination from the activation solutions ($SnCl_2$, $PdCl_2$ and HCl), the membrane was excessively rinsed with the DI H_2O both from shell and tube sides by immersing the membrane assembly into a DI H_2O reservoir (i.e., beaker, graduated cylinder, etc). Once all the fluid contained in the tube-side was forced with the pressurized air through the pores of the support into the shell-side filled with DI H_2O, the solution during intermediated rinsing steps appeared to look as boiling water. Since only the pore mouths and valleys were targeted during the activation via HBT, the porous surface of the support was patchy in appearance due to the partial seeding with the Pd^{2+} nuclei. Following activation, Ag and/or Pd plating solution, which was pre-heated to 60°C in a constant temperature water bath, the tube-side was activated by the similar procedure described for the activation steps. Similar to the intermediate DI H_2O rinsing step for the HBT activation, the membrane was dipped into the used HBT plating solution for a duration of 1-2 minutes, which was collected in a beaker. This final step was utilized to allow further plating at the target pore mouths, as well as to seed the non-activated top surface of the porous support in order to shorten the induction period for the following plating step. Finally, the membrane was thoroughly rinsed with a pre-heated DI H_2O (60°C).The HBT Ag and/or Pd plating was repeated twice. The HBT activation and plating procedure is schematically illustrated for the Ag metal (HBT-Ag) in Figure 6-3[a].

After HBT, regular Ag and/or Pd was deposited sequentially for 90-120 minutes to allow consolidation between the HBT Ag and/or Pd and the regular electroless deposition

morphology, as schematically illustrated in Figure 6-3[b]. Then the membrane was dried at 120°C overnight prior to room temperature helium permeance test. The complete synthesis process, including the regular electroless Ag and/or Pd plating, was termed as the HBT-Ag and/or HBT-Pd depending on which plating solution was processed from the tube-side of the support metal. In addition, the HBT synthesis usually included an intermediate annealing step, which was conducted at 600°C in helium for 10-20 hours and a surface polishing step with a 600-grid SiC paper prior to the application of a dense Pd layer.

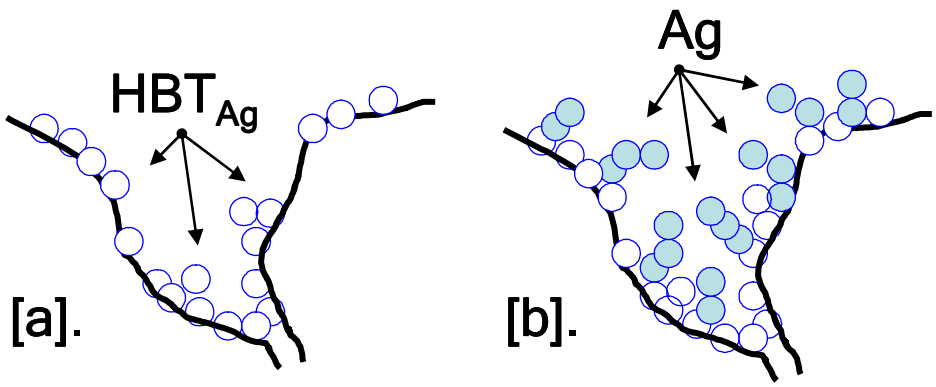

Figure 6-3: Schematic representation of the [a]. Activation and Ag plating via HBT and [b]. Regular Ag plating after HBT

The synthesis of composite Pd/Ag membranes via the HBT was usually accomplished at a reduced number of synthesis steps compared to that of regular electroless plating and bi-metal multi-layer (BMML) deposition procedures. The HBT synthesis step resulted in the formation of a relatively thin Pd/Ag layers below ~7 µm, accompanied with a large reduction in the room temperature helium permeance of the support indicating partial blockage of the large surface pores. Figure 6-4 shows the % change of He permeance with respect to the initial permeance of the bare and/or oxidized support as a function of deposition thickness estimated gravimetrically during synthesis. It should be noted that the additional synthesis steps in Figure 6-4 for the HBT membranes are not shown for the simplicity of comparison. While HBT-Ag plating on ½" OD supports resulted in Ag-rich Pd/Ag layers as thin as 2-4 µm with ~60% reduction in support permeance, HBT-Pd plating on 1" OD, 6" long supports formed 6-7 µm thick Pd-rich Pd/Ag layers with a reduced permeance as high as ~85% (Figure 6-4). Any variation in the thickness and the

reduced He permeance data for the HBT layers were originated from the changes in the support grades (0.1-0.5 µm) and the different electroless Pd and/or Ag plating times used for the final consolidation step. In the case of regular electroless plating and BMML deposition, a similar decline in the support permeance (~60% or higher) was observed only after depositing 25 µm or thicker layers of Pd/Ag, as shown in Figure 6-4. Although additional Pd plating was required to achieve a dense membrane, the final thickness of the composite Pd/Ag membranes prepared via the HBT were in the order of 15-25 µm with variable Ag content in the range of 2-20 wt%.

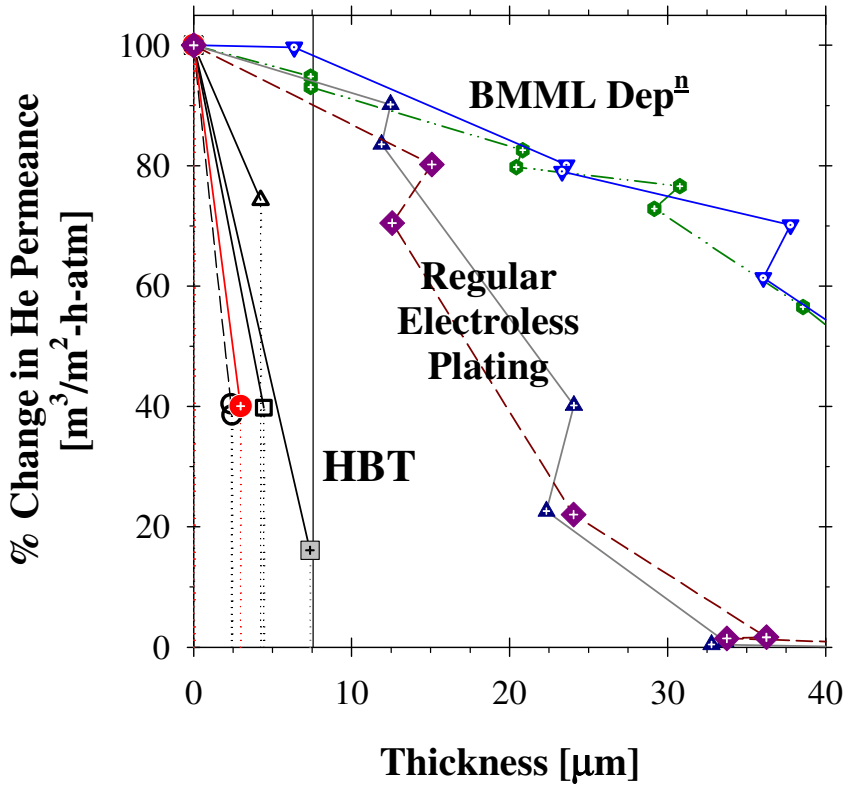

Figure 6-4: Normalized He permeance (%) vs. deposition thickness for the composite Pd/Ag membranes formed by the HBT, regular electroless plating and BMML deposition (Additional synthesis steps for the HBT membranes are not shown for the clarity of comparison)

6.3.1. Microstructure Analysis of the Pd/Ag Layers formed by the HBT

The morphology of the Pd/Ag layers resulting from the HBT was investigated on a 0.2 µm media grade un-oxidized PSS support (½" OD and 1" long).

The thickness of the Pd/Ag layer formed after the 1st HBT-Ag step was 2.4 µm and showed a 62% decline in the initial He permeance of the support after annealing the Pd/Ag/PSS composite (labeled as E_t001) at 600°C for 10 hours in He. In order to check the re-producibility of the HBT process, a 2nd HBT-Ag run was conducted without activating the outer top surface of the E_t001 membrane. Similarly, the Pd/Ag/PSS composite was annealed at 600°C for 10 hours in He. The final thickness of the E_t001 membrane was 5.6 µm and the % change in the He permeance was ~98%, indicating an almost gas-tight Pd/Ag layer. Then, the Pd/Ag/PSS composite (labeled as E_t001) was cut into sections, mounted and polished for the SEI and EDX analyses.

The cross-sectional SEI micrographs of the E_t001 membrane shown in Figure 6-5 indicated that the thin Pd/Ag layers formed by the HBT was relatively uniform, in which the thickness of 5.6 µm estimated gravimetrically was in good agreement with the average thickness shown in the micrographs. Since the 2nd HBT-Ag run proceeded without activating the top surface of the 1st HBT-Ag layer, the interface between the two HBT runs was clearly visible in all the micrographs shown in Figure 6-5. Yet, Figure 6-5[c] indicated that the Pd/Ag layer formed by the 2nd HBT-Ag run was loosely attached to the underlying HBT layer due to the poor surface activation. It was also interesting to note that the large pore gaps in close proximity to the support surface were not blocked by the presence of Pd and/or Ag deposits, as shown in Figure 6-5[a] and [b]. As evidenced by the cross-sectional SEI micrographs in Figure 6-5, it was confirmed that the HBT was effective for the synthesis of thin Pd/Ag layers by selectively depositing Pd and/or Ag metals only at the targeted pore mouths and valleys of the support.

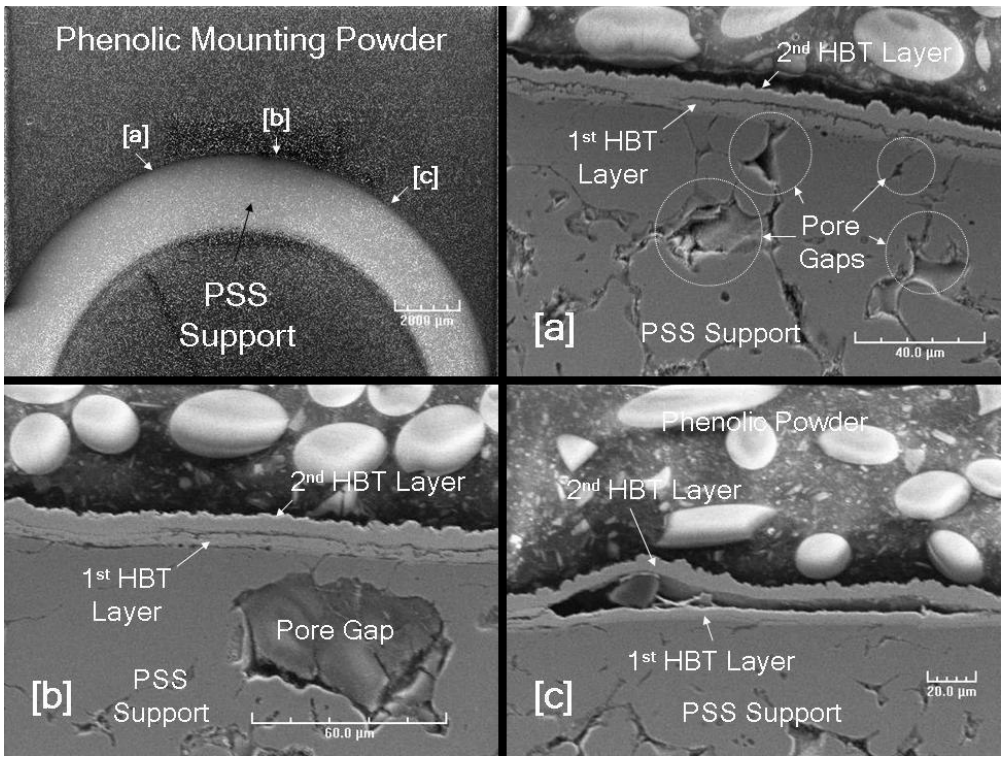

Figure 6-5: Cross-sectional SEI micrographs of the HBT membrane Et001

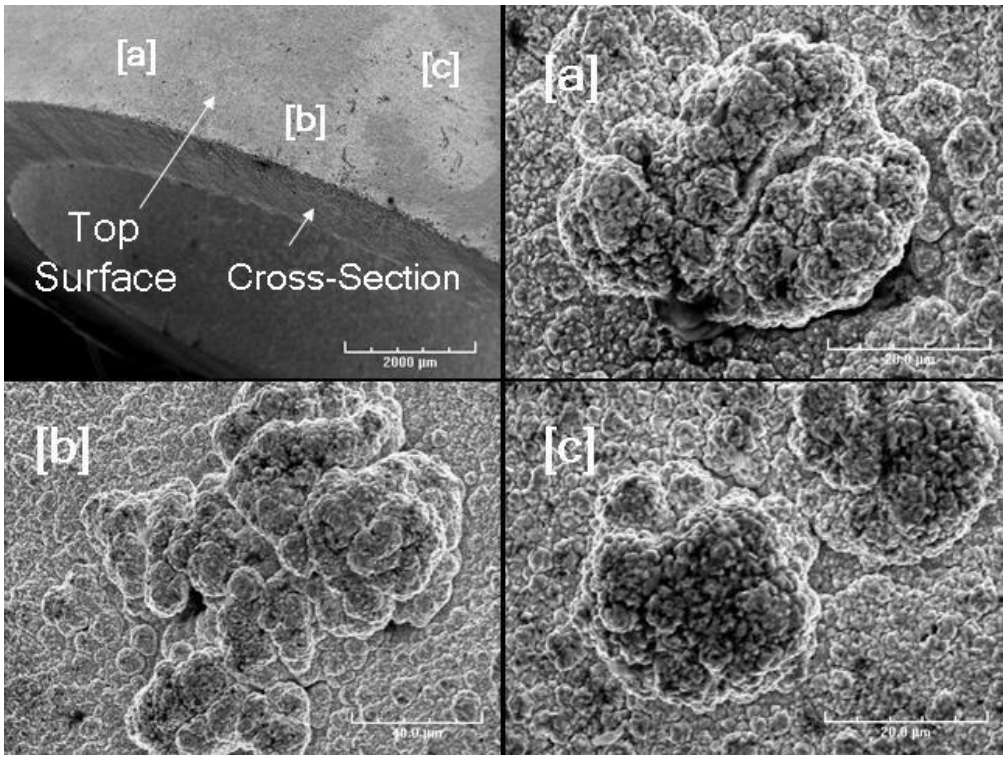

Figure 6-6: Top-view SEI micrographs of the HBT membrane Et001

The top surface SEI micrographs shown in Figure 6-6 revealed the presence of cauliflower-like clusters, which were as large as 40-120µm and appeared to be randomly distributed throughout the entire surface. It is most likely that the activation and Ag plating solutions processed through the tube-side by the use of pressured air during the 2nd HBT-Ag run, followed the path through the pore openings that were not liquid dense at the end of 1st HBT-Ag run. Therefore, the formation of large cauliflower-like deposits was attributed to the accumulation of the plating solutions at the regions in the likelihood proximity to the large pores of the support surface.

Given the size of the cauliflower-like surface deposits, it should be also noted that the polishing of the surface may be necessary prior to further plating steps in order to smoothen the surface topology and to avoid additional growth of the large clusters shown in Figure 6-6[a]-[c].

In addition, the EDX spot scans conducted both at the top-surface and along the cross-section of the membrane E_t001 gave an estimate for the average surface composition of Pd and Ag as 70-80 wt% and 20-30 wt%, respectively.

Furthermore, Figure 6-7 shows the cross-sectional SEI micrographs for a 24.4 µm thick Pd/Ag membrane (E_t002) formed by the HBT-Ag on a 0.5 µm media grade PSS support. Unlike membrane E_t001, E_t002 membrane was characterized in H_2 for 2450 hours over a temperature range of 275-500°C.

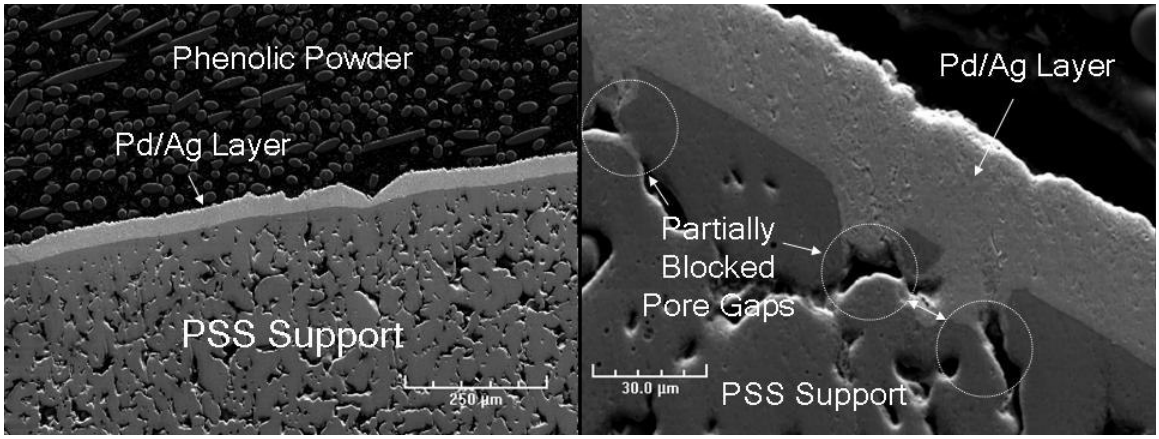

Figure 6-7: Cross-section morphology of the E_t002 membrane after H_2 permeation test

The average thickness of the Pd/Ag layer estimated from the SEI micrographs given in Figure 6-7 was ~30-32 µm, which was in fairly good agreement with the thickness estimated gravimetrically for the E_t002 membrane. As can be depicted in Figure 6-7, the thickness of the Pd/Ag layer formed by the HBT-Ag was uniform along the support surface. Finally, the top surface SEI micrographs in Figure 6-8 shows the likelihood location of a large surface pore, which was effectively blocked initially by the HBT-Ag and during the additional electroless Pd plating to achieve a dense membrane layer.

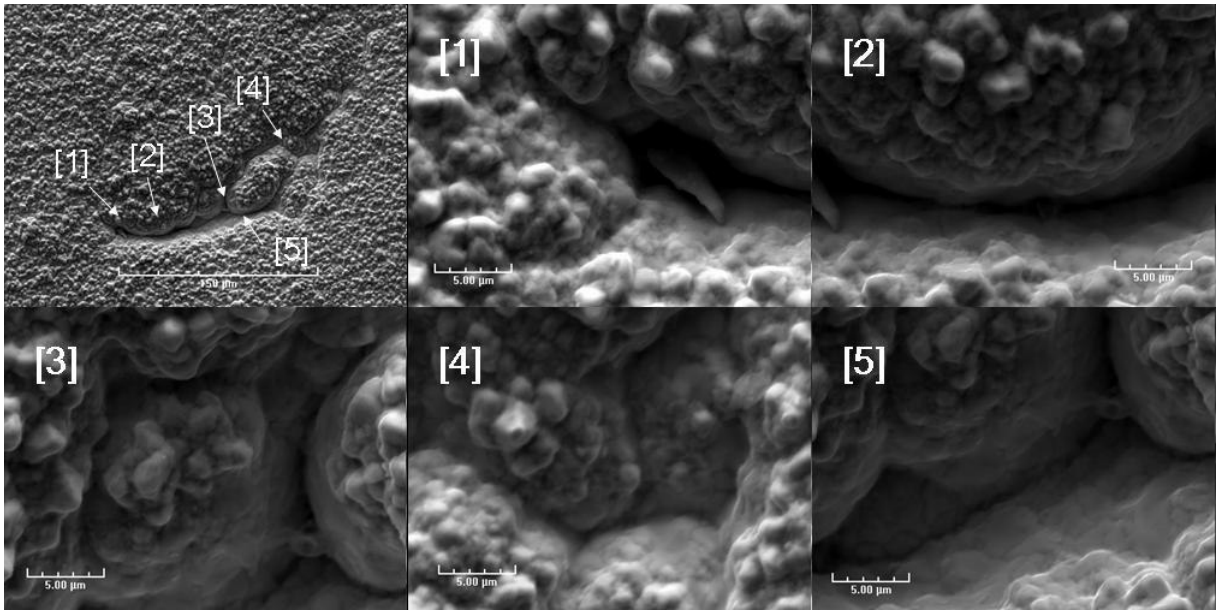

Figure 6-8: Surface morphology of the E_t002 membrane

The hole-blowing technique (HBT) was used for the synthesis of the composite Pd/Ag membranes E_t001, E_t002, E_t003, E_t004, E_t005, 004, 010 and 007 (Ma-33). The characteristics of the HBT membranes along with all the other composite Pd and Pd/Ag membranes prepared in this dissertation are summarized in Table 3-5.

6.4. Modification of the Porous Support Surface for the Synthesis of Composite Pd/Ag Alloy Membranes

6.4.1. Pre-Activated α-Al_2O_3 Particles

The use of pre-activated (Pd seeded) alumina particles for the gradual smoothing of the metal support surface, a surface modification technique developed in our group (Ma and Guazzone, 2006), consists of depositing coarse, fine and ultra-fine alumina particles in order to narrow the surface pore size distribution of the support metal and to allow for the formation of thin Pd and Pd/alloy layers.

Coarse, fine and ultra-fine Al_2O_3 particles, used to modify the porous support surface, were powder mixtures with different particle sizes. The coarse powder mixture consisted of 65 wt%, 30 wt% and 5 wt% Al_2O_3 with average particle sizes of 1 μm, 5 μm and 3 μm, respectively and used as-is. However, the fine powder mixture was pre-activated with a single loop of $SnCl_2$-$PdCl_2$ solutions in an ultrasonic bath at 60°C and consisted of 60 wt%, 30 wt% and 10 wt% Al_2O_3 with average particle sizes of 0.3 μm, 3 μm and 1 μm, respectively. Similarly, pre-activated ultra-fine powder mixture included 60 wt%, 30 wt% and 10 wt% Al_2O_3 with average particle sizes of 0.01-0.02 μm, 1 μm and 0.3 μm, respectively.

The grading of the porous support surface via the deposition of the pre-activated Al_2O_3 powder mixtures from a 200 mL water slurry (pH=2) containing 0.5 g of the powder mixture was accomplished by applying vacuum from the tube-side. The excess cake formed on the surface of the support was removed by gloved hands while gently rinsing with the DI H_2O after each deposition stage. The intermediate Pd plating (5-15 minutes), used to consolidate (glue) the Al_2O_3 powder layers in the original procedure, was replaced with electroless Ag plating that lasted for 5-15 minutes. Finally, the graded support was dried at 120°C overnight, then, weighed and tested at room temperature at different pressures to determine the He permeance of the modified support. According to Guazzone (2005), successful utilization of the above steps would yield a graded support similar to the cross-sectional SEI micrograph shown in Figure 6-9.

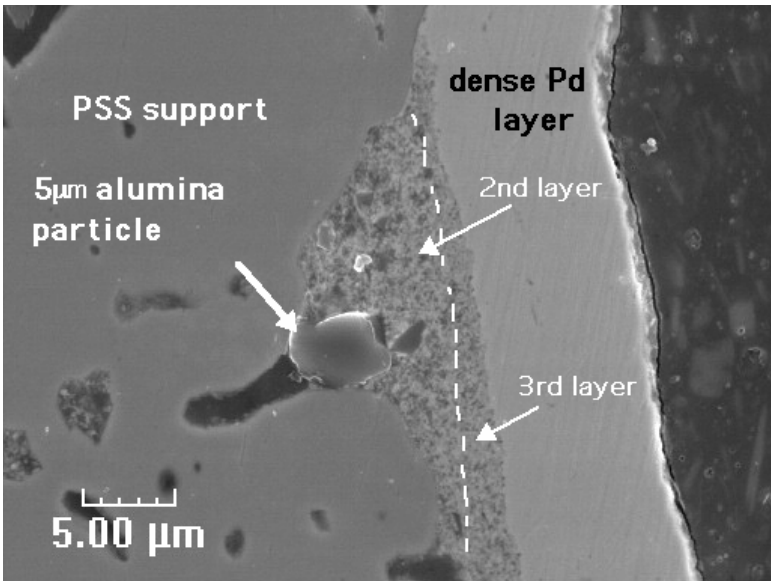

Figure 6-9: Structure within a pore achieved by sequential deposition of coarse, fine and very fine pre-activated powders (Guazzone, 2005)

The modification of the support surface via the pre-activated Al_2O_3 particles was used for the synthesis of membrane 013 (Ma-46) as shown in Table 3-5.

6.4.2. $Al(OH)_3$ Grading

The use of aluminum hydroxide as a filler material for the modification of the porous metal support surface was first introduced by Tong and Matsumura (2004). The original procedure reported by Tong and Matsumura (2004) consisted of precipitating aluminum hydroxide, referred to as "aluminum hydroxide sol and/or gel", from an aqueous solution of 0.4M aluminum nitrate by adding 0.6M ammonium carbonate at room temperature. The precipitate was either used as-is (Tong and Matsumura, 2004) or after suspending the as-prepared aluminum hydroxide sol in a commercial activation solution (Okuno Chem. Ind., Co) at a 9:1 volume ratio with stirring for 3 hours followed by another 3 hours of ultrasonic bath treatment (Tong *et al.*, 2005d; Tong *et al.*, 2005e). Then, the surface of the porous support was modified with the aluminum hydroxide sol in an ultrasonic bath for 2 hours under vacuum suction from the tube-side of the support. The surface modification was completed after an additional hour of vacuum suction until the support tube filled with the aluminum hydroxide was liquid dense. The excess filling material on the surface was removed by rinsing with distilled water.

The aluminum hydroxide powder for the preparation of grading solutions used in this study was purchased from Fisher Scientific, which was in the hydrated form, $Al(OH)_3.xH_2O$, with a maximum water content of 32.4% and a density of 2.42 g/cm^3.

The methodology used for the grading of the porous support surface was accomplished by the use of two different $Al(OH)_3$ solutions, namely regular and concentrated. The regular $Al(OH)_3$ grading solution was prepared by dissolving 16 g of powder in 1L of DI H_2O and 1mL of 1M HCl solution. Similar to the procedure described by Tong and Matsumura (2004), the 0.2M $Al(OH)_3$ solution was kept in an ultrasonic bath for 1 hour and stirred mechanically for an additional 1-2 hours. The grading of the porous support was conducted by applying vacuum from the tube-side with constant stirring of the $Al(OH)_3$ solution for 20-45 minutes. The excess filling material on the surface was removed by gloved hands while rinsing with DI H_2O. The regular $Al(OH)_3$ grading procedure was only utilized for the synthesis of composite Pd/Ag membranes 014 and 015, as shown in Table 3-5.

The modified $Al(OH)_3$ grading procedure consisted of preparing a dense $Al(OH)_3$ slurry and applied at a reduced number of synthesis steps for the preparation of composite Pd and Pd/Ag membranes 016 to 025 listed in Table 3-5. The modified $Al(OH)_3$ grading solution was prepared by dissolving 5 g of powder in 40 mL of DI H_2O and 1mL of 1M HCl solution in a 50 mL vial for the ½" OD supports with 20-25 cm^2 plating area. For 1" OD supports, the grading was carried out in graduated cylinders by maintaining a $Al(OH)_3$ grading solution volume to plating area ratio of ~2. Then the support tube was immersed into the $Al(OH)_3$ slurry twice for only 2 minutes while applying vacuum form the tube-side. Then, an additional 1 minute suction was employed to ensure that the graded support was liquid dense. Between each dipping, the $Al(OH)_3$ slurry was shaked thoroughly to avoid particles settling down at the bottom of the grading vial and/or graduated cylinder. The excess $Al(OH)_3$ cake formed on the porous surface of the support resembled to that of a "shaving cream" due to its dense and foam-like texture. Upon the successful completion of the aforementioned steps, the excess cake on the surface was removed either by gloved hands while rinsing with DI H_2O or with a bristle brush after drying at 120°C for 2-4 hours. Finally, the surface modified support was placed in a

constant temperature plating bath for the electroless deposition of Pd and/or Ag. It should be also noted that the $Al(OH)_3$ grading did not include any intermediate Pd and/or Ag plating to consolidate (glue) the powder such as the pre-activated Al_2O_3 grading technique discussed in Section 6.4.1. In order to avoid long induction times at the beginning of the electroless plating reaction, all the support tubes (oxidized and/or un-oxidized) were activated 6 times by the regular $SnCl_2$-$PdCl_2$ cycle prior to the surface modification with the $Al(OH)_3$ particles.

Typical cross-sectional SEI micrographs for the $Al(OH)_3$ surface modified supports of the Pd/Ag membranes 017 and 014 are shown in Figure 6-10[a] and [b], respectively.

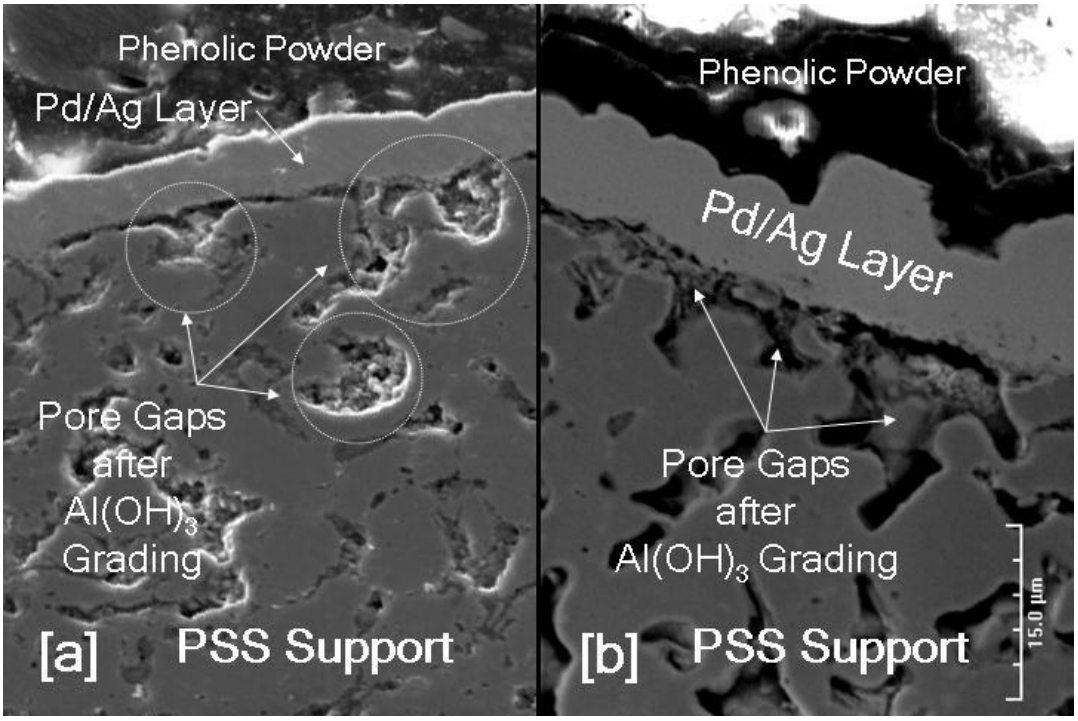

Figure 6-10: The cross-sectional SEI micrographs for the membranes [a]. 017: ~4.6 µm thick Pd/Ag (31.3 wt% Ag) and [b]. 014: ~10 µm thick Pd/Ag (30.6 wt% Ag) on $Al(OH)_3$ modified 0.1 µm media grade Inconel supports

6.4.2.1. Characterization of $Al(OH)_3$ Phase Transformations via FT-IR Spectroscopy and X-Ray Diffraction

Since the surface modification of the porous metal supports $Al(OH)_3$ was essentially preferred over ZrO_2, SiO_2 and CeO_2 particles due to the low residual volume of $Al(OH)_3$ at high temperatures (Tong *et al.*, 2005e), this section is aimed at understanding the effect of temperature on the properties of $Al(OH)_3$ via gravimetric, XRD and FT-IR analyses.

For this purpose, three sample sets were prepared; as-received $Al(OH)_3$ powder, a 1.6 M $Al(OH)_3$ solution aged for 6 months and a freshly prepared 1.6 M $Al(OH)_3$ solution, which were designated as sample solutions A, B and C, respectively. The excess liquid for the samples B and C were filtered prior to further analysis. Then, samples from each set were dried in air at 120°C, 350°C and 500°C for 16 hours. Figure 6-11 shows the % weight change data for the $Al(OH)_3$ samples as a function of drying temperature.

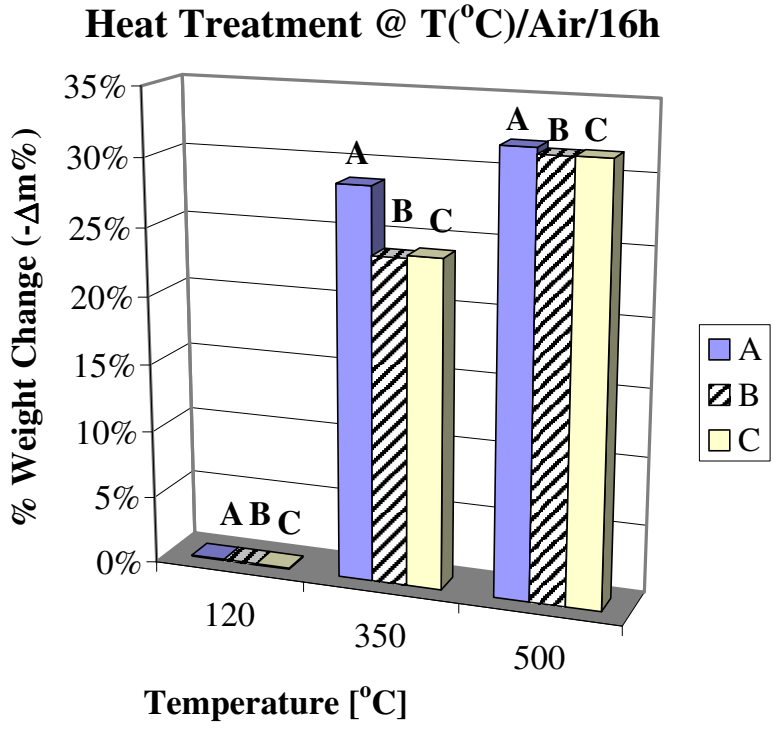

Figure 6-11: % Weight change of $Al(OH)_3$ samples after heat treatment

As shown in Figure 6-11, there were no significant changes in the sample weights after drying at 120°C. The maximum % weight change was 0.009 wt% for all the samples

A, B and C. On the other hand, drying at 350°C for 16 hours resulted in a noticeable change in the order of 28.7 wt%, 23.8 wt% and 24.1 wt% for the samples A, B and C, respectively. Finally, the % weight change of samples A, B and C was 32 wt%, 31.6 wt% and 31.6 wt%, respectively, after drying at 500°C for 16 hours. Since the $Al(OH)_3$ powder, purchased from Fisher Scientific, was in the hydrated form, $Al(OH)_3.xH_2O$ with a maximum water content of 32.4%, the gravimetric analysis of the samples A, B and C indicated that the $Al(OH)_3$ powder lost all the absorbed water after drying at 500°C.

Figure 6-12 shows the XRD patterns both for the $Al(OH)_3$ powder and the samples dried at 120°C for 16 hours. The $Al(OH)_3$ powder used for the grading of the porous metal supports was identified as the Gibbsite phase with a monoclinic crystal structure, as can be depicted in Figure 6-12.

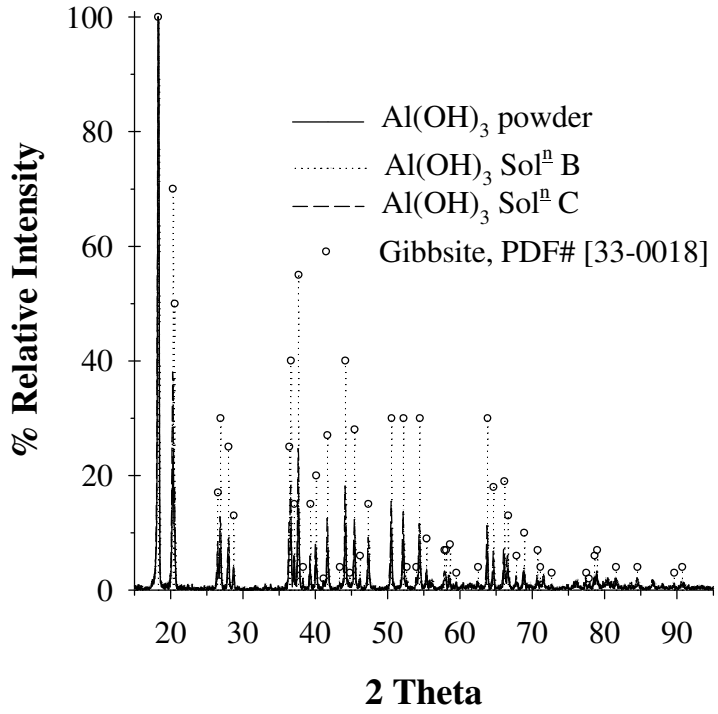

Figure 6-12: XRD patterns for the $Al(OH)_3$ powder and the samples B and C after drying at 120°C for 16 hours

Furthermore, Figure 6-13 shows the XRD patterns for the $Al(OH)_3$ powder (Sample A) at room temperature and after drying at 120°C, 350°C and 500°C for 16 hours. Since the samples B and C have produced exactly the same XRD pattern as for the sample A, the XRD patterns for samples B and C were not shown in Figure 6-13 for the clarity of comparison.

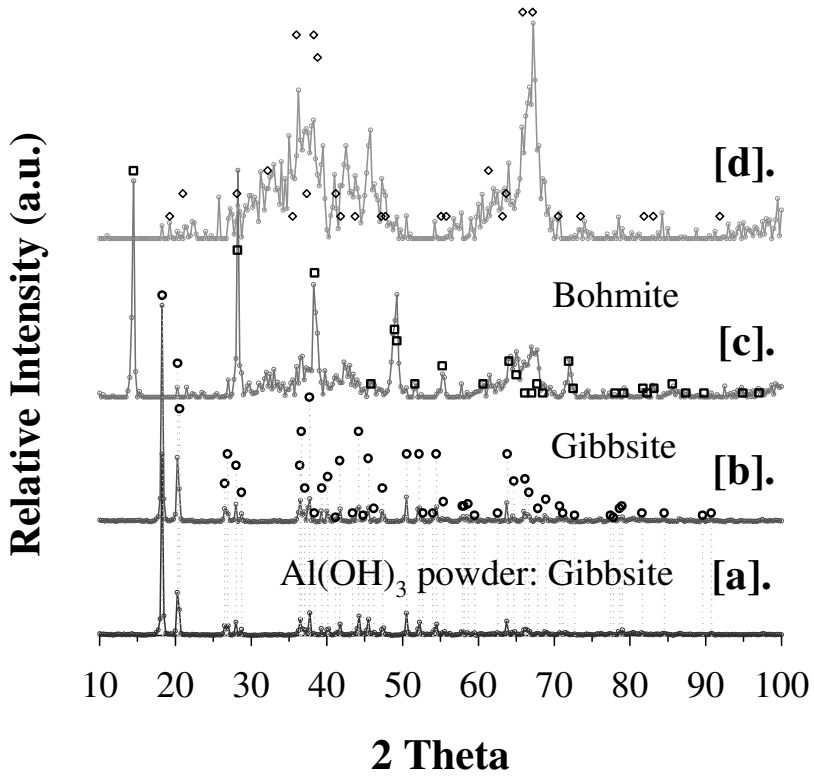

Figure 6-13: XRD patterns for the $Al(OH)_3$ powder at [a]. RT, and after 16 hours of drying at [b]. 120°C, [c]. 350°C and [d]. 500°C

As can be depicted from Figure 6-13, the XRD pattern for the $Al(OH)_3$ powder dried at 350°C indicated the formation of a Bohmite phase. The Bohmite phase of $Al(OH)_3$ was identified with a orthorhombic crystal structure and represented by the molecular formula of AlO(OH). After drying at 500°C, the $Al(OH)_3$ powder transformed to a relatively amorphous phase as shown by the significant broadening of the characteristic peaks. According to the XRD pattern shown in Figure 6-13, the transformation at 500°C was not

complete and indicated the co-existence of both the Akdalaite and Bohmite phases. The Akdalaite phase of $Al(OH)_3$ was identified with a hexagonal crystal structure and has the molecular formula of $(Al_2O_3)_4.H_2O$.

To thoroughly understand the $Al(OH)_3$ phase transformations at high temperatures, the FT-IR spectroscopy was used to monitor the changes in the structural OH groups of $Al(OH)_3$ Gibbsite phase. Since the powder samples can be easily analyzed without the preparation of KBr pellets, all the FT-IR measurements were performed in the attenuated total reflectance (ATR) mode. The ATR spectra for the $Al(OH)_3$ powder samples at room temperature and after drying at 120°C, 350°C and 500°C for 16 hours are shown in Figure 6-14.

As shown in Figure 6-14[a] and [b], ATR spectra of the gibbsite crystal structure revealed two distinct types of OH groups due to the absorbed water and to the presence of structural and surface OH groups between 3660-2800 cm^{-1}. The OH group due to the absorbed H_2O was located at the 3615 cm^{-1} band. On the other hand, the structural and surface OH groups were represented by three vibrational ν(OH) stretching bands located at 3356, 3424, and 3518 cm^{-1}. The ATR band located at 1730 cm^{-1} was identified as the H-O-H bending of the absorbed water, which was formed due to the humidity of the samples at room temperature working conditions. Similarly, the ATR bands located between 1390-1150 cm^{-1} were due to the presence of the interlayer carbonate and/or any other surface impurities. Finally, AlO bands were identified at 1130-885 cm^{-1}. All the characteristic ATR bands shown in Figure 6-14 were in good agreement with the similar observations reported in literature (Frost *et al.*, 1999; Wang and Johnston, 2000).

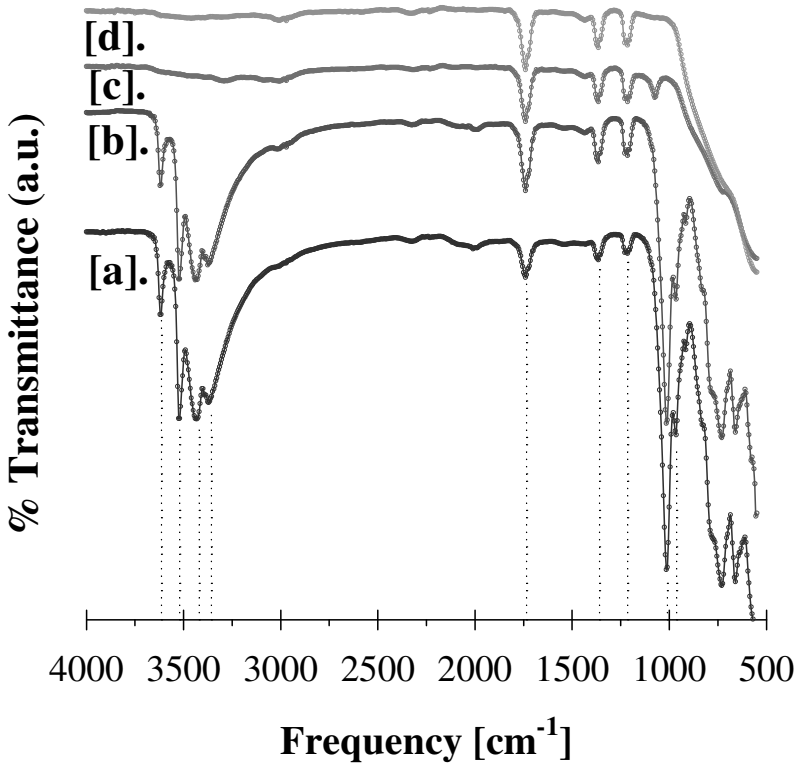

Figure 6-14: ATR spectra for the $Al(OH)_3$ samples at [a]. Room temperature and after heat treatment at [b]. 120℃, [c]. 350℃ and [d]. 500℃ for 16 hours

The OH bands representing both the absorbed water and the structural and surface OH groups (3660-2800 cm^{-1}) in Figure 6-14[a] and [b] were disappeared after drying at 350°C and 500°C. The disappearance of the OH bands located at 3660-2800 cm^{-1} was in good agreement with the % weight change data given in Figure 6-11. After drying at 350°C the shoulders of the AlO bands located at 963 and 910 cm^{-1} in Figure 6-14[c] were disappeared in agreement with the formation of a Bohmite (AlO(OH)) phase as shown by the XRD pattern in Figure 6-13. Finally, the disappearance of the AlO band at 1010 cm^{-1} in Figure 6-14[d] was observed after drying at 500°C. As shown in Figure 6-13 further transformation at 500°C was due to the co-existing Akdalaite ($(Al_2O_3)_4.H_2O$) and Bohmite (AlO(OH)) phases.

The transformation of the $Al(OH)_3$ from Gibbsite to Bohmite and to Akdalaite with the increasing temperature resulted in the formation of different crystal structures each exerting different physical properties. The densities for the Gibbsite, Bohmite and Akdalaite phases were reported as 2.34, 3.05 and 3.68 g/cm^3, respectively[*]. As shown by the detailed FT-IR and XRD analyses, the phase transformation of $Al(OH)_3$ from Gibbsite to Akdalaite resulted in the formation of a denser structure at high temperatures (350-500°C). From the standpoint of support surface modification with the use of $Al(OH)_3$, and in comparison to the pre-activated Al_2O_3, ZrO_2, SiO_2 and CeO_2 particles, the effect of mass transfer resistance is expected to be less pronounced for $Al(OH)_3$ due to its low residual volume at high temperatures.

[*] http://webmineral.com/

7. Microstructure Analysis of the Intermetallic Diffusion Induced Alloy Phases in Composite Pd/Ag/Porous Stainless Steel (PSS) Membranes

7.1. Introduction

The development of effective barrier layers against the intermetallic diffusion is of great importance for the porous sintered metal supports since high annealing temperatures and/or longer duration times are required to achieve uniform alloy layers of Pd and Ag metals formed by the electroless plating. Since the deposition morphology and the topological features of the electrolessly formed Pd and Ag deposits on PSS vary considerably (Ma *et al.*, 2004a), it is essential to develop a better understanding on the surface interactions and the phase changes between the Pd and Ag metals and the PSS substrate, especially upon high temperature annealing to form uniform alloy layers. The objective of this chapter is twofold: to investigate the effectiveness of different intermetallic diffusion barriers (i.e., *in-situ* oxide layer, Pd/Ag barrier) and their effects on the hydrogen permeance and more importantly, to study the intermetallic diffusion driven microstructure formation at the interface between the support metal and the Pd and Ag layers in the absence of a barrier layer (Ayturk *et al.*, 2007).

7.2. Results and Discussion

7.2.1. Intermetallic Diffusion and Composite Pd/Ag/PSS Membranes

The effect of intermetallic diffusion on the overall performance of composite Pd and Pd/Ag membranes has been discussed in Chapter 5 (e.g., Figure 5-2).

The *in-situ* oxidation technique (Ma *et al.*, 2000) has been successfully utilized to obtain stable hydrogen permeances over a limited temperature range (max., 400-450°C) with oxidation temperatures strongly depending on the support properties. On the other hand, the porous Pd/Ag barrier layer formed by the BMML deposition technique (Ma *et al.*, 2007) has provided excellent thermal stability against the intermetallic diffusion not only at 500°C but at temperatures as high as 600°C (Figure 5-4). Although the intermetallic diffusion may still occur between the porous metal support and the Pd/Ag barrier, it is interesting to note that the unique deposition morphology of the porous Pd/Ag barrier layer acted as a trap and prevented further diffusion of the Fe, Ni and Cr from the PSS support into the hydrogen selective Pd layer (Ayturk *et al.*, 2006). Indeed, the porous Pd/Ag barrier layer may even enhance the permeability of this layer, if a Pd/Ag alloy is formed. The unique deposition morphology of the Pd/Ag barrier necessitates a better understanding of the possible relationship between the intermetallic diffusion and the Pd and Ag deposition morphology formed by the electroless plating technique.

The characteristics of the morphology formed by the electroless deposition of Pd and Ag metals have been previously discussed in Chapter 5. It is well recognized that the electroless Ag plating leads to a heterogeneous rough surface coverage (Shu *et al.*, 1993; Cheng and Yeung, 1999; Keuler *et al.*, 1999b, 1999a; Ma *et al.*, 2004a; Ayturk *et al.*, 2006). For the deposition on a porous surface, Ag metal tends to deposit on easily accessible surface sites, thus resulting in the formation of clusters that grow in the direction normal to the surface and leads to a poor penetration at the pore mouths and valleys on the porous surface as schematically illustrated in Figure 7-1.

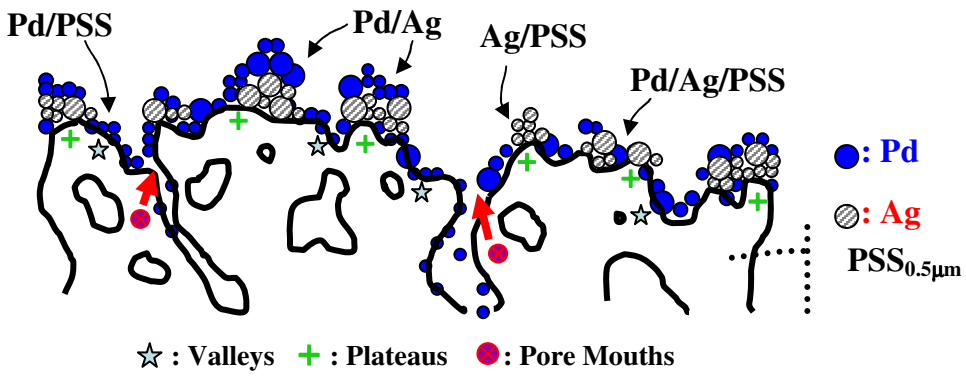

Figure 7-1: Deposition morphology of Pd and Ag deposits on PSS surface

On the other hand, electroless Pd plating covers the entire support surface with a uniform layer of tightly knitted clusters. The Pd deposition not only occurs on the Ag deposited sites but also penetrates into every pore wall and valley on the PSS surface (Ma *et al.*, 2004a). These topological features of the electroless plating of Pd and Ag on PSS, therefore, result in the formation of various interfaces that can be considered as binary (Pd/Ag, Pd/PSS and Ag/PSS) and ternary (Pd/Ag/PSS) metal systems at the contact surfaces corresponding to the pore mouths, valleys and plateaus of the PSS supports as shown in Figure 7-1.

It should also be noted that, insufficient temperature or time for the diffusion treatment (annealing) of Pd and Ag deposits formed by the electroless plating, can result in incomplete alloy formation. On the other hand, annealing temperatures which are too high can result in the intrusion of the support metals (Fe, Cr and Ni) into the membrane layer and the formation of undesirable alloy phases (i.e., Pd/Fe, Pd/Ni, Pd/Ag/Fe and etc.). Indeed, the compositional distribution of Pd and Ag metals at these co-existing metal-metal interfaces might exhibit significant variance depending on the annealing conditions to form the alloy. Therefore, a better understanding of the surface interactions and phase changes at the support interface is essential to obtain uniform Pd/Ag alloys. For this purpose, the formation of both the fcc Pd/Ag alloy phase and other undesirable phases containing Pd, Ag and support metals and the associated changes in the surface morphology was studied at a temperature range of 500°C-800°C and will be discussed in greater detail.

7.2.2. Characterization of Intermetallic Alloy Phases

A typical X-ray diffraction pattern for the as-synthesized Pd and Ag deposit is given in Figure 7-2[a]. For the sample shown in Figure 7-2[a], a total of 90 min. Pd and 180 min. Ag deposition was carried out by the sequential electroless plating on a 0.5 μm media grade PSS plate. Both Pd and Ag had the face centered cubic (fcc) crystal structure as shown in Figure 7-2[a] by the characteristic peak locations at the high intensity planes (111), (200) and (220).

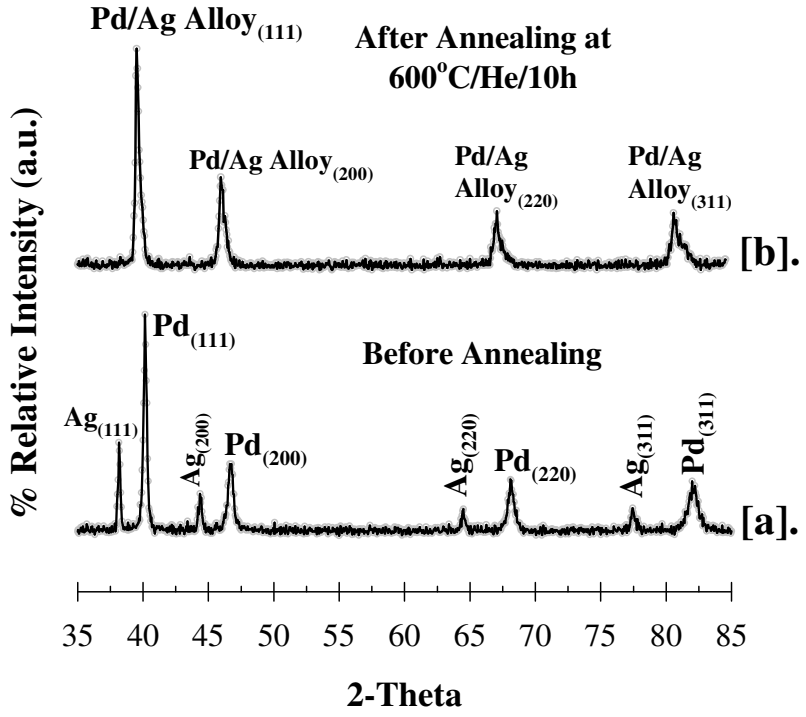

Figure 7-2: X-ray diffraction patterns for Pd and Ag deposited PSS support [a] before and [b] after the annealing treatment @ 600°C/He/10h

The diffusion treatment (annealing) for the as-synthesized Pd and Ag layer was conducted at 600°C for 10 hours in helium atmosphere (designated as 600°C/He/10h). As shown in Figure 7-2[b], pure Pd and Ag phases disappeared to form a single fcc Pd/Ag alloy phase upon annealing at 600°C/He/10h. Similar XRD patterns on the alloying of electrolessly deposited Pd/Ag layers were also reported by various researchers (Uemiya

et al., 1991b; Shu *et al.*, 1993). The key to the interpretation of the diffraction patterns of alloys is the fact that each phase produces its own pattern independent of the presence or absence of any other phases (Cullity and Stock, 2001). Thus, a single-phase alloy produces a single pattern. Palladium and silver metals are completely soluble in the solid state as illustrated by the phase diagram given in Figure 7-3[a] (Karakaya and Thompson, 1988). The solid phase α forms a continuous solid solution, which is of the substitutional type. Substitutional alloys of Pd and Ag, which have the face-centered cubic (fcc) phase, vary only in composition but not in crystal structure. Since all Pd/Ag alloys in a system of this kind consist of the same single phase, their diffraction patterns appear quite similar, as shown in Figure 7-2[a] and [b]. The only effect of a change in the composition was the shift in the diffraction line positions in accordance with the change in the lattice parameter of the α-phase (Figure 7-3[b]), which varied continuously from that of pure Ag to that of pure Pd (Cullity and Stock, 2001). Figure 7-3[b] also shows that the Pd and Ag solid solutions followed the Vegard's Law, which states that the lattice parameter of the solution is directly proportional to the weight percent of the solute (Pd).

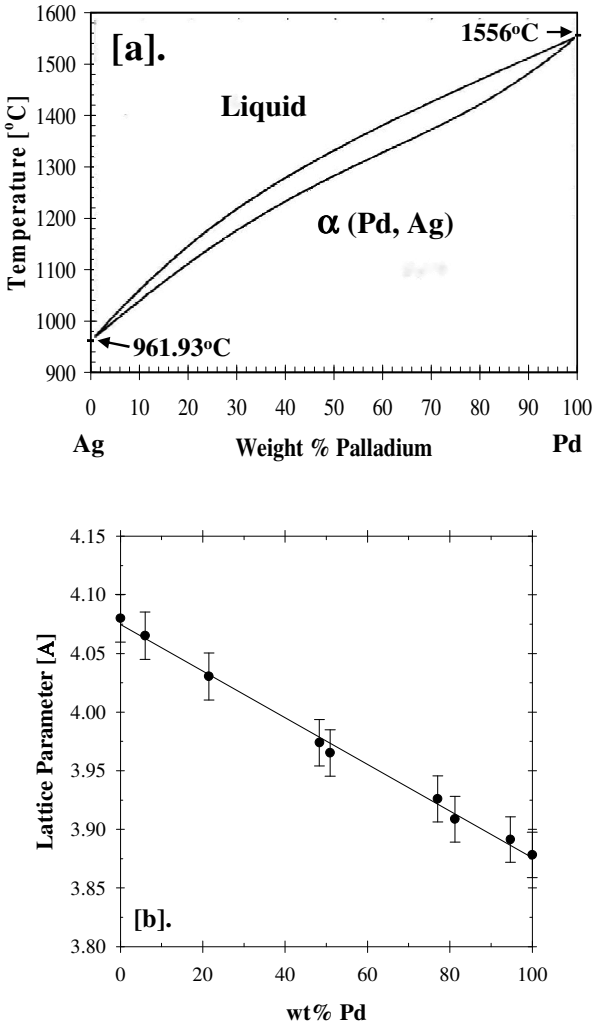

Figure 7-3: [a] Pd/Ag binary phase diagram (Karakaya and Thompson, 1988) and [b] Lattice parameter for the Pd/Ag solid solutions (Cullity and Stock, 2001)

It should be noted that a diffraction pattern of a given phase is characterized not only by the line positions but also by the line intensities. It can be seen in Figure 7-2[a] that the X-ray diffraction pattern taken before the annealing treatment did not provide any information of the PSS support which lay beneath the Pd/Ag layer. Even though the X-ray pattern given in Figure 7-2[b] indicated the formation of a new Pd/Ag alloy phase, it was very difficult to conclude if there were any intrusion from support metals (Fe, Cr and Ni) into the Pd/Ag alloy phase. This might be in fact associated with the thickness of the Pd/Ag deposition layer, which was gravimetrically estimated as ~11 μm after a total of 90 minutes of the Pd and 180 minutes of the Ag deposition. However, the thickness estimated from the cross-section SEI micrographs was in the range of 4-20 μm. The

mismatch between the gravimetric and the SEM-measured thickness for the electrolessly plated Ag films was due to the preferential deposition and the vertical growth tendency of the Ag clusters. Based on the discussion of Figure 7-1 on the characteristic surface topologies of the Pd and Ag deposits on the PSS supports, it appears that, there was a strong possibility for the deposited metals (especially Ag) to form islands on the surface of the substrate, as well as non-uniform deposition at the first or deeper layers. Therefore, the uniformity of the Pd/Ag alloy layer at the bulk might substantially differ from the phases formed at the regions closer to the PSS substrate (Cristensen et al., 1997). Indeed, the EDX line scans for the same specimen indicated that the diffusion of PSS elements into the Pd/Ag alloy phase was in the order of 1.5-2.0 μm. Since the gravimetrically calculated thickness in the case of the Ag deposited porous metal surfaces differed significantly from the thickness observed from cross-section SEI micrographs, it was also important to consider the effects of the X-ray penetration on the diffracted intensity when characterizing intermetallic alloy phases. Most metallurgical specimens strongly absorb X-rays, and the intensity of the incident beam is reduced almost to zero in a very short distance below the surface as discussed in greater detail by Cullity and Stock (2001). The diffraction beams therefore originate chiefly from a thin surface layer whenever the reflection technique is used. The intensity diffracted by the layer at depth x as a fraction of the total integrated intensity diffracted by a specimen of infinite thickness can be calculated by using Equation (7-1) (Cullity and Stock, 2001).

$$G_x = \frac{\int_{x=0}^{x=x} dI_D}{\int_{x=0}^{x=\infty} dI_D} = \left[1 - e^{-\frac{2\mu x}{\sin\theta}}\right] \qquad (7\text{-}1)$$

where, G_x is the fraction of the total diffracted intensity contributed by a surface layer of depth x. The depth of penetration, given by Equation (7-1), can sometimes be surprisingly small. The fractions of the total diffracted intensity in a diffractometer with CuKα radiation for the (111) planes of Pd, Ag and PSS (i.e., $Cr_{0.19}Fe_{0.70}Ni_{0.11}$) metals calculated from Equation (7-1) are given in Figure 7-4.

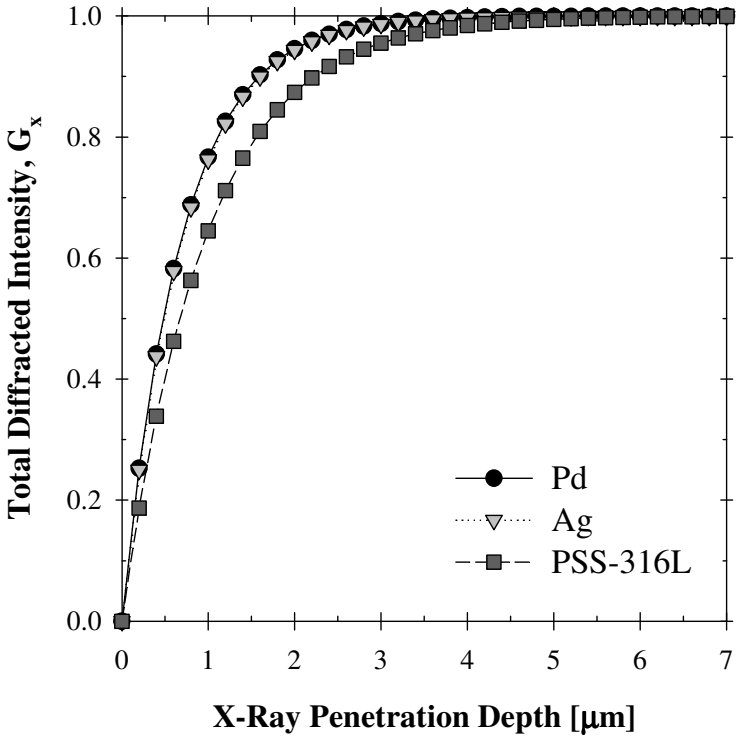

Figure 7-4. Total diffracted intensity vs. X-ray penetration depth for Pd, Ag and PSS (e.g., $Cr_{0.19}Fe_{0.70}Ni_{0.11}$) at the (111)-plane

As can be depicted from Figure 7-4, 95% of the information recorded on the diffraction pattern came from the X-rays penetrated to 2.0-2.2 μm depth for Pd and Ag and 2.8-3.0 μm for PSS. The intensity of the incident beam decreased exponentially with distance below the surface. Figure 7-4 also shows that close to 100% of the X-rays had already been absorbed at a thickness range of 4.0-5.0 μm. Therefore, it is essential to consider the sample layer thickness, which needed to be less than 4.0-5.0 μm, before proceeding further with the XRD phase analysis of the annealed specimens.

For this purpose, three sample sets were prepared by the electroless deposition of Pd and Ag on the as-received 0.5 μm media grade PSS coupons as representative batches of Pd/PSS, Ag/PSS binary and Pd/Ag/PSS ternary systems. The PSS coupons were prepared by cutting a 1 dm^2 316L 0.5 μm media grade PSS sheet of 0.1 cm thick, 1.5 cm by 1.0 cm pieces. The surfaces of the PSS coupons were activated by the regular $SnCl_2$-$PdCl_2$ cycle as discussed in Section 3.1. Following the activation, two sample sets, consisting of three

pieces each, were prepared by conducting 25 minutes of Pd-only and 25 minutes of Ag-only electroless deposition on PSS. The resulting thicknesses from 25 minutes of electroless plating of Pd and Ag were in the order of 0.5 μm and 0.25 μm, respectively. Similarly for the ternary analysis, a third sample set was prepared by first conducting 90 minutes of Ag and then 90 minutes of Pd deposition. The thicknesses in the cases of 90 minutes of Ag and Pd deposition were in the order of 0.75 μm and 1.5 μm, respectively. For the ternary analysis, longer plating times were selected in order to increase the plating surface coverage, insuring the existence of the metal-metal interfaces between the support metals (Fe, Cr and Ni) and the electroless plated Pd and Ag metals as illustrated in Figure 7-1. The annealing treatments for the Pd/PSS, Ag/PSS and Pd/Ag/PSS specimens were carried out at 500°C, 600°C and 800°C with a heating/cooling rate of 5°C/min for about 20 hours and in H_2 atmosphere (T[°C]/H_2/20h). It should be noted that Fe was the major component in 316L porous stainless steel supports with a compositional range of 68 to 70 wt%. Therefore, the discussion regarding the annealed Pd and Ag deposited PSS is directed to the interactions of Pd/Fe, Ag/Fe binary and Pd/Ag/Fe ternary systems.

7.2.2.1. The Pd/PSS Binary System

The X-ray diffraction patterns for the Pd/PSS binary samples annealed at 500°C, 600°C and 800°C are shown in Figure 7-5.

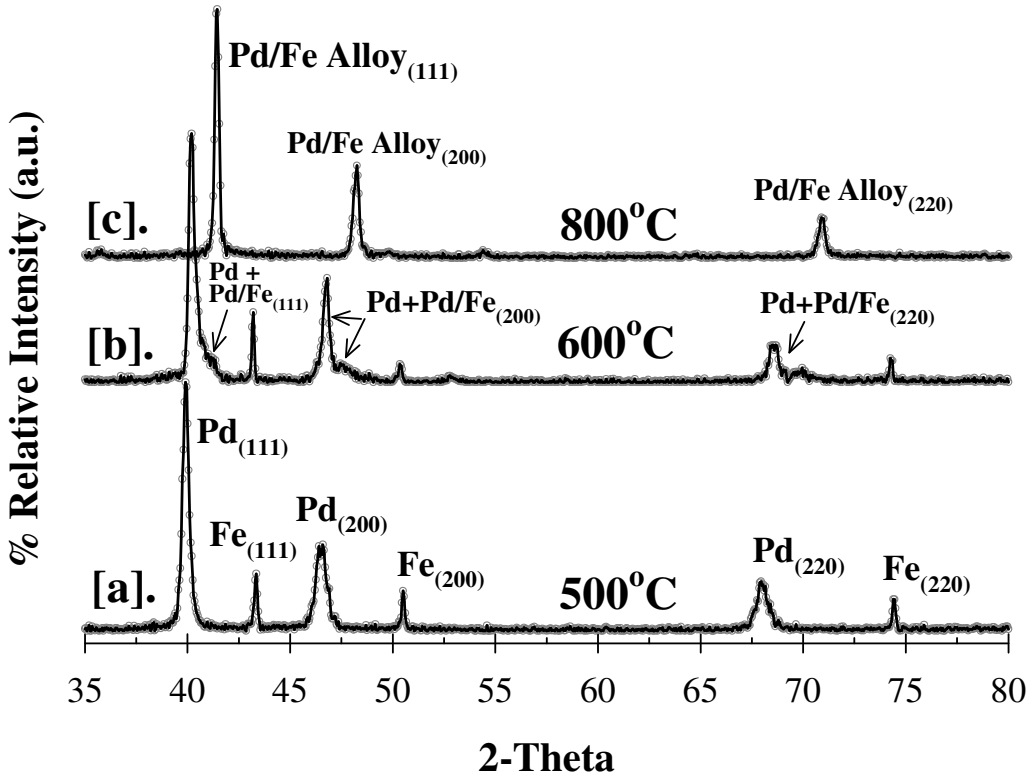

Figure 7-5: XRD patterns for the samples annealed at 500℃, 600℃ and 800℃ in H_2 for 20 hours

For the sample annealed at 500°C/H_2/20h, Figure 7-5[a] shows the characteristic peaks of both the Pd deposit and the PSS support located at the (111), (200) and (220) planes. Since the annealing temperature of 500°C was well below the Tamman temperatures of both Pd (T_{Tamman}: 640°C) and 316L PSS (T_{Tamman}: 550-560°C), the Fe segregation into the Pd matrix was too small to be detected by the resulting XRD pattern as a separate alloy peak. However, peak broadening observed at the characteristic fcc planes for Pd in Figure 7-5[a], might indicate the presence of small intrusion from the support metals into the Pd layer. At an annealing temperature of 600°C, the formation of a new Pd-rich Pd/Fe alloy phase was detected as shoulders appeared at the characteristic fcc planes (111), (200) and (220). The XRD pattern taken after the annealing of the Pd/PSS specimen at 600°C/H_2/20h also indicated that the Pd-rich Pd/Fe alloy phase co-existed with the pure Pd and Fe phases as shown in Figure 7-5[b]. A further increase in

the annealing temperature to 800°C resulted in the disappearance of the pure Pd and Fe peaks and the formation of a pure Pd/Fe alloy phase with an fcc crystal structure (Figure 7-5[c]). Since the 800°C annealing temperature was well above the Tamman temperatures of both metals, it provided sufficient energy for the binary solid solution to re-distribute within the layers and to form a uniform Pd/Fe alloy phase. The SEI micrographs given in Figure 7-6 show the changes in the surface topology of the Pd/PSS binary system after annealing.

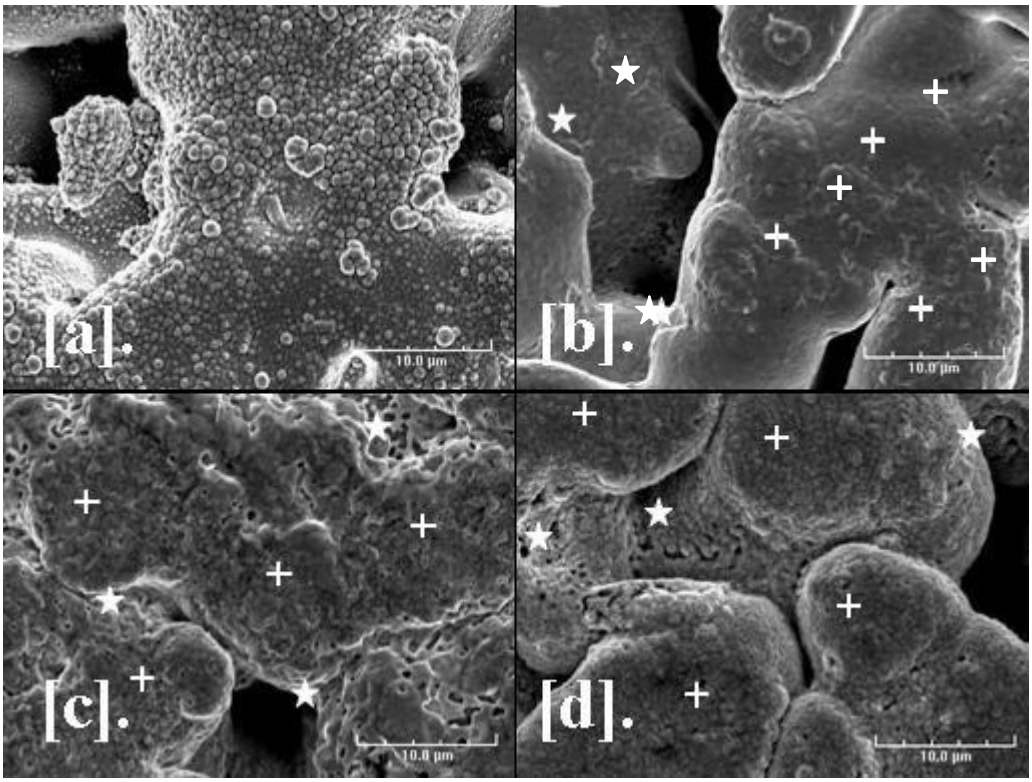

Figure 7-6: SEI micrographs on the surface topology of annealed Pd/PSS binary system (@ 3kX) [a] Un-annealed, [b] Annealed @ 500°C/H_2/20h, [c] Annealed @ 600°C/H_2/20h and [d] Annealed @ 800°C/H_2/20h (+: Plateaus, ★: Valleys)

The Pd deposits in Figure 7-6[b] after annealing at 500°C/H_2/20h appeared to be in the form of larger clusters, which had a relatively smooth surface texture in comparison to the as-synthesized Pd clusters shown in Figure 7-6[a]. On the other hand, a noticeable change in the surface morphology was observed for the sample annealed at 600°C/H_2/20h (Figure 7-6[c]) with respect to Figure 7-6[a] and Figure 7-6[b]. The XRD patterns in Figure 7-5[b] indicated that the pure Pd, Fe and Pd-rich Pd/Fe alloy phase coexisted upon

annealing at 600°C/H_2/20h due to the incomplete intermetallic diffusion between the PSS support elements and the Pd layer. Therefore, the simultaneous nucleation, growth and thus, the thickening of the Pd/Fe alloy phase at 600°C might have caused the surface topology in Figure 7-6[c] to look relatively crumbly and non-uniform. For the specimen annealed at 800°C/H_2/20h (Figure 7-6[d]) a uniform surface morphology which appeared to look like a thick oxide-scale was observed over the entire support surface even extending to regions covering the pore walls, pore mouths and valleys. This was also in agreement with the formation of a pure fcc Pd/Fe alloy phase as shown in Figure 7-5[c].

The binary phase diagram of Pd/Fe system, which was reported by Okamoto and Masalski (1990) is given in Figure 7-7. According to Chen *et al.* (2002), the main features of the phase diagram of the Pd/Fe system were characterized by the phase separation in the Fe-rich region (> 90 wt% Fe) due to the size mismatch among αFe, δFe and γFe phases and the appearance of two ordered phases, namely FePd and $FePd_3$, in the Pd-rich region (> 62 wt% Pd). The Pd/Fe binary phase diagram shows a continuous region of solid solution with fcc structure existed over the entire composition range at high temperatures (> 700°C). However, at lower temperatures the fcc phase was still stable above 90 wt% of Pd.

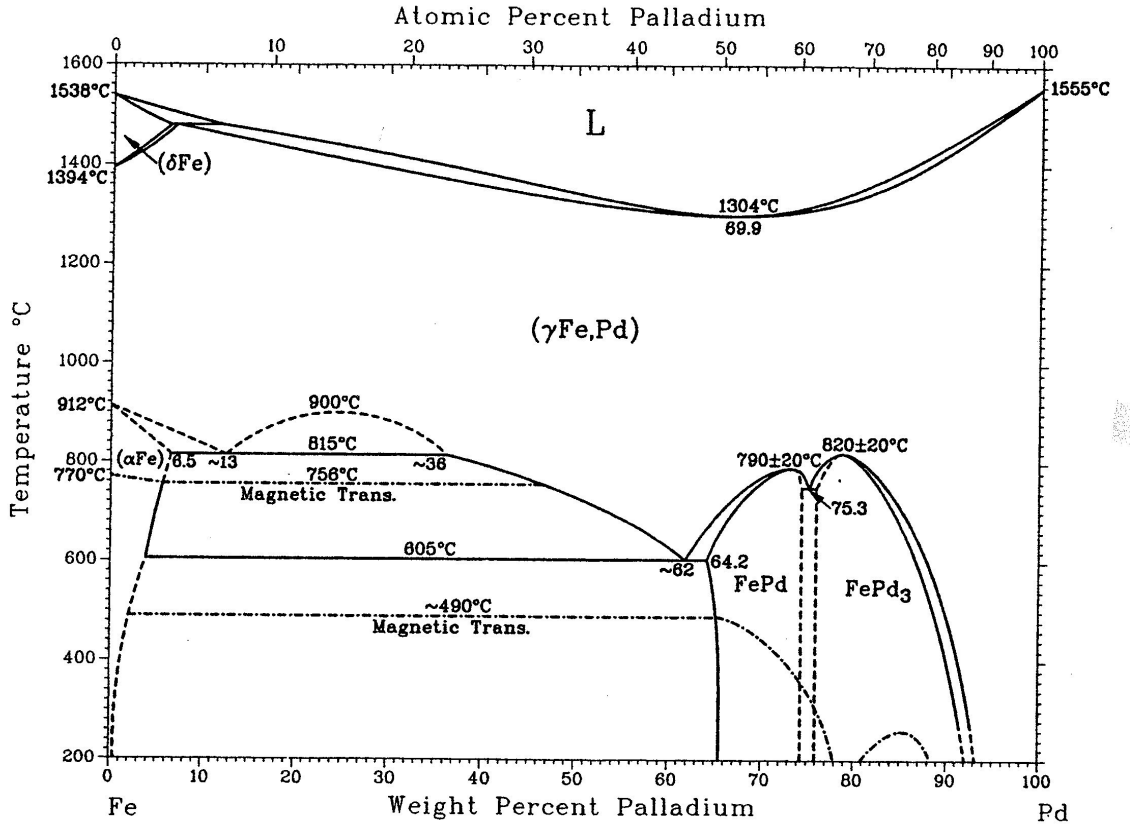

Figure 7-7: Pd/Fe binary phase diagram (Okamoto and Masalski, 1990)

The average surface compositions of the specimens annealed at 500°C, 600°C and 800°C were determined via the EDX area scan analyses and given in Figure 7-8. The spatial resolution for the EDX analysis of Pd, Ag, Fe, Cr and Ni metals lay between 0.5 to 0.7 µm at an accelerating voltage of 15 keV and between 0.8 to 1.2 µm at an accelerating voltage of 20 keV (Friel, 1998).

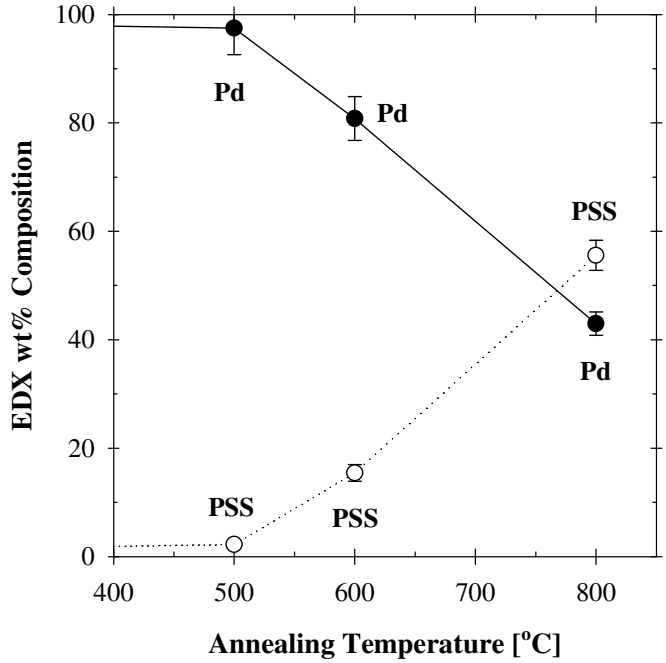

Figure 7-8: EDX area scans for the Pd/PSS binary solid solutions after annealing (The PSS label refers to the total wt% composition of Fe, Cr and Ni on the surface)

Figure 7-8 shows that the average surface composition of the sample annealed at 500°C was ~97.6 wt% Pd, ~2.2 wt% PSS with trace amounts of surface impurities. According to the Pd/Fe binary phase diagram given in Figure 7-7, 97.6 wt% of Pd corresponds to the Pd/γFe solid solution. Similarly, for the sample annealed at 600°C the average surface composition was estimated as 80.8 wt% Pd and 15.4 wt% PSS. According to the Pd/Fe binary phase diagram, the lever-rule estimate of 80 wt% Pd at 600°C corresponded to a Pd/Fe solid solution, which was composed of ~67% PdFe and ~33% $FePd_3$ phases. The average surface composition for the 800°C annealed sample was estimated as 49.3 wt% of Pd and 58.9 wt% PSS, which indicated a significant Fe diffusion into the Pd layer. According to the Pd/Fe binary phase diagram the solid solution with a Pd content of ~49 wt% corresponded to the completely miscible Pd/γFe alloy phase which was in agreement with the alloy phase formation as shown in Figure 7-5[c]. Further evidence on the alloying of Pd and Fe metals can also be obtained from the changes in the lattice parameter. The lattice parameters for the pure Pd, PSS ($Cr_{0.19}Fe_{0.70}Ni_{0.11}$) and Fe are 3.89Å, 3.59Å and 2.87Å, as reported in (JADE4.0,) powder

diffraction database files #46-1043, #33-0397 and #06-0696, respectively. By using the XRD patterns given in Figure 7-5, the Pd lattice parameters upon annealing at 500°C, 600°C and 800°C were estimated as 3.89Å, 3.87Å and 3.76Å, respectively. Since the intermetallic diffusion is a temperature activated process, the further Fe diffusion into the Pd layer with increasing annealing temperature (i.e., 59 wt% Fe diffusion for the sample annealed at 800°C), apparently reduced the Pd lattice as shown by the above lattice parameter calculations. The changes in the lattice parameter due to the Fe diffusion was in good agreement with the data reported by Bryden and Ying (2002). Since increasing the Fe content would shrink the metal lattice and reduce the H_2 solubility and diffusivity (Flanagan *et al.*, 1977; Bryden and Ying, 2002), the intermetallic diffusion of the PSS components into the Pd matrix and the formation of undesirable alloy phases during the high temperature diffusion treatment, might significantly alter the hydrogen permeance for Pd/Ag/PSS composite membranes as previously illustrated with the permeance data of membrane 001 in Figure 5-2.

7.2.2.2. The Ag/PSS Binary System

Besides the Pd/PSS binary system, it is of equal importance to understand the interactions of Ag metal with the support metal. For this purpose, a similar experimental procedure as in the Pd/PSS case was followed for the Ag/PSS samples, as discussed in Section 7.2.2.1. The X-ray diffraction patterns for the Ag/PSS binary system annealed at 500°C, 600°C and 800°C are shown in Figure 7-9.

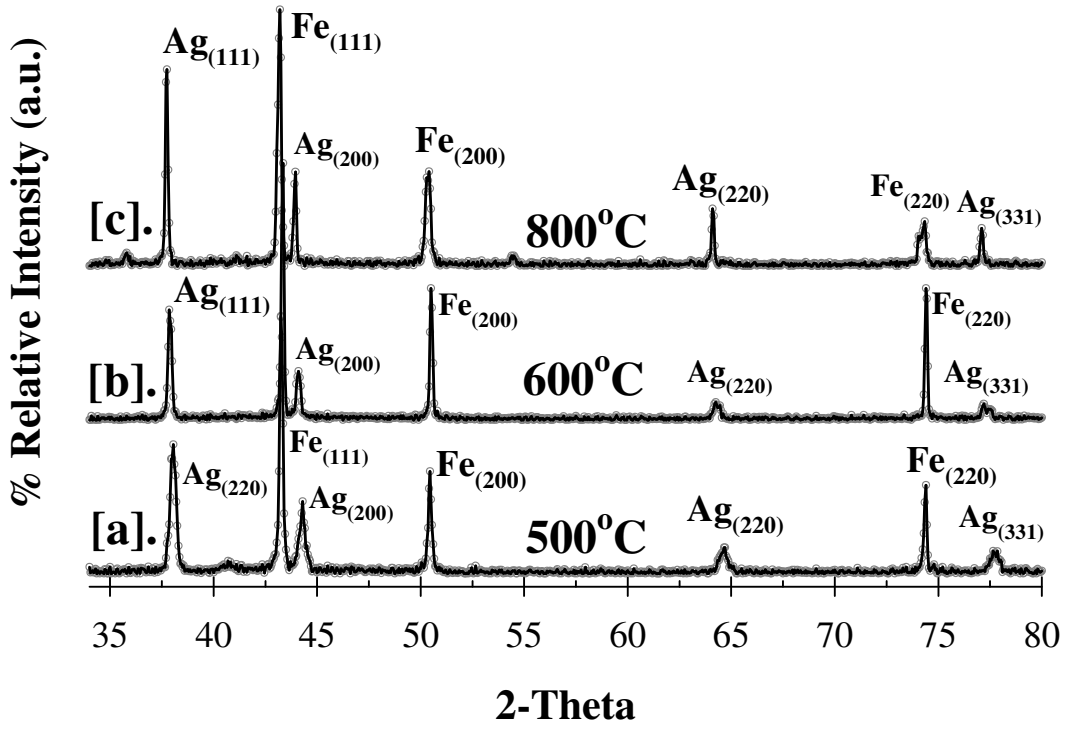

Figure 7-9: X-ray diffraction patterns for the Ag/PSS samples annealed at 500℃, 600℃ and 800℃ in H_2 for 20 hours

It was interesting to note that the characteristic peak positions located at the (111), (200) and (220) planes both for Ag and PSS did not exert any change upon annealing at 500°C, 600°C and 800°C. This indicated a likelihood of immiscibility of these two metals. According to the Ag/Fe phase diagram given in Figure 7-10, Ag/Fe system consists of an immiscible αFe-Ag solid solution below 911.5°C (Swartzendruber, 1984). The immiscibility of Ag and Fe metals also extends into the liquid phase above 1500°C (designated as L_1 and L_2 phases in Figure 7-10).

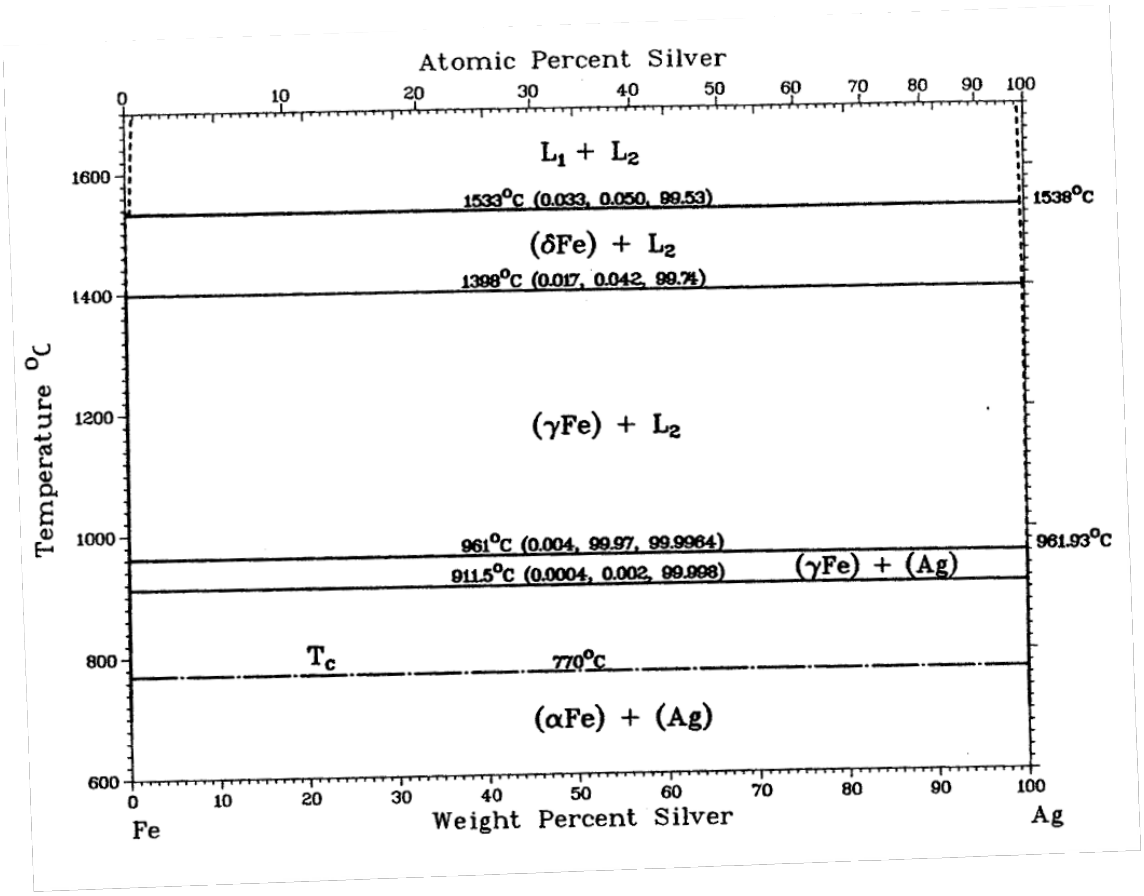

Figure 7-10: Ag/Fe binary phase diagram (Swartzendruber, 1984)

Adda and Philibert (1966) have reported that the maximum solubility of Ag in αFe is 0.0002 at% and the solubility of αFe in Ag is 0.0065 at%(below 911.5°C). Since the mutual solubility for the Ag/Fe system both in the liquid and solid states is extremely low, no stable alloys of appreciable compositions exist under the equilibrium conditions (Bonyuet et al., 2004). Figure 7-11 shows the changes in the surface morphology of the Ag/PSS binary system after annealing at 500°C, 600°C and 800°C for 20 hours in H_2. As can be seen from the SEI micrographs shown in Figure 7-11, the distribution of the Ag deposits on the PSS surface both before and after the annealing treatments was quite random and non-uniform. The net effect of the high temperature annealing for the Ag/PSS binary system appeared to be the observed increase in Ag cluster size with increasing temperature. Upon annealing at 500°C, 600°C and 800°C , the lattice parameters of the fcc Ag phase (a_{Ag}: 4.08Å, PDF#04-0783, JADE4.0, database) were estimated using the XRD patterns shown in Figure 7-9 as 4.08Å, 4.10Å and 4.12Å,

respectively. This is an indication that the observed increase in the Ag cluster size was associated with the lattice expansion of the Ag metal. Similar observations were reported by Fahler *et al.* (1998).

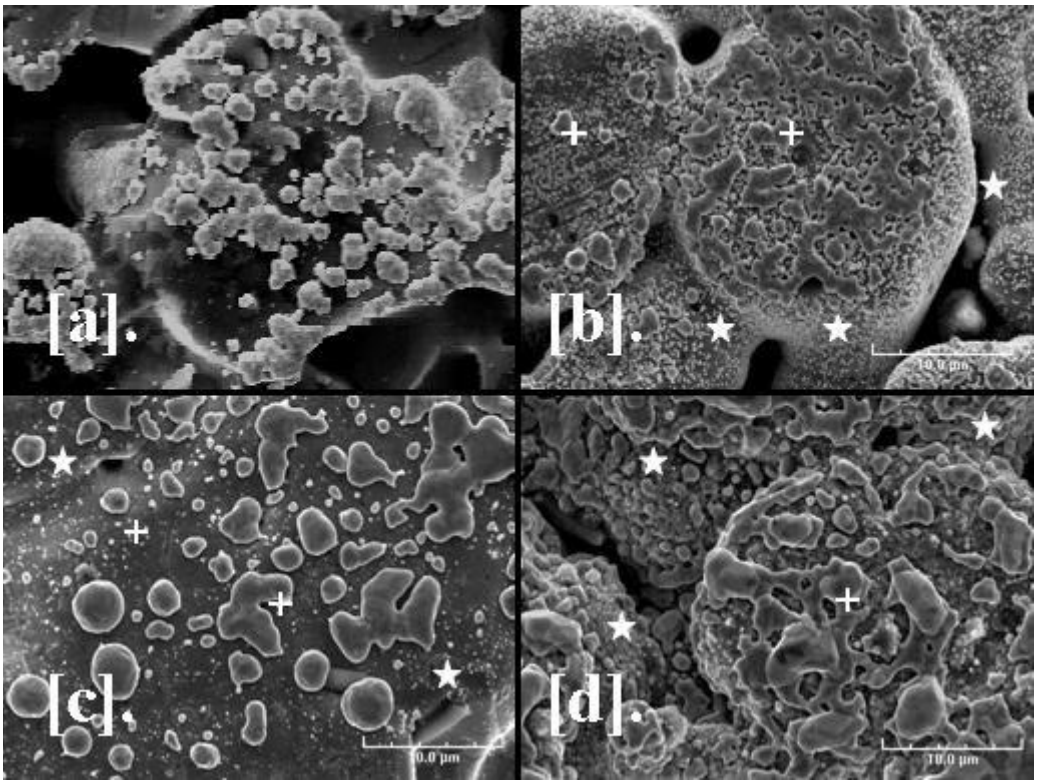

Figure 7-11: SEI micrographs on the surface topology of the annealed Ag/PSS binary system (@ 3kX) [a]. Un-annealed, [b]. Annealed @ 500°C/H_2/20h, [c]. Annealed @ 600°C/H_2/20h and [d]. Annealed @ 800°C/H_2/20h (+: Plateaus, ★: Valleys)

Figure 7-12 summarizes the EDX area scan analyses for the annealed Ag/PSS samples. In contrary to the EDX data shown in Figure 7-8 for the Pd/PSS system, the EDX area scans in Figure 7-12, taken on the Ag clusters that were located at the plateaus of the PSS support, showed a constant composition at each annealing temperature indicating that Fe diffusion into the Ag layer was not significant. This was also in good agreement with the immiscibility of the αFe and Ag solid phases as shown by the XRD patterns and the Ag/Fe phase diagram in Figure 7-9 and Figure 7-10, respectively.

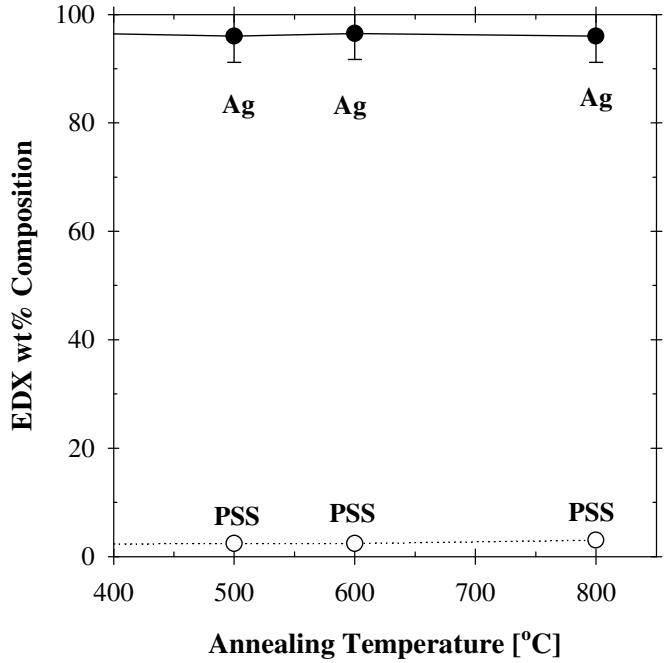

Figure 7-12: EDX area scans for the Ag/PSS binary system after annealing (The PSS label refers to the total wt% composition of Fe, Cr and Ni on the surface)

7.2.2.3. The Pd/Ag/PSS Ternary System

Following the results on Pd/PSS and Ag/PSS binary systems, the morphology and the associated phase changes upon annealing were investigated for the Pd/Ag/PSS ternary system. For the Pd/Ag/PSS ternary system, specimens for the annealing experiments were prepared by carrying out first 90 minutes of Ag plating and then 90 minutes of Pd plating on PSS supports as described in section 3.2. Figure 7-13 shows the XRD patterns of the Pd/Ag/PSS ternary system after the annealing treatments conducted at 500°C, 600°C and 800°C in hydrogen for 20 hours each.

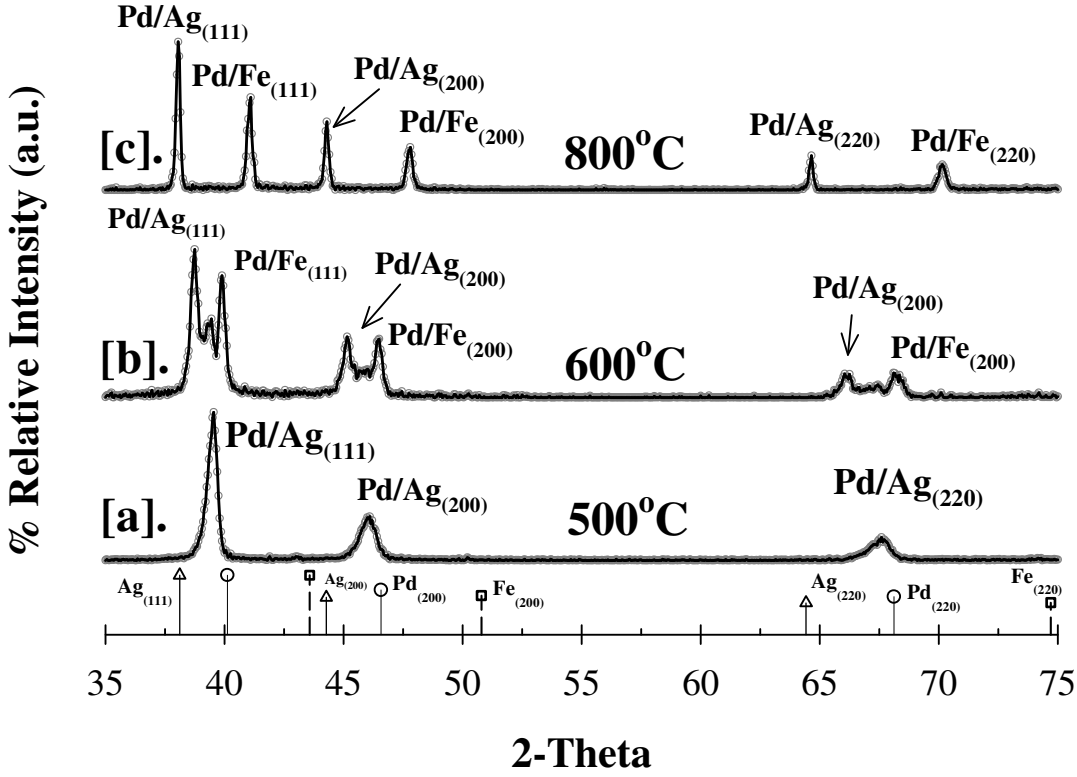

Figure 7-13: XRD patterns for the Pd/Ag/PSS ternary system both before and after the annealing @ [a] 500°C/H_2/20h, [b] 600°C/H_2/20h and [c] 800°C/H_2/20h (Ag: PDF#04-0783, Pd: PDF#46-1043 and $Cr_{0.19}Fe_{0.70}Ni_{0.11}$: PDF#33-0397, JADE4.0, database)

Upon annealing at 500°C, the Fe diffusion was less pronounced and the XRD pattern given in Figure 7-13[a] indicated that the resulting phase was a Pd-rich Pd/Ag alloy phase. It should be noted that the Fe concentration for the Pd/PSS binary system at 500°C was only ~2.2 wt% as shown by the EDX data provided in Figure 7-7, yet, high enough to alter hydrogen permeance (Bryden and Ying, 2002). The XRD pattern for the sample annealed at 600°C (Figure 7-13[b]), indicated that the Fe diffusion into the Pd matrix was higher than the sample annealed at 500°C. However, annealing at 600°C resulted in the simultaneous formation of both the Pd-rich Pd/Fe and the Pd-rich Pd/Ag phases. As can be depicted from the significant shift in the characteristic peak locations of the Pd/Ag alloy phase at (111), (200) and (220) planes in Figure 7-13[b], the Pd content of the Pd/Ag alloy phase decreased with respect to the sample annealed at 500°C.

These observations were in good qualitative agreement with the discussion in Section 5.3.1 regarding the stability of membrane 011 at 600°C (Figure 5-2). XRD pattern shown in Figure 7-13[b] supported the fact that the formation of a Pd-rich Pd/Fe alloy phase between the support metal and the Pd/Ag barrier layer interface was not harmful to the permeability of the hydrogen selective top Pd layer. Although a noticeable intermetallic diffusion might have taken place at 600°C, the unique deposition morphology of the porous Pd/Ag barrier layer provided enough resistance, giving stable hydrogen permeances at such high temperatures as shown in Figure 5-2 and Figure 5-4.

Furthermore, the XRD pattern for the sample annealed at 800°C indicated the formation of an Ag-rich Pd/Ag alloy phase and a Fe-rich Pd/Fe alloy phase as can be seen from the characteristic fcc planes in Figure 7-13[c]. The formation of the Pd/Fe alloy phase at 800°C was in good agreement with the XRD patterns and the SEI micrographs given in Figure 7-5[c] and Figure 7-6[d] for the Pd/PSS binary system. On the other hand, since Ag and Fe were immiscible both in solid and liquid phases, the interdiffusion between Pd and Ag metals led to the formation of an Ag-rich Pd/Ag alloy phase. The SEI micrographs for the annealed Pd/Ag/PSS ternary samples are shown in Figure 7-14.

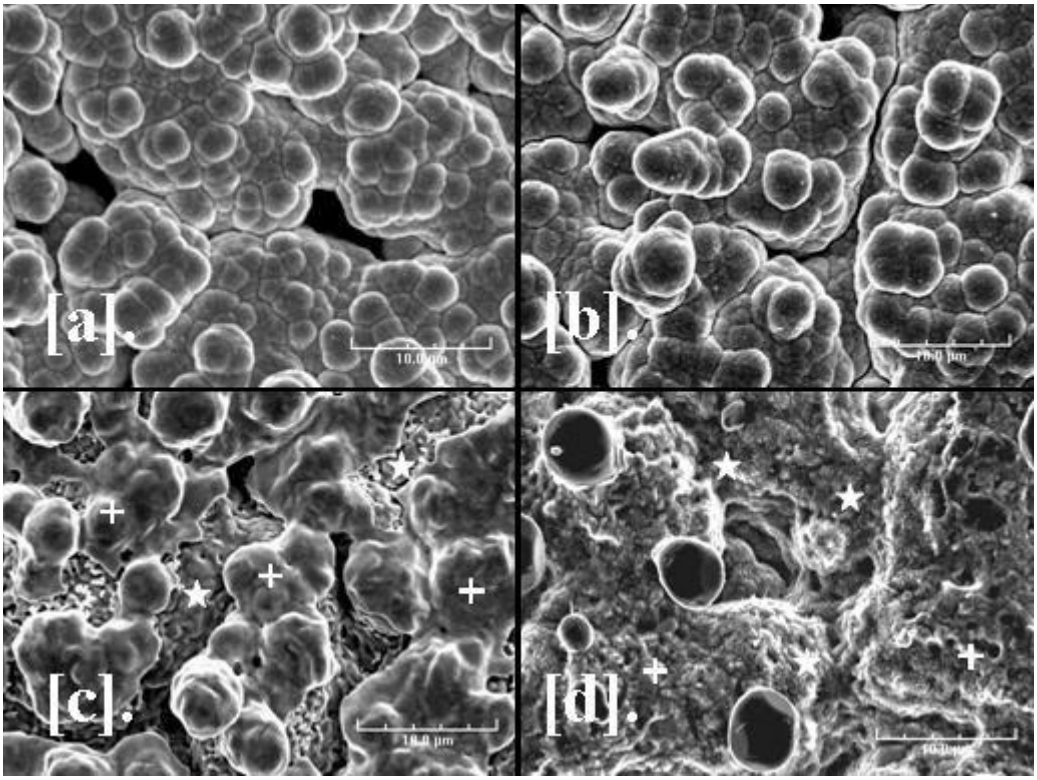

Figure 7-14: SEI Micrographs for the Pd/Ag/PSS ternary system (@ 3kX) [a]. Un-Annealed, [b]. 500℃/H_2/20h, [c]. 600℃/H_2/20h and [d]. 800℃/H_2/20h (+: Plateaus and ★: Valleys)

The SEI micrograph for the Pd/Ag/PSS ternary system before annealing is given in Figure 7-14[a]. The sample annealed at 500°C showed a similar morphology as the un-annealed sample except the fact that the size of the Pd and Ag clusters after annealing at 500°C was slightly larger. The EDX surface analysis for this sample also indicated that the Pd, Ag and PSS average surface compositions were 96.9 wt%, 2.0 wt% and 0.8 wt%, respectively with trace amount of impurities. The average surface compositions estimated by the EDX were in good agreement with the formation of the Pd-rich Pd/Ag alloy phase shown by the XRD pattern in Figure 7-13[a]. The SEI micrograph of the sample annealed at 600°C in Figure 7-14[c] indicated that the annealing morphology at the pore wall and valleys were different from the morphology of the Pd and Ag deposits which were located on the surface plateaus. For the cauliflower like deposits that were located at the plateaus of the surface, the compositional distributions estimated by the EDX analysis were in the range of 62-70 wt% for Pd, 36-25 wt% for Ag and 0-0.5 wt% for PSS with trace amount of impurities. Similarly, the XRD data given in Figure 7-13[b] and the EDX

surface analysis were in good agreement with the formation of Pd-rich Pd/Ag alloy phase. The EDX area scans corresponding to the regions between the cauliflower-like deposits and regions that covered the pore wall and valley areas, resulted in 90.7 wt% Pd, 4.5 wt% Ag and 4.6 wt% PSS with trace amount of impurities. This was also a further evidence for the formation of a Pd-rich Pd/Fe alloy at 600°C as shown previously in Figure 7-13[b]. The resulting surface morphology for the sample annealed at 800°C had two distinct features similar to the sample annealed at 600°C. As can be depicted from Figure 7-14[d], the Ag-rich deposits were located on top of the plateaus of the surface, which were round in shape and even faceted at the corners. However, the rest of the surface morphology mainly located at the pore wall and valley regions appeared to look quite uniform. The EDX analysis on the faceted Ag-like deposits resulted in an average surface composition of 12 wt% Pd, 86.6 wt% Ag and 0.4 wt% PSS with trace amount of impurities, which were in good agreement with the formation of a Ag-rich Pd/Ag alloy phase shown in Figure 7-13[c]. The EDX area scans conducted for the rest of the surface of the sample annealed at 800°C resulted in an average compositional range of 18-20 wt% for PSS and at varying compositions between 35-45 wt% and 26-37 wt% for Pd and Ag, respectively.

7.2.3. Synthesis and Characterization of a Pd/Ag//PSS Membrane with a pure-Ag Layer as an Intermetallic Diffusion Barrier

Based on the results of the Ag/PSS binary system discussed in Section 7.2.2.2, it appears that a pure-Ag layer, if deposited uniformly on the PSS surface, might be an excellent intermetallic diffusion barrier due to its both solid and liquid phase immiscibility with Fe.

The effect of the intermetallic diffusion on the hydrogen permeance is expected to be more significant if there are no barrier layers between the support metal and the hydrogen selective dense Pd and/or Pd/Ag layer. In fact, the stability of the porous Pd/Ag barrier against intermetallic diffusion, as shown by the performance of membrane 002 in Figure 5-2 of Section 5.3, might be associated with the low solubility of support metals (Fe, Cr and Ni) in Ag. Recently, Tong *et al.* (2005d) have reported that a 0.3 μm thick electroplated Ag on stainless steel support functioned as a diffusion barrier for hydrogen

permeation test conducted at 500°C for 70 hours. However, the relatively short period of the hydrogen permeation test conducted by Tong *et al.* (2005d) might not be enough evidence to conclude on the long-term thermal stability of the pure-Ag layer as an effective intermetallic diffusion barrier.

To test the effectiveness of the pure-Ag layer as an intermetallic diffusion barrier, a Pd/Ag membrane, designated as 012, was synthesized on a 0.2 μm media grade bare PSS support (1/2" OD and 1" long). Membrane 012 had a 2.9 μm pure-Ag layer formed by the regular electroless deposition between the porous PSS support and the top Pd layer using the Ag bath chemistry given in Table 3-5 of Section 3.1. The hydrogen permeance data at 500°C and 600°C are shown in Figure 7-15.

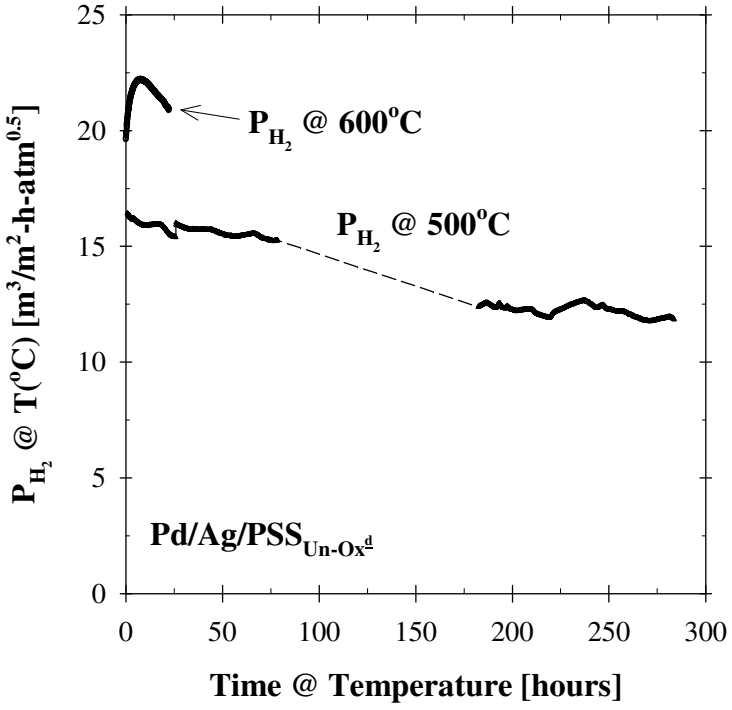

Figure 7-15: Hydrogen permeance plot for the Pd/Ag/PSS membrane 012 at 500°C and 600°C

At 600°C, the hydrogen permeance for membrane 012 showed a slight increase within the first 2 hours of the permeation testing indicating an enhancement due to the formation of a Pd/Ag alloy phase. Since the formation of both the Pd/Ag and Pd/Fe alloy phases took place simultaneously as shown in Figure 7-13[b], the hydrogen permeance of

membrane 012 declined steadily from 22.6 to 21.1 m^3/m^2-h-$atm^{0.5}$ over a period of 14 hours of the permeation testing at 600°C. The deterioration in the hydrogen permeance corresponded to the 6% of the original permeance measured at 600°C. The curvature of the permeance plot at 600°C also indicated that the initial increase in the H_2 permeance due to the formation of a Pd-rich Pd/Ag alloy phase has been overtaken by the formation of a Pd-rich Pd/Fe alloy phase. For the Pd/Ag/Fe ternary system, the SEI micrographs shown previously in Figure 7-14 indicated that the Pd/Ag phase was distributed as isolated clusters, whereas the Pd/Fe phase was more dominant over the entire morphology. These observations coupled with the XRD patterns given in Figure 7-13[b] and the discussion on the topological characteristics of the Pd and Ag deposits (Figure 7-1) were in good agreement with the permeance loss of membrane 012 at 600°C (Figure 7-15) due to the intermetallic diffusion.

The hydrogen permeance of membrane 012 was continuously monitored at 500°C over a period of ~285 hours. As shown in Figure 7-15, the hydrogen permeance at 500°C showed a steady decline from 16.7 to 12.7 m^3/m^2-h-$atm^{0.5}$ indicating further diffusion of the support metals (Fe, Ni and Cr) into the Ag-rich top Pd layer. At 500°C, the total loss in the hydrogen permeance was estimated to be 24%. Even though the Ag/PSS annealing experiments and the data reported in binary phase diagrams indicated solid phase immiscibility between the Ag and the support metals, the permeance data indicated that the 2.9 μm thick pure-Ag layer was not intact enough to provide resistance against the intermetallic diffusion. The non-uniform surface coverage of Ag from the electroless plating baths (Table 3-4) appeared to be the main reason for the poor resistance of the pure-Ag layer as a barrier layer against the intermetallic diffusion.

Coupled with the detailed coupon studies discussed in Sections 7.2.2.1, 7.2.2.2 and 7.2.2.3, the permeance results for membrane 012 shown in Figure 7-15, clearly indicated that the long-term stability of composite Pd and Pd/Alloy membranes required the formation of effective barriers against the intermetallic diffusion.

7.2.4. Conclusions

The intermetallic diffusion of PSS components (Fe, Cr and Ni) resulted in the formation of Pd/Fe alloys at varying proportions at the regions closer to the PSS support. The formation of these surface alloys had a strong effect on the uniformity of the dense and selective Pd/Ag alloy layers. In addition, the formation of a Pd/Fe alloy phase at the support-membrane interface during high temperature diffusion treatments might deteriorate the H_2 permeance for composite Pd and Pd/Alloy membranes, since increasing Fe content shrank the Pd lattice and reduced the H_2 solubility and diffusivity (Flanagan *et al.*, 1977; Bryden and Ying, 2002).

It was verified by the X-Ray phase analysis that Pd and Fe formed completely miscible solid solutions at 500°C (below 5 wt% Fe) and 600°C. At 800°C, pure Pd and Fe peaks disappeared and a pure γFe/Pd alloy formed. SEI micrographs also indicated that the morphology of γFe/Pd alloy phase was uniform throughout the plateaus and the regions covering the pore walls, mouths and the valleys of the PSS support.

The extent of the intermetallic diffusion of the PSS components (Fe, Cr and Ni) into the Pd layer was estimated via the EDX surface scans and found to be in the order of 2 wt%, 15 wt% and 59 wt%, for the Pd/PSS specimens annealed at temperatures 500°C, 600°C and 800°C, respectively.

On the other hand, Ag and Fe metals were found to be immiscible for the temperature range investigated. This was in good agreement with the data reported in Ag/Fe binary phase diagrams. The SEI micrographs indicated that the net effect of high temperature annealing for the Ag/PSS binary system appeared to be the increase in the Ag cluster size with the increasing temperature.

In the case of the ternary phase analysis, it was found that both the Pd/Fe and Pd/Ag alloy formation took place on the support surface simultaneously. Since the Fe segregation was less pronounced at low temperatures, the Pd/Ag and Pd/Fe alloy compositions became richer in Pd with decreasing annealing temperature.

The permeation tests for the composite Pd/PSS and Pd/Ag/PSS showed that the thermal stability of the supports without effective diffusion barriers were severely altered

and the measured hydrogen permeance significantly deteriorated due to the intermetallic diffusion, thus the formation of undesired surface alloys (i.e., Pd/Fe) at the interface between the support metal and the membrane layer. Regardless of its solid phase immiscibility with the support metals, the effectiveness of a pure-Ag layer as an intermetallic diffusion barrier was limited by the non-uniformity of the electroless deposition morphology obtained from regular Ag plating baths.

8. The Effect of Ag on the Synthesis, Long-Term H_2 Characterization and the Thermal Stability of Composite Pd/Ag/PHST and Pd/Ag/Inconel Membranes

8.1. Introduction

Ni-rich PHST and Inconel alloys offer better metallurgical stability, resistance to localized corrosion, and are not sensitized during welding or heating and therefore, well-suited for high temperature membrane reactor applications. Indeed, the coefficients of thermal expansion for the Ni-rich metal supports are a closer match to that of Pd and Ag metals, as shown in Table 2-2.

Unlike PSS supports which were most commonly used as the support materials in the literature for the synthesis of composite Pd and Pd/alloy membranes, Ni-rich porous sintered metal supports have not been widely integrated into membrane reactor applications yet. On the other hand, the synthesis of composite Pd and Pd/Ag membranes throughout this dissertation study has been mainly realized by the use of Ni-rich porous metal supports. Therefore the concepts presented in this Chapter aim at providing a better understanding on the use of Ni-rich porous sintered metal supports for the synthesis of Pd and Pd/Ag membranes. In particular, the main objectives of this study are as follows:

1. To thoroughly understand the deposition morphology, surface interactions and the subsequent phase changes between the Ni-rich porous sintered support metals and the Pd and Ag deposits by investigating the formation of surface alloys upon high temperature annealing treatments.

2. To test the long-term stability of composite Pd/Ag/Inconel membranes formed by the pure-Ag barrier layer deposition and $Al(OH)_3$ surface modification technique.

3. To recapitulate the effectiveness and the stability of the pure-Ag barrier layer formed by the modified electroless Ag plating bath, against intermetallic diffusion.

4. To provide thorough understanding on the oxidation characteristics of the Ni-rich porous supports and the effect of oxide barrier layer formed by the *in-situ* oxidation technique on the long-term stability of composite Pd/Ag/PHST and Pd/Ag/Inconel membranes.

8.2. Electroless Plating Morphology of Pd and Ag Layers on Ni-rich Porous Sintered Metal Supports

Figure 8-1 shows the morphology of the thin Pd-only, Ag-only and Pd/Ag layers on PHST support surface after 30 minutes of electroless deposition. In comparison to the smooth surface appearance of the bare PSS supports shown in Figure 5-5[a], the roughness of the bare PHST support surface, shown in Figure 8-1[a], is due to the different particle size and sintering temperature used to form the substrate. Indeed, EDX spot scan analyses indicated that the rectangular inclusions seen on the surface in Figure 8-1[a] were mainly Mo-rich powder particles.

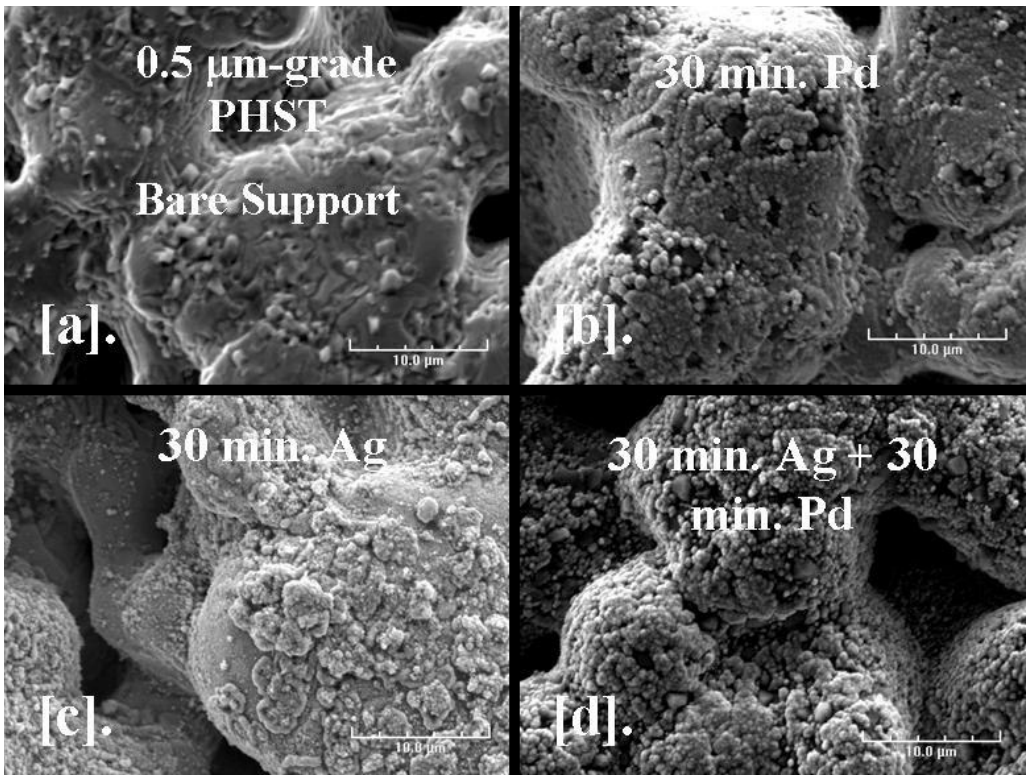

Figure 8-1: SEI micrographs [a] Bare PHST support, [b] 30 min. Pd/ PHST, [c] 30 min. Ag/ PHST and [d] 30 min. Ag + 30 min. Pd on PHST

As shown in Figure 8-1[b], the electroless Pd plating on PHST appeared to be in the form of tightly knitted spherical clusters, which were uniformly distributed and covered the entire support surface. On the other hand, electroless Ag plating on PHST in Figure 8-1[c] resulted in a relatively heterogeneous surface coverage with large Ag clusters that grew either on the neighboring clusters or vertically from the surface. It was also visible in Figure 8-1[c] that the Ag deposition led to a poor penetration at the pore walls and valleys of the PHST support. Finally, Figure 8-1[d] shows the resulting morphology for the electroless plating of Ag and Pd on PHST. SEI micrograph in Figure 8-1[d] indicated that electroless Pd plating not only covered the Ag-plated surface sites, but also penetrated deep into pore walls and valleys of the PHST surface. It was interesting to note that the electroless plating of Pd and Ag both on PHST and PSS supports resulted in almost identical topological features, which were in good agreement with the discussions in Chapters 5 and 7 regarding the microstructure analysis of the Pd and Ag deposits formed by the electroless plating (Ayturk *et al.*, 2006; Ayturk *et al.*, 2007).

8.3. Binary and Ternary Phase Analysis of Pd/PHST, Ag/PHST and Pd/Ag/PHST Systems

To thoroughly understand the electroless plating morphology of Pd and Ag layers on Ni-rich porous sintered metals and the subsequent surface interactions between the Ni-rich PHST substrate, Pd and Ag deposits after high temperature annealing treatments, three sample sets were prepared by the electroless deposition of Pd and Ag on the as-received 0.5 μm media grade PHST coupons (1.5x1.0 c015) as representative batches of Pd/PHST, Ag/PHST binary and Pd/Ag/PHST ternary systems. Each sample set was consisted of 4 specimens and all the metal depositions on PHST coupons were carried out for 30 minutes. The thickness estimated gravimetrically for the Pd/PHST, Ag/PHST and Pd/Ag/PHST specimens were in the order of 0.15 μm, 0.1 μm and 0.25 μm, respectively, which were all within the detection limit of the X-ray penetration depth as discussed in Section 7.2.2.

Similar to the study discussed in Chapter 7, the annealing treatments for the Pd/PHST, Ag/PHST and Pd/Ag/PHST specimens were carried out at 500°C, 600°C, 700°C and 800°C for 20 hours in H_2 (designated as T[°C]/H_2/20h) and at a heating/cooling rate of 5°C/min. The X-ray diffraction patterns for the Pd/PHST system annealed at 500°C, 600°C, 700°C and 800°C are shown in Figure 8-2.

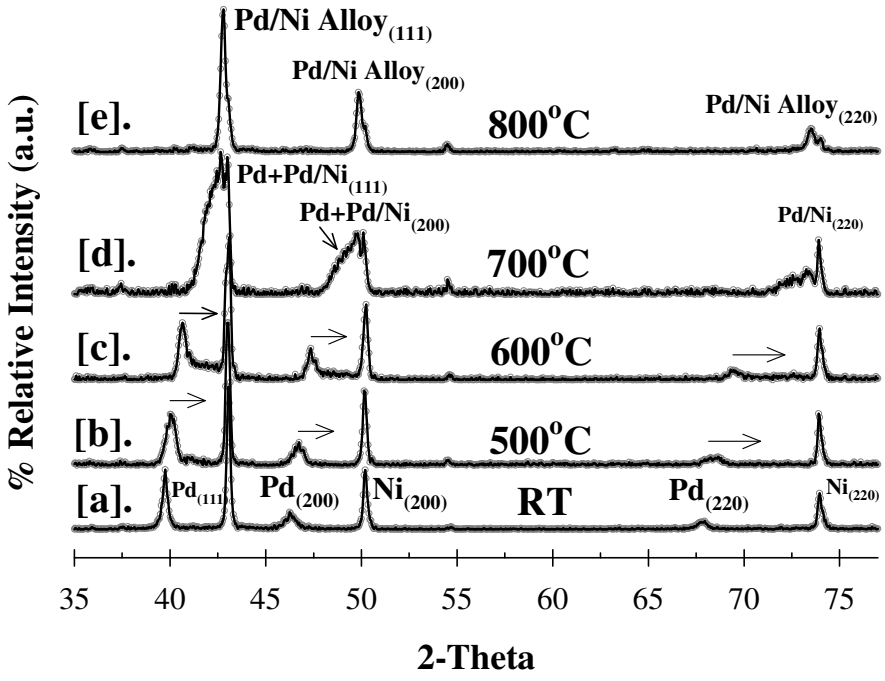

Figure 8-2: X-ray diffraction patterns for the Pd/PHST samples at [a].RT and after annealing at [b]. 500°C/H_2/20h, [c]. 600°C/H_2/20h, [d]. 700°C/H_2/20h and [e]. 800°C/H_2/20

For the sample annealed at 500°C/H_2/20h, XRD pattern in Figure 8-2[b] showed a small shift in fcc peaks of Pd towards the characteristic peaks of PHST substrate compared to the XRD pattern of the fresh Pd deposit shown in Figure 8-2[a]. It should be noted that Ni is the major component in PHST substrate with a compositional range of 50-63 wt% and with the low melting point temperature of 1453°C. Therefore, the discussion regarding the annealed Pd and Ag deposits on PHST is directed to the interactions of Pd/Ni, Ag/Ni binary and Pd/Ag/Ni ternary systems as shown by the Pd/Ni annotations in Figure 8-2. Upon annealing at 600°C/H_2/20h, shown in Figure 8-2[c], a Pd-rich Pd/Ni alloy phase appeared to form as shoulders between the characteristic Pd and the support peaks. Since the annealing temperature of 600°C was above the Tamman temperature of Ni (T_{Tamman}: 590°C) the intermetallic diffusion of the support metals, Ni in particular, into the Pd layer was more pronounced with the further increase in the annealing temperature to 700°C. The XRD pattern in Figure 8-2[d] indicated the formation of a Ni-rich Pd/Ni alloy upon annealing at 700°C/H_2/20h. The final diffusion

treatment conducted at 800°C/H_2/20h, resulted in the formation of a pure Pd/Ni fcc-alloy phase as shown in Figure 8-2[e]. It is also possible for the new-alloy phase to contain trace amounts of Cr and Fe since the annealing temperature of 800°C was above the Tamman temperatures of both Cr (T_{Tamman}: 792°C) and Fe (T_{Tamman}: 632°C) metals. According to the Pd/Ni binary phase diagram (Nash, 1990), Pd and Ni metals are completely miscible both in solid and liquid phases similar to that of Pd/Fe system discussed in Section 7.2.2.1. SEI micrographs for the annealed Pd/PHST samples are shown in Figure 8-3.

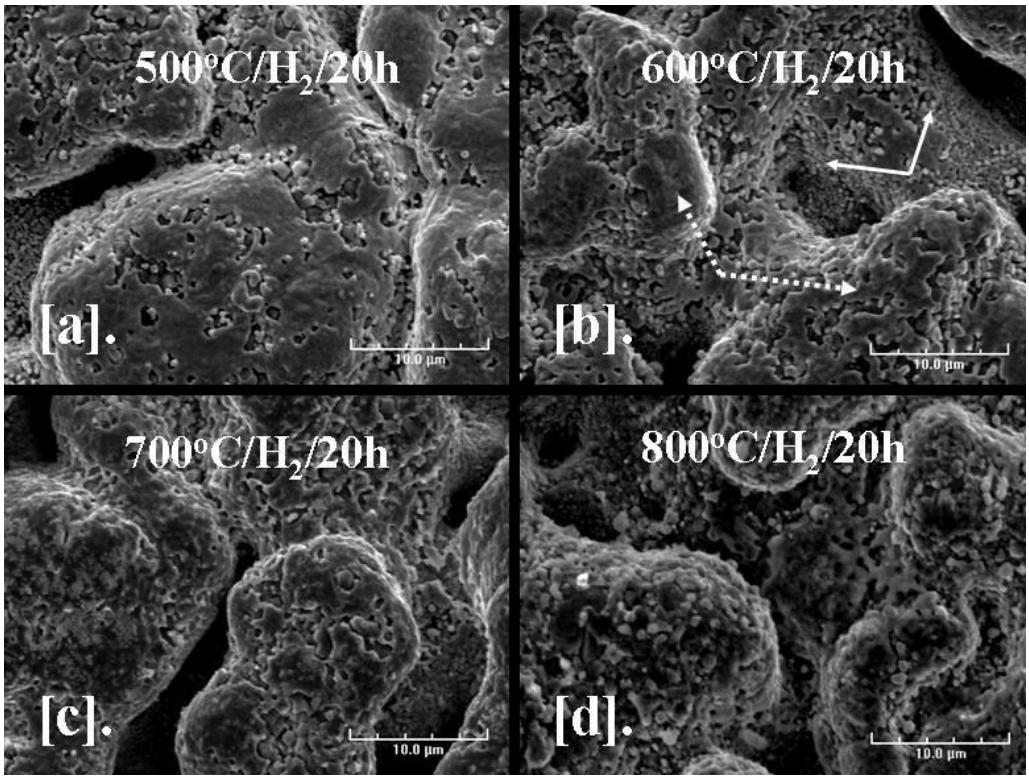

Figure 8-3: SEI micrographs on the surface topology of the annealed Pd/PHST system at [a]. 500 °C/H_2/20h, [b]. 600 °C/H_2/20h, [c]. 700 °C/H_2/20h and [d]. 800 °C/H_2/20h

In comparison to the fresh Pd deposit on PHST (Figure 8-1[b]), annealing at 500°C/H_2/20h resulted in a smooth surface morphology as shown in Figure 8-3[a], which was attributed to the mild sintering of the Pd clusters. Indeed, the spherical Pd clusters on the surface of the support were still visible (Figure 8-1[b]). However, the surface morphology of the coupon after annealing at 600°C/H_2/20h had two distinct features, which were in the form of large clusters located at the plateaus (arrows with dashed-lines

in Figure 8-3[b]) and small spherical particles mainly distributed at the regions covering the pore walls and valleys (arrows with solid-line in Figure 8-3[b]). This was also in agreement with the co-existing pure-Pd and Pd-rich Pd/Ni alloy phases shown by the XRD pattern in Figure 8-2[c]. As shown in Figure 8-3[c], the spherical Pd clusters disappeared and the surface morphology changed to form uniformly distributed large clusters after annealing at 700°C/H_2/20h. According to the XRD pattern in Figure 8-2[d], these large clusters represent a Ni-rich Pd/Ni alloy phase. It was interesting to note that the surface morphology of the Pd/Ni clusters after annealing at 800°C (Figure 8-3[d]) appeared to be quite different from the coupons annealed at lower temperatures between 500°C-700°C. The change in the surface morphology after annealing at 800°C/H_2/20h was attributed to the high concentration of Ni, as evidenced by the noticeable peak shift in Figure 8-2[e] indicating the formation of a Ni-rich Pd/Ni alloy phase. Since the annealing temperature of 800°C was higher than the Tamman temperatures of the all the support metals (Ni, Cr and Fe), the change in the morphology in Figure 8-3[d] might also be associated with the formation of other intermetallic alloy phases such as Pd/Cr and Pd/Fe.

The XRD patterns for the Ag/PHST samples after annealing at 500°C, 600°C, 700°C and 800°C are shown in Figure 8-4. For the temperature range investigated, XRD patterns for the Ag/PHST system indicated no peak shifting and/or broadening for the characteristics peaks located at (111), (200) and (220) planes indicating that there were no phase transformations between Ag and the support metals. As confirmed by the Ag/Ni binary phase diagram (Singleton, 1990), similar to the Ag/PSS system discussed in Section 7.2.2.2, Ag and Ni metals exert immiscibility both in solid (Figure 8-4) and liquid phases.

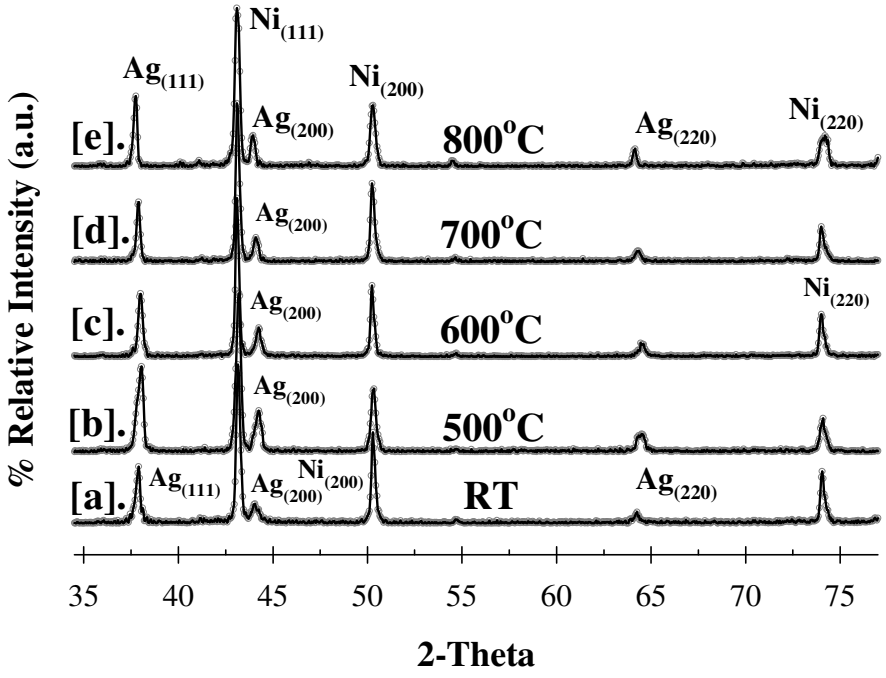

Figure 8-4: X-ray diffraction patterns for the Ag/PHST samples at [a].RT and after annealing at [b]. 500°C/H_2/20h, [c]. 600°C/H_2/20h, [d]. 700°C/H_2/20h and [e]. 800°C/H_2/20

The SEI micrographs in Figure 8-5 show the annealed morphologies of the Ag/PHST. In comparison to the fresh Ag deposit shown in Figure 8-1[c], the size of the Ag clusters appeared to increase with the increasing annealing temperature (Figure 8-5). A similar increase in the size of the Ag clusters with temperature was observed for the Ag/PSS system discussed in Section 7.2.2.2. It was also interesting to note that the Ag clusters became significantly larger (2-8 μm) and even faceted (Figure 8-5[d]) after annealing at 800°C/H_2/20h.

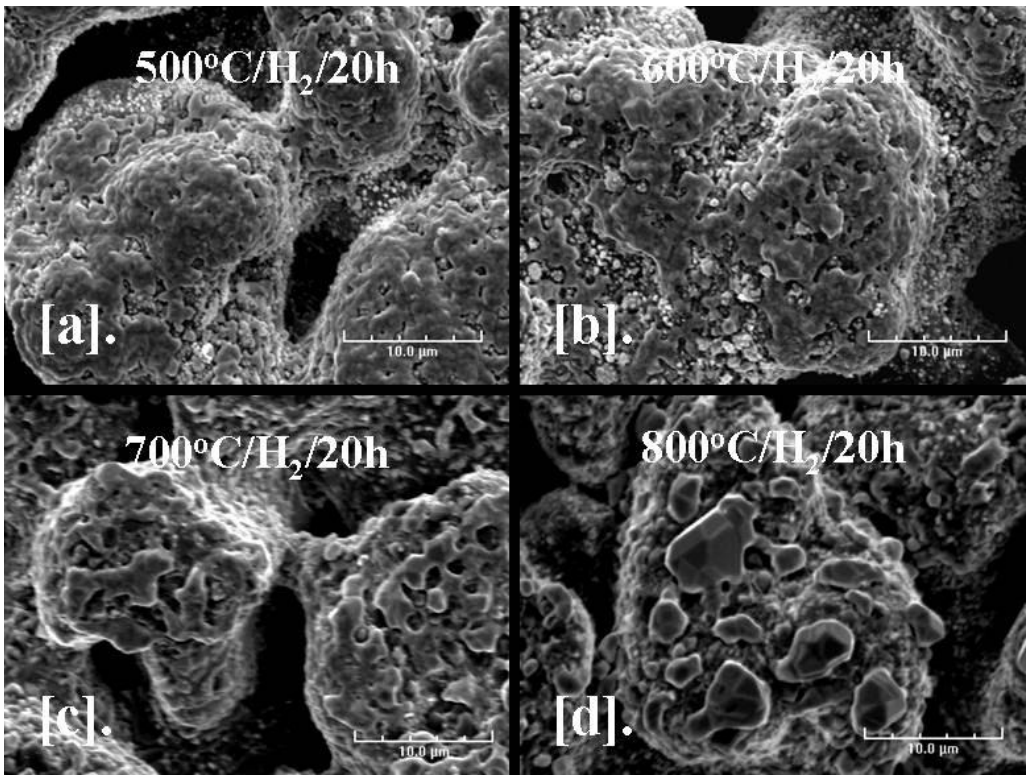

Figure 8-5: SEI micrographs on the surface topology of the annealed Ag/PHST system at [a]. 500 °C/H_2/20h, [b]. 600 °C/H_2/20h, [c]. 700 °C/H_2/20h and [d]. 800 °C/H_2/20h

For the Pd/Ag/PHST ternary system, XRD patterns given in Figure 8-6 indicated that the formation of the Pd/Ni alloy phase followed a similar trend as observed in the case of Pd/PHST binary system shown in Figure 8-2. The nucleation of the Pd/Ni alloy phase first started upon annealing at 500°C/H_2/20h and became more pronounced after annealing at 600°C/H_2/20h, as shown in Figure 8-6[b] and Figure 8-6[c], respectively. At 700°C, a Ni-rich Pd/Ni alloy phase was formed due to significant Ni segregation into the Pd layer (Figure 8-6[d]). As shown in Figure 8-6[e], annealing at 800°C/H_2/20h, resulted in the formation of a pure Pd/Ni fcc alloy phase.

Higher annealing temperatures resulted in an increase in the Ni content of the Pd/Ni alloy phase. On the other hand, characteristic peaks for the Pd/Ag alloy phase formed after annealing at 500°C/H_2/20h (Figure 8-6[b]) shifted towards the pure-Ag plane at higher temperatures, indicating that the diffusion between Pd and Ni was more dominant.

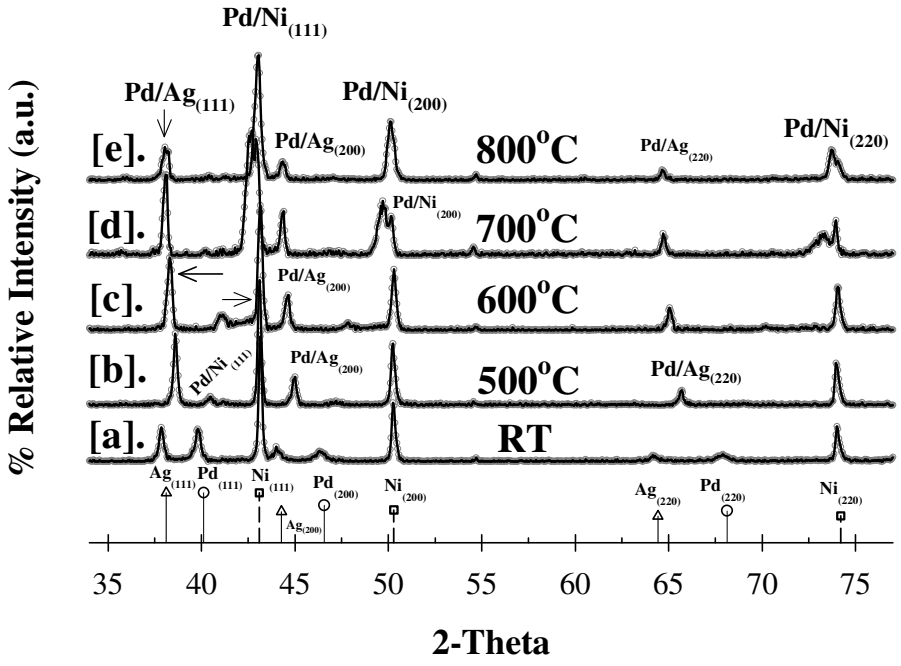

Figure 8-6: X-ray diffraction patterns for the Pd/Ag/PHST samples at [a].RT and after annealing at [b]. 500°C/H_2/20h, [c]. 600°C/H_2/20h, [d]. 700°C/H_2/20h and [e]. 800°C/H_2/20

The SEI micrographs for the annealed morphologies of the Pd/Ag/PHST samples shown in Figure 8-7. It is interesting to note that the topological features of the annealed Pd/Ag/PHST samples in Figure 8-7[a]-[d] appeared to be similar to that of the Pd/PHST and Ag/PHST systems shown in Figure 8-3 and Figure 8-5, respectively. The spherical clusters, shown in Figure 8-7[a] and [b], disappeared and the surface morphology changed to form uniformly distributed large clusters after annealing at 700°C/H_2/20h (Figure 8-7[c]). Upon annealing at 800°C/H_2/20h, the surface morphology shown in Figure 8-7[d] was mainly in the form of uniform Pd-like spherical clusters co-existing with randomly distributed and Ag-like faceted large clusters, which appeared to look similar to the surface morphologies shown in Figure 8-3[d] and Figure 8-5[d], respectively.

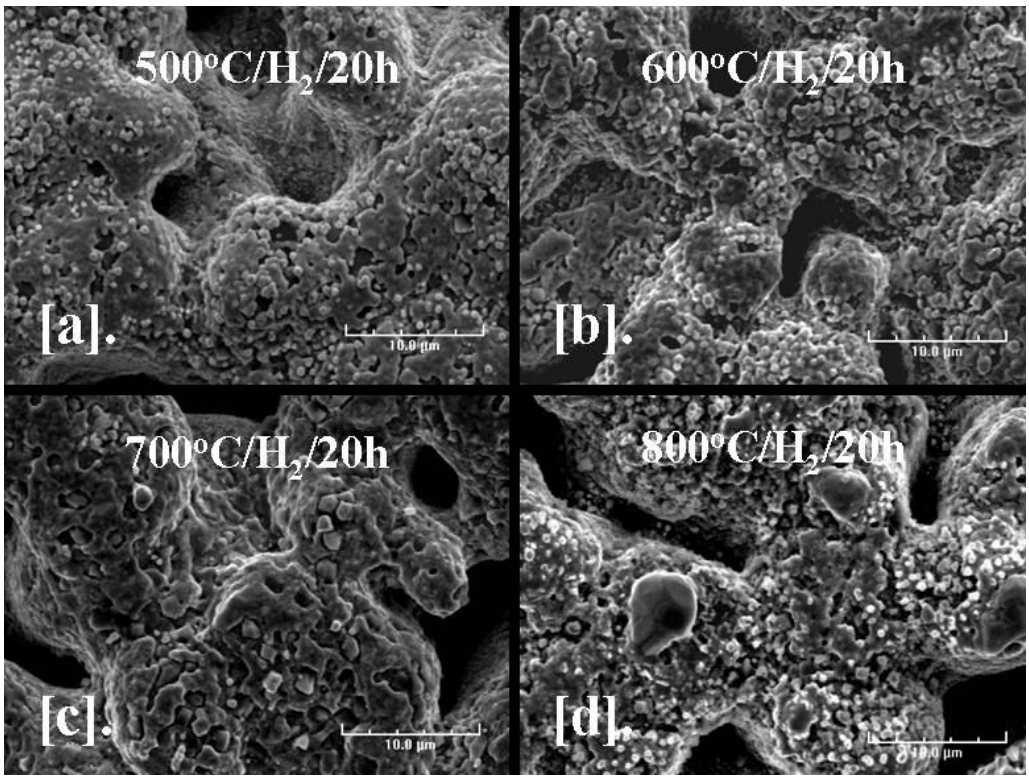

Figure 8-7: SEI micrographs on the surface topology of the annealed Pd/Ag/PHST system at [a]. 500 °C/H_2/20h, [b]. 600 °C/H_2/20h, [c]. 700 °C/H_2/20h and [d]. 800 °C/H_2/20h

Similar to the Ag/Fe system discussed in Section 7.2.2.2, XRD phase analysis of the Ag/PHST system coupled with the SEI micrographs (Figure 8-5) and the data from the Ag/Ni binary phase diagrams (Singleton, 1990), indicated that the Ag might be an excellent intermetallic diffusion barrier due to its both solid and liquid phase immiscibility with the support metal (Fe, Cr and Ni).

However, the validation of the Ag-immiscibility concept via the testing of the composite Pd/Ag membrane 012, prepared on an un-oxidized PSS support, resulted in a 24% decline in the initial H_2 permeance due to the intermetallic diffusion, which was monitored over a period of ~450 hours at 500°C. Hence, the long-term testing of the composite Pd/Ag/PSS membrane 012 at 500°C (Figure 7-15) further indicated that the Ag-layer, formed by the conventional electroless plating baths (Table 3-4), did not provide enough resistance against the intermetallic diffusion due to its non-uniform deposition morphology. It appears that the formation of uniform Ag layers is of great importance for the long-term chemical and thermal stability of the composite Pd/Ag alloy

membranes supported on un-oxidized Fe and/or Ni-rich porous sintered metal supports. The modification of the conventional Ag plating bath in order to achieve uniform Ag deposition layer will be discussed next.

8.4. Modification of the Conventional Electroless Ag Plating Bath

In an effort to improve the deposition morphology and to achieve uniform Ag layers on porous metal supports, the electroless plating of Ag was compared to several different "silvering" techniques including the glucose, Rochelle salt and hydrazine methods, which were summarized by Mallory and Hajdu (1990) in greater detail. Although the use of "silvering" methods (Mallory and Hajdu, 1990) led to a "mirror-like" metallic-shiny Ag layers that formed instantaneously at room temperature, the Ag layer deposition mainly took place at the inner walls of the plating cells and very little on the porous metal surface.

However, it was interesting to note that the Ag metal ion concentrations used for the glucose, Rochelle salt and hydrazine methods were 0.21M, 0.49M and 0.15M, respectively, and significantly higher than the concentration of the Ag (3.05 mM) used in the regular electroless Ag plating bath given in Table 3-4. Since fast nucleation rates are required to avoid particle growth by the Ostwald ripening at the expense of shrinking small particles (Porter and Easterling, 1992), a concentrated Ag plating solution with an initial Ag ion concentration of 61.2 mM was used to enhance the Ag deposition morphology by increasing the total number of Ag nucleation sites that might alter the growth of the surface dendrites. Although the stability of the concentrated Ag plating bath was limited to 20 minutes, the deposition on the porous surface had a creamy-white appearance and a uniform texture. It was also observed that the stability of the concentrated Ag bath was further improved and lasted as long as 60 minutes when it was applied on surfaces with Ag deposition and by using hydrazine concentrations less than 3.6 mM. The Ag layer formed by the concentrated Ag plating bath was termed as the "pure-Ag barrier" layer and successfully utilized for the synthesis of Pd/Ag layers with a Ag content as high as 30-40 wt%. Having a 3-5 μm thick pure-Ag barrier layer should also serve a dual purpose by providing resistance against intermetallic diffusion due to

the immiscibility of the Ag with the support metals and by enhancing the H_2 permeability if the diffusion between the Ag and the top Pd layer leads to a uniform Pd/Ag alloy. Furthermore, pure-Ag barrier layer was used subsequently with the $Al(OH)_3$ grading technique, described in Section 6.4.2, in order to prepare thin composite Pd/Ag membranes on porous Inconel supports.

8.5. The Effectiveness and the Stability of the "pure-Ag Barrier" Layer Against Intermetallic Diffusion

To recapitulate the effectiveness and the stability of the pure-Ag barrier layer against intermetallic diffusion, the synthesis of Pd/Ag membrane layers on 0.1 μm media grade, ½" OD un-oxidized tubular Inconel supports were carried out via the combined use of the pure-Ag barrier layer deposition and the $Al(OH)_3$ grading technique in two different experimental settings, as schematically illustrated in Figure 8-8. While the pure-Ag barrier layer for the membranes 014 and 018 was formed after the $Al(OH)_3$ grading of the support surface as shown in Figure 8-8[a], the pure-Ag barrier layer for the membranes 019, 020 and 021 (Ma-64) were formed prior to the $Al(OH)_3$ grading step (Figure 8-8[b]), in order to provide extra resistance against the intermetallic diffusion by minimizing the contact area between the support surface and the top Pd layer.

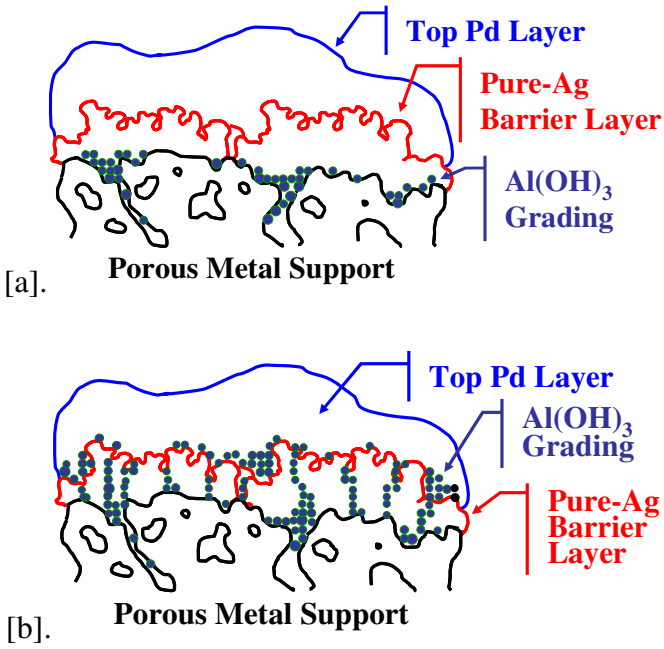

Figure 8-8: Schematic for the membrane synthesis procedure [a]. $Al(OH)_3$+pure-Ag Barrier Layer and [b].pure-Ag Barrier Layer+ $Al(OH)_3$

A comparison of the H_2 permeance at 500°C for all the Pd/Ag membranes prepared on un-oxidized Inconel supports is shown in Figure 8-9.

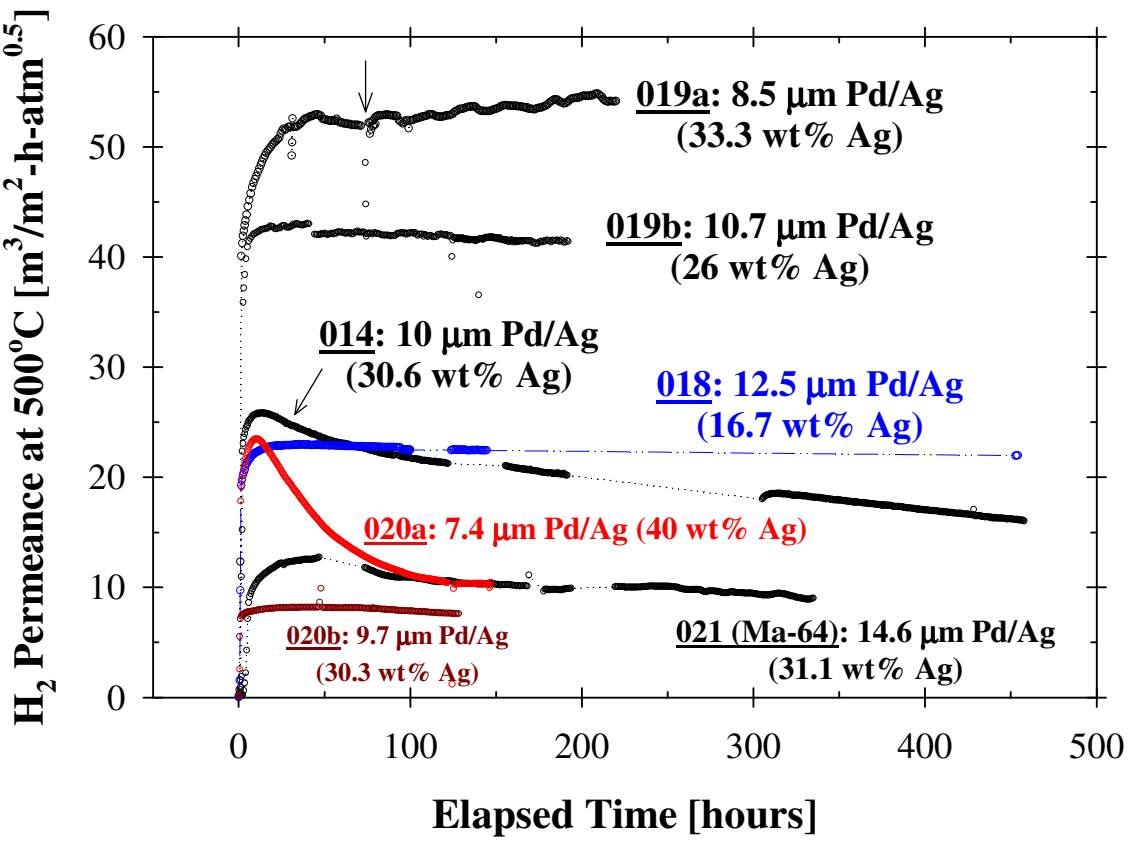

Figure 8-9: H_2 benchmarking at 500°C for the Pd/Ag membranes prepared on un-oxidized Inconel supports

The H_2 permeance of the 10 µm thick Pd/Ag (30.6 wt %) membrane 014 at 500°C was 25.8 m^3/m^2-h-$atm^{0.5}$ with an activation energy of 20.1 kJ/mol in the temperature range of 350-500°C. As can be seen in Figure 8-9, 38% of the initial H_2 permeance of the membrane 014 deteriorated at 500°C over a period of ~450 hours. Nonetheless, the final H_2/He selectivity at 500°C was as high as ~250. In order to elucidate the cause of the 38% loss in H_2 permeance and to asses the effectiveness of the pure-Ag barrier layer (3.4 µm) as an intermetallic diffusion barrier, the cross-sectional SEI and EDX analyses for the membrane 014 are shown in Figure 8-11.

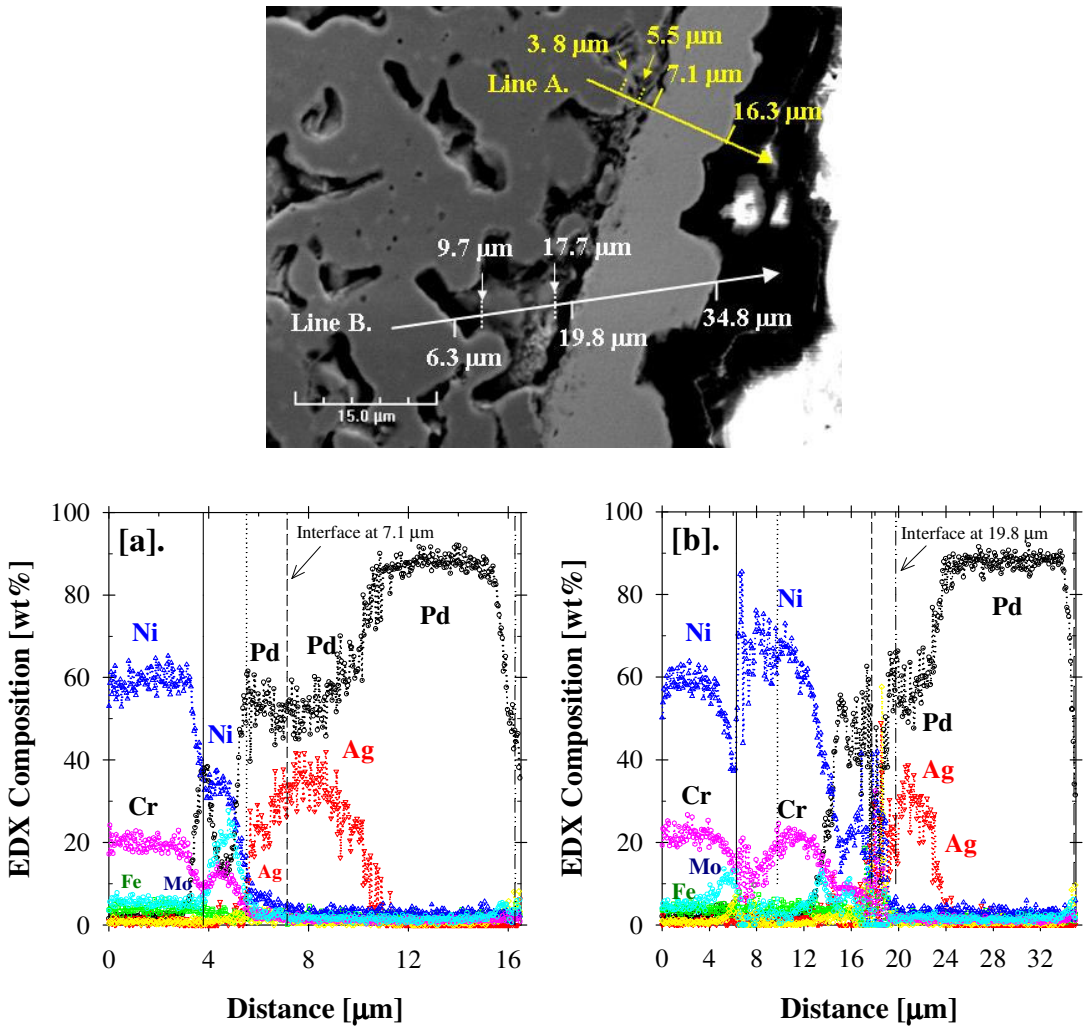

Figure 8-10: EDX cross-section line scans A and B for the membrane 014

In Figure 8-10, the interface between the porous support metal and the Pd/Ag layer for the EDX line scans A and B were marked at 7.1 µm and 19.8 µm, respectively. As can be depicted from both the line scans given in Figure 8-10[a] and [b], there were no intrusion of support metals into the dense Pd/Ag layer beyond the marked interfaces. As can be depicted in Figure 8-10[a] and [b], the pure-Ag barrier layer at the support membrane interface had a sharp gradient with a Ag composition as high as 40 wt%. This clearly indicated that the pure-Ag barrier layer formed at the support membrane interface, located between 6-11 µm and 19-24 µm for the line scans A and B, respectively, was effective against intermetallic diffusion. It was also interesting to note that the surface marked between 5.5 µm and 7.1 µm in line scan A in Figure 8-10 showed a small gradient of Ni concentration. This unexpected intermetallic diffusion at a relatively Ag-

rich surface was attributed to the "horophilic" nature of the Pd metal. By definition, horophilic refers to the boundary related intercrystallite diffusion processes. In this respect, Arkharov (1954) describes the elements, which tend to accumulate preferentially in the intercrystallite transition zone, as horophilic. Arkharov and Yunikov (1954) further postulate that the horophilic characteristics might be the main reason why steels apparently identical in analysis and microstructure might differ in mechanical properties. According to Arkharov and Yunikov (1955), when a horophilic element is added to a metal, it tends to concentrate at its grain boundaries, where its concentration becomes much higher than the average and facilitates the diffusion of a third element, which is originally immiscible with the metal. The Ag-Fe-Pd and/or Ag-Ni-Pd ternary system is an excellent illustration of the situation, Pd being 100% soluble in Fe and/or Ni and Ag being immiscible both in solid and liquid phases with Fe and/or Ni but completely miscible with Pd. Arkharov and Yunikov (1955) have reported that, the Ag diffusion along grain boundaries of γ-Fe was possible when it was only enriched with the horophilic Pd. On the other hand, no Ag diffused in Fe free from Pd. Therefore, it should be taken into consideration that the horophilic nature of Pd might alter the solid immiscibility of Ag with Fe and/or Ni. Therefore, given enough time and temperature in the absence of an effective barrier layer, a Pd/Ag alloy might be as vulnerable to intermetallic diffusion as the pure Pd layer. Indeed, the small gradient of Ni diffusion at the region marked between 5.5 μm and 7.1 μm in line scan A of Figure 8-10 indicated that the intermetallic diffusion of Ni into the Pd/Ag layer took place at a slower rate when the Ag content was less than ~20%. Furthermore, careful examination of the cross-section of the membrane 014 showed that the pure-Ag layer deposition was not uniform through out the membrane thickness. As shown in Figure 8-11, the intermetallic diffusion of Ni into the dense Pd layer was significant (up to a distance of ~10 μm) when there were no Ag at the interface (marked at 4.65 μm).

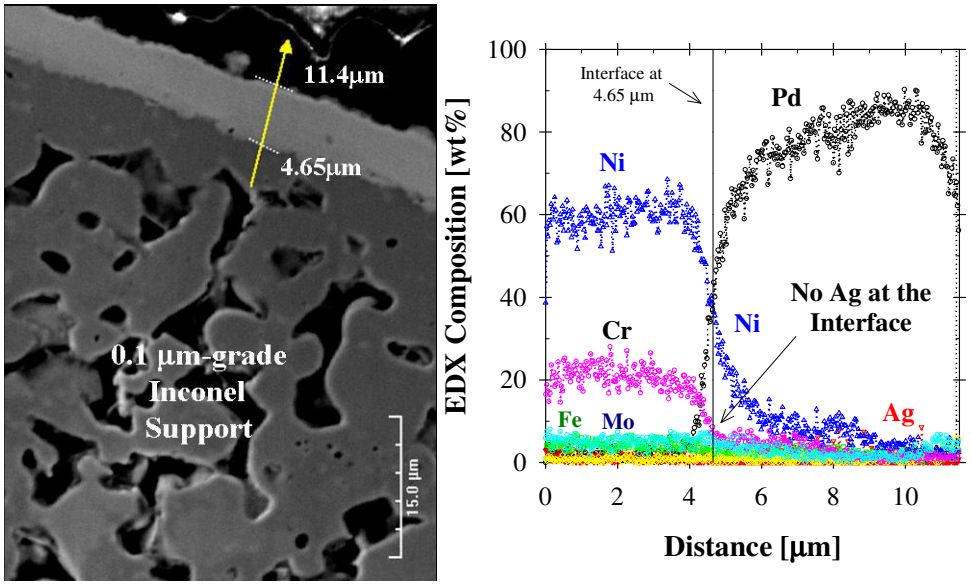

Figure 8-11: EDX line scan for the membrane 014

The EDX cross-section data shown in Figure 8-10 and Figure 8-11 indicated that the intermetallic diffusion mainly took place only at the regions where the Ag composition was below ~30%. No intermetallic diffusion was observed at the regions which were initially Ag-rich. Therefore, the effectiveness of the pure-Ag barrier layer against intermetallic diffusion was concluded to be strongly depended upon the electroless plating morphology of Ag. Due to the presence of the concentration gradients that were originated from the deposition morphology, the intermetallic diffusion was believed to occur at different rates at different regions of the surface. However, the overall effect was the associated steady decline in hydrogen permeation flux as observed in the case of membrane 014 at 500°C for ~450 hours (Figure 8-9).

In the case of a 12.5 μm thick Pd/Ag (16.7 wt %) membrane 018, a stable H_2 permeance at 500°C was 22.6 m^3/m^2-h-$atm^{0.5}$, however, the H_2/He selectivity of membrane 018 was below 100 after a relatively short period of testing at 500°C (~100 hours). The membrane was tested at 550°C in H_2 for an additional ~160 hours in order to complete the alloying between the as-deposited Pd and Ag layers and to test the stability of the pure-Ag barrier layer against intermetallic diffusion by the cross-sectional analyses of the annealed membrane. The EDX cross-sectional line scans and the SEI micrographs are shown in Figure 8-12.

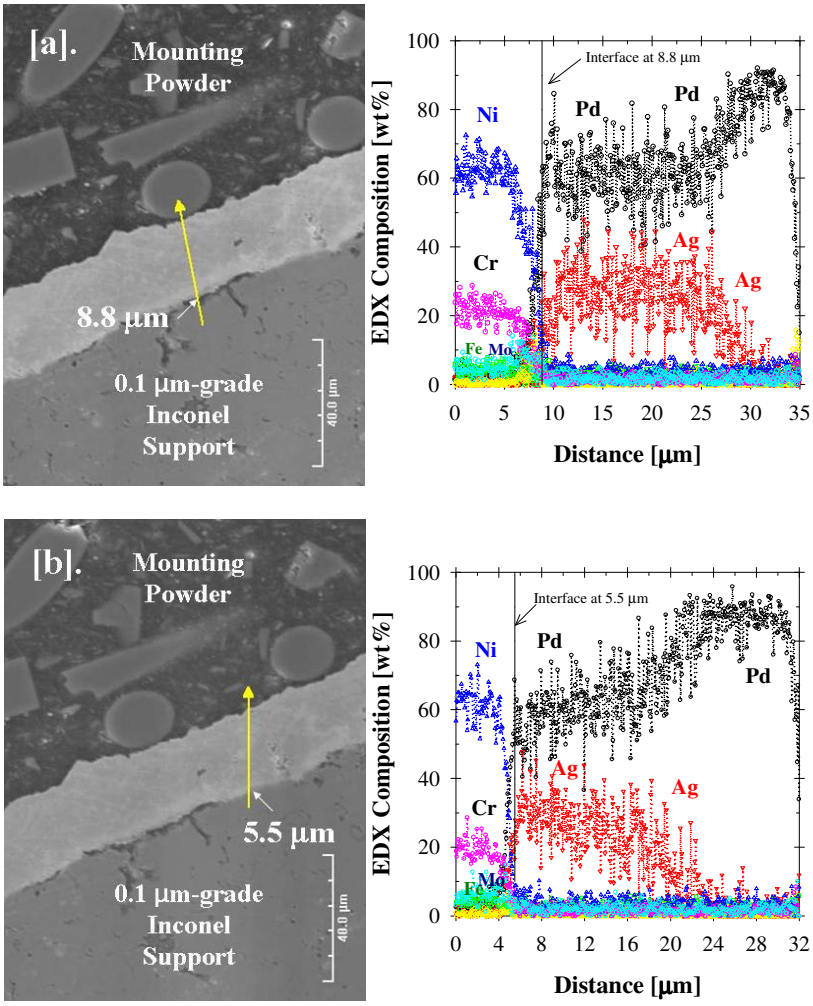

Figure 8-12: EDX cross-sectional line scan analysis of membrane 018

In Figure 8-12[a] and [b], the interface between the porous support metal and the Pd/Ag layer was located at 5.5 µm and 8.8 µm, respectively. According to the EDX line scans shown in Figure 8-12[a] and [b], the membrane layer can be distinguished by two distinct regions; a Pd-rich Pd/Ag alloy layer with an average Ag composition of ~30 wt% with a pure-Pd layer on the top. The presence of a pure-Pd layer indicated that the alloying of the as-synthesized Ag and Pd layers was not complete even after ~160 hours of annealing treatment conducted at 550°C in H_2. Moreover, the intrusion of the Ni metal into the Pd/Ag membrane layer was estimated to be less than 1-2 µm from both line scans shown in Figure 8-12[a] and [b], respectively. Although the membrane 018 was annealed at a temperature as high as 550°C, there was no indication of a loss in H_2 permeance that

might be associated with the intermetallic diffusion of support metals into the membrane layer. It was also interesting to note that the average SEM thickness of the membrane 018 was found to be 25 μm, which was almost ~2 times higher than the thickness estimated gravimetrically during the synthesis (12.5 μm). Further analysis of the surface morphology indicated the presence of macroscopic surface defects, as shown in Figure 8-13. The regions annotated as A and B on the SEI micrographs in Figure 8-13 was located at the porous surface in proximity to the upper weld area. Both defects located at regions A and B were as large as 2000 μm in length and 1000 μm in width, which can be seen in a greater detail by the SEI micrographs taken at a higher magnification in Figure 8-13. Therefore, the low H_2/He selectivity of membrane 018 was due to the formation of the macroscopic surface defects shown in Figure 8-13.

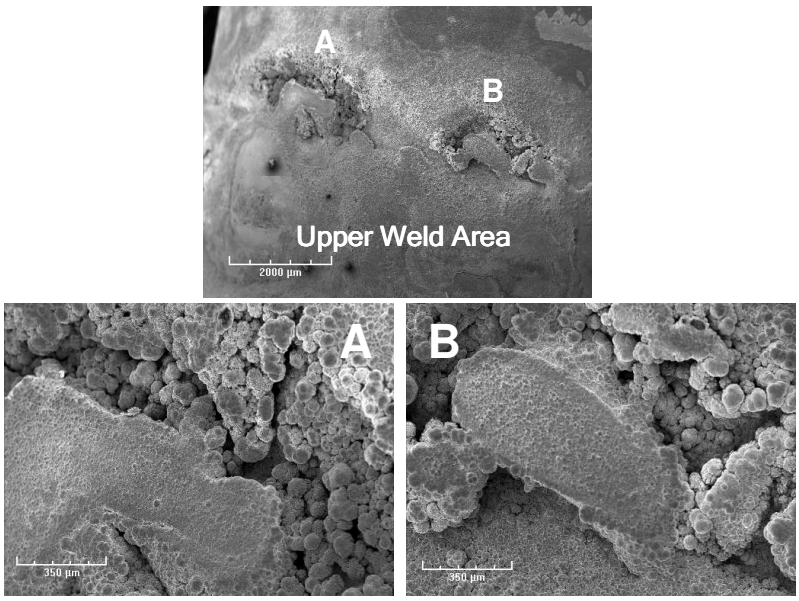

Figure 8-13: Top SEI micrographs revealing the surface morphology at the upper weld area for membrane 018

The synthesis of Pd/Ag membranes 019a, 020a and 021 (Ma-64) according to the procedure shown in Figure 8-8[b], led to interesting observations. The thickness of the pure-Ag barrier layers, formed prior to $Al(OH)_3$ grading, for the membranes 019a, 020a and 021 (Ma-64) were 3.1, 3.3 and 5.0 μm, respectively. For a 8.5 μm thick Pd/Ag (33.3 wt% Ag) membrane 019a, shown in Figure 8-9, the H_2 permeance at 500°C was as high as 52 m^3/m^2-h-$atm^{0.5}$. However, the H_2/He selectivity of membrane 019a dropped below a

value of 100 shortly after the first ~100 hours of testing (annotated by an arrow in Figure 8-9). Repairing of the membrane 019a with an additional 2.2 μm Pd layer resulted in a 10.7 μm thick Pd/Ag (26 wt% Ag) with a stable H_2 permeance of 43 m^3/m^2-h-$atm^{0.5}$ at 500°C (shown in Figure 8-9). However, similar to the performance of membrane 019a, the membrane 019b developed a significant leak shortly after the initial testing at 500°C. Similar to the characterization of membrane 018, the membrane 019b was annealed at 550°C for 150 hours.

Furthermore, Figure 8-9 shows the H_2 permeance of the 7.4 μm thick Pd/Ag (40 wt% Ag) membrane 020a.As can be depicted in Figure 8-9, the H_2 permeance at 500°C initially increased to a peak value of 23.5 m^3/m^2-h-$atm^{0.5}$ and then declined steadily to a stable value of 10.4 m^3/m^2-h-$atm^{0.5}$ after a relatively short testing period of ~125 hours. Indeed, it was observed that initial selectivity (H_2/He) at 500ºC declined from a value of 1950 to only 50 only after a total testing period of 150 hours. Similarly, repairing the membrane 020a with an additional 2.2 μm Pd layer resulted in a 9.7 μm thick Pd/Ag (30 wt% Ag) membrane 020b with a stable H_2 permeance of only 8.2 m^3/m^2-h-$atm^{0.5}$ at 500°C (shown in Figure 8-9). The membrane 020b was tested for an additional 200 hours at 550°C prior to the cross-sectional analyses, which are shown in Figure 8-14.

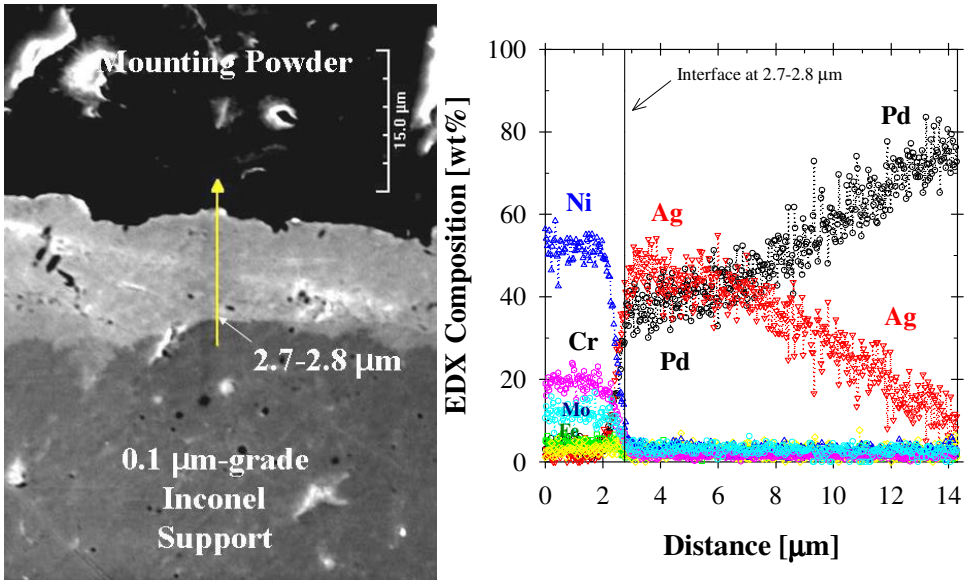

Figure 8-14: Cross-sectional SEI and EDX Analyses of Membrane 020ab

As can be seen in Figure 8-14, the EDX line scan analysis of the cross-section of membrane 020b indicated that there were no intrusion of the support metals in the Pd/Ag layer as evidenced by the sharp interface, which was marked at 2.8 µm between the Inconel support metal and the Pd/Ag layer. In addition, the Pd/Ag alloy phase formed at the interface, shown in Figure 8-14, had a Ag content as high as 50 wt%, clearly indicating that the decline in the H_2 permeance of membrane 020a (Figure 8-9), was due to the formation of a Ag-rich Pd/Ag alloy phase rather than the intermetallic diffusion. Since the thickness of the pure-Ag barrier layer for the 14.6 µm thick Pd/Ag (31.1 wt% Ag) membrane 021 (Ma-64) was as high as 5 µm, the decline in H_2 permeance from 12.6 to 9 m^3/m^2-h-$atm^{0.5}$ at 500°C over a period of ~160 hours, as shown in Figure 8-9, was also attributed to the formation of a Ag-rich Pd/Ag alloy phase at the support membrane interface. It should be also noted that the characterization of membrane 021 (Ma-64) also included a ~75 hours testing at 550°C similar to the membranes 019 and 020.

The long-term H_2 characterization and detailed cross-sectional SEI and EDX analyses of the composite Pd/Ag membranes shown in Figure 8-9 gave strong evidence that the 3-5 µm thick pure-Ag barrier layers provided improved resistance against intermetallic diffusion in the temperature range of 500-550°C, with no noticeable decline in the H_2

permeation flux. In addition, the main advantage of the pure-Ag barrier layer appeared to be the possibility of forming Ag-rich, yet, thin Pd/Ag membranes layers.

Furthermore, the pure-Ag barrier layer can also be utilized as an additional barrier layer and used in combination with the *in-situ* oxidation technique (Ma *et al.*, 2000) for the high temperature annealing of the as-synthesized Pd/Ag layers.

8.6. *in-situ* Oxidation of the Ni-Rich Porous Sintered Metal Supports

Due to their heat resistance nature, Ni-rich porous metal supports (i.e., PHST, Inconel) require higher oxidation temperatures in order to form an effective oxide barrier layer against intermetallic diffusion. The differences in the chemical compositions between Fe-rich PSS and Ni-rich PHST and Inconel supports were given in Table 3-1. Although the formation of an intermetallic diffusion barrier via the *in-situ* oxidation of the PSS supports has been studied extensively as discussed in Section 2.3.2, there are no studies in the literature to account for the effects of temperature on the formation of an oxide-barrier by the controlled *in-situ* oxidation technique for the composite Pd and Pd/alloy membranes supported on Ni-rich porous sintered metal substrates.

For this purpose, four sets of both PSS and PHST coupons, each consisted of 5 pieces were oxidized at stagnant air over a temperature range of 400-800°C for 12 hours. The summary of the weight gains due to the oxide layer formation is shown in Figure 8-15. The x-axis in Figure 8-15 gives the oxide-layer weight gain per total area, which was estimated by assuming that the oxide layer formed entirely on the exterior surface for each coupon (~3 cm^2).

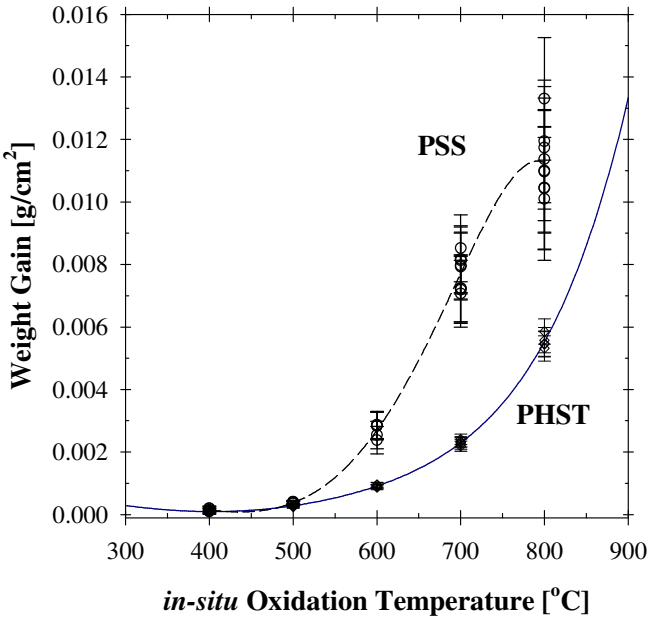

Figure 8-15: Weight gain vs. oxidation temperature for PHST and PSS coupons

As can be seen in Figure 8-15, the weight gains of the PSS samples noticeably increased with increasing oxidation temperature indicating the formation of a thicker oxide layer at temperatures higher than 600°C. In contrast, the weight gains of the PHST samples relatively were smaller than those of PSS in the temperature range of 400-700°C. A noticeable increase in the weight gains of the PHST samples were observed after oxidation 800°C.

Figure 8-16[a] and [b] shows the SEI micrographs of the PSS and PHST surfaces after oxidation at various temperatures in the range of 400-800°C, respectively. It can be seen in Figure 8-16[a] that the change in the PSS surface topology due to the formation of a thin oxide-layer starts at 500°C. At higher oxidation temperatures, 600°C and above, the surface of the PSS substrate changed substantially by the formation of a thick oxide-layer, which covered the entire surface uniformly including the pore walls and the mouths of the substrate.

On the other hand, the SEI micrographs for the PHST samples in Figure 8-16[b] indicated that the formation of a thin oxide layer for the oxidation temperature range of 500-700°C had no significant effect on the surface morphology. However, a noticeable

change was observed for the sample oxidized at 800°C indicating the presence of thicker oxide layer. These observations were in good agreement with the weight gains shown in Figure 8-15. For the PHST samples, the XRD patterns shown in Figure 8-18 further supported the fact that the nucleation of a thin Cr_2O_3 layer started at a temperature of 700°C (Figure 8-17[d]) and became more pronounced after oxidation at 800°C, which can be depicted from the peak broadening of the PHST substrate and the characteristic peak locations annotated by the arrows in Figure 8-17[e].

In the case of PSS samples, the XRD patterns in Figure 8-18 showed that the Fe_2O_3 layer nucleated at an oxidation temperature of 500°C and started to grow at 600°C. The XRD patterns shown in Figure 8-18[d] and [e] for the PSS samples oxidized at 700°C and 800°C, respectively, indicated the dominant presence of an Fe_2O_3 phase, which was identified as the Hematite. Furthermore, the EDX surface scan analysis confirmed that the higher oxidation temperatures resulted in the formation of Cr-rich and Fe-rich surface oxides for the PHST and PSS supports, respectively.

[a].

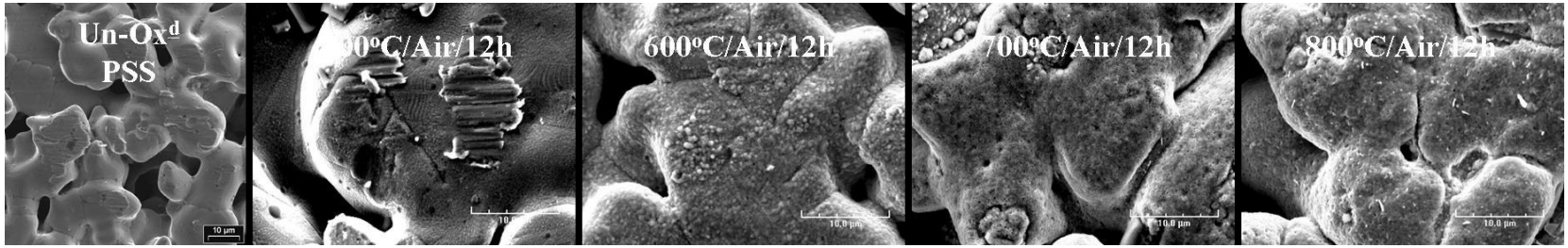

[b].

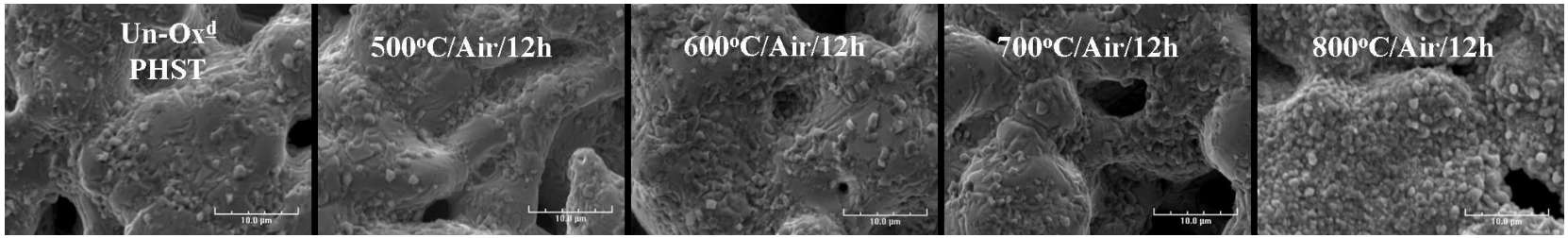

Figure 8-16: SEI surface morphology for [a]. PSS and [b]. PHST supports at different oxidation temperatures

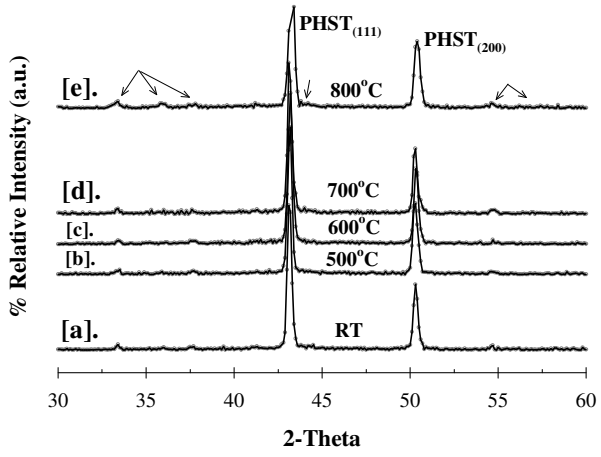

Figure 8-17: XRD patterns for the PHST samples at [a]. RT and after oxidation at [b]. 500℃, [c]. 600℃, [d]. 700℃ and [e]. 800℃

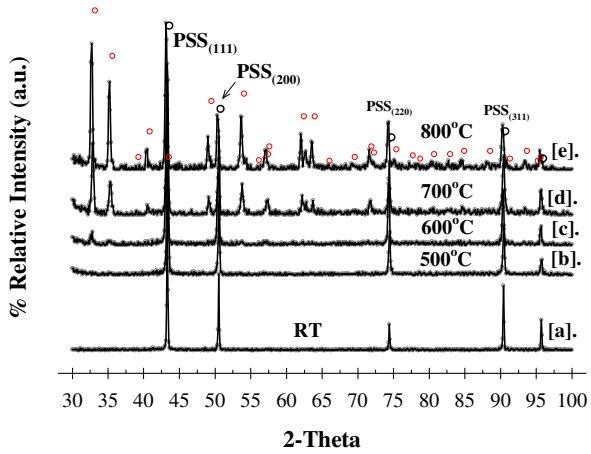

Figure 8-18: XRD patterns for the PSS samples at [a]. RT and after oxidation at [b]. 500℃, [c]. 600℃, [d]. 700℃ and [e]. 800℃

The oxide-barrier layers formed at 600°C by the *in-situ* oxidation of the PSS supports have provided long-term thermal stability against intermetallic diffusion as discussed in Section 5.3.1 and also shown by the permeance testing of membrane 011 at 500°C (Figure 5-2). Based on the oxide-layer weight gain data, the SEI micrographs and the XRD patterns in Figure 8-15, Figure 8-16[b] and Figure 8-17, an oxidation temperature of 800°C was chosen as the *in-situ* oxidation temperature for the Ni-rich porous sintered supports. The composite Pd and Pd/Ag membranes 015, 016, 017, 022, 025 and 026, as

listed in Table 3-5, were prepared on Inconel supports, which were oxidized at 800°C for 12 hours.

8.7. The Long-Term Stability of *in-situ* Oxidation of the Composite Pd/Ag Membranes formed by the Ni-Rich Porous Sintered Metal Supports

The stability of the oxide barrier formed by the *in-situ* oxidation of the Ni-rich porous sintered metal supports was compared via the long-term H_2 permeance testing of the composite Pd/Ag membranes 013 (Ma-46) and 015. The synthesis history for the membranes 013 (Ma-46) and 015 is shown in Figure 8-19. The synthesis of membranes 013 (Ma-46) and 015were carried out on as-received 0.1 μm media grade, 1" OD and 6" long PHST (un-oxidized) and a 0.1 μm media grade, ½" OD and 2" long Inconel, which was oxidized at 800°C for 12 hours. The modification of the PHST and Inconel support surfaces was achieved via pre-activated Al_2O_3 and $Al(OH)_3$ grading techniques, respectively, as discussed in Chapter 6. The synthesis of membrane 015 also included a 4 μm thick pure-Ag barrier layer deposition immediately after the surface grading with $Al(OH)_3$. On the other hand, the thickness of the Ag layer for the membrane 013 (Ma-46) was only 1.6 μm, which was deposited using the regular electroless Ag plating bath.

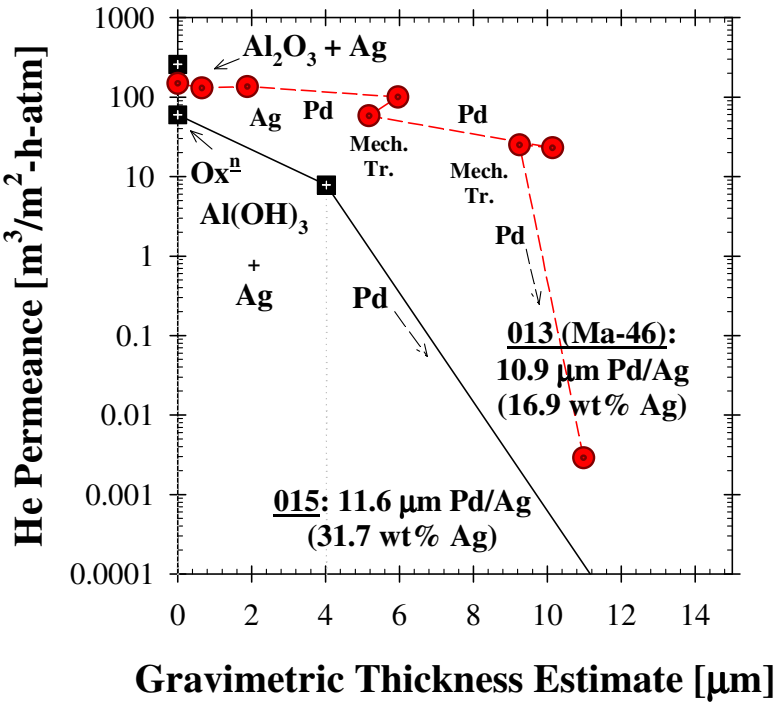

Figure 8-19: Synthesis history for the membranes 013 (Ma-46) and 015

For the 10.9 μm thick Pd/Ag/PHST (16.9 wt% Ag) membrane 013 (Ma-46), the H_2 initial permeance at 250°C, 350°C and 500°C were 7.2, 15.3 and 41.7 m^3/m^2-h-$atm^{0.5}$, respectively, which corresponded to an activation energy of 23.6 kJ/mol. The H_2 permeance history for the membrane 013 (Ma-46) is shown in Figure 8-20.

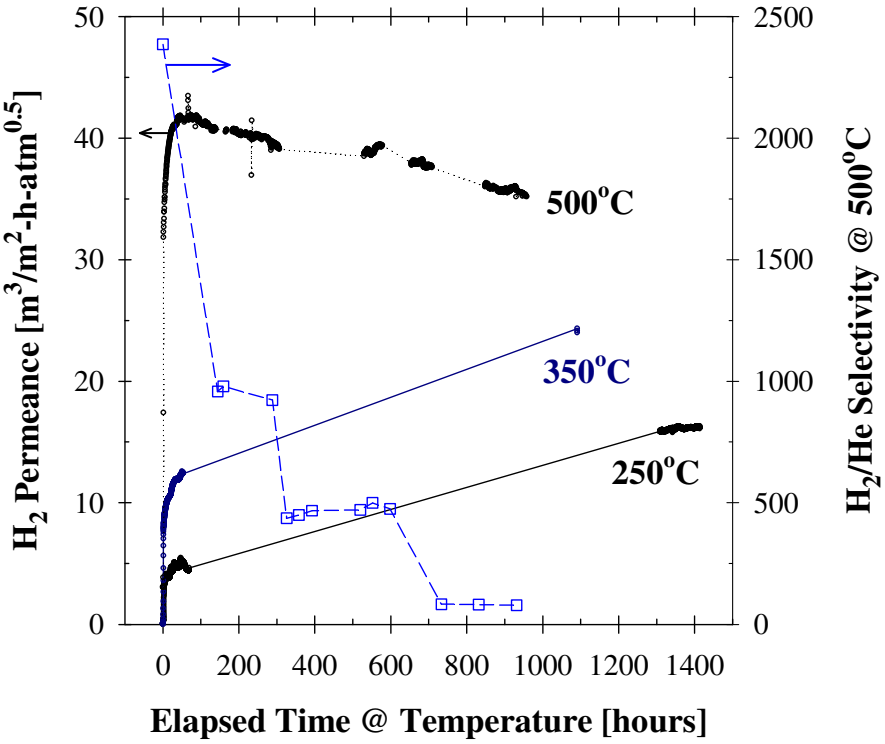

Figure 8-20: H_2 permeance history of membrane 013 (Ma-46) at 250℃, 350℃ and 500℃ (y-axis on the right refers to the H_2/He selectivity data measured at 500℃)

As can be depicted in Figure 8-20, the H_2 permeance of 013 (Ma-46) declined over a period of ~1000 hours during the testing at 500°C, which was attributed to the intermetallic diffusion of the support metals into the dense Pd/Ag layer. The total loss in H_2 permeance at 500°C was about 13.9% compared to the initial H_2 permeance of 41.7 m^3/m^2-h-$atm^{0.5}$. The additional Sieverts' law data measured at successive times during the permeance decline at 500°C are shown in Figure 8-21.

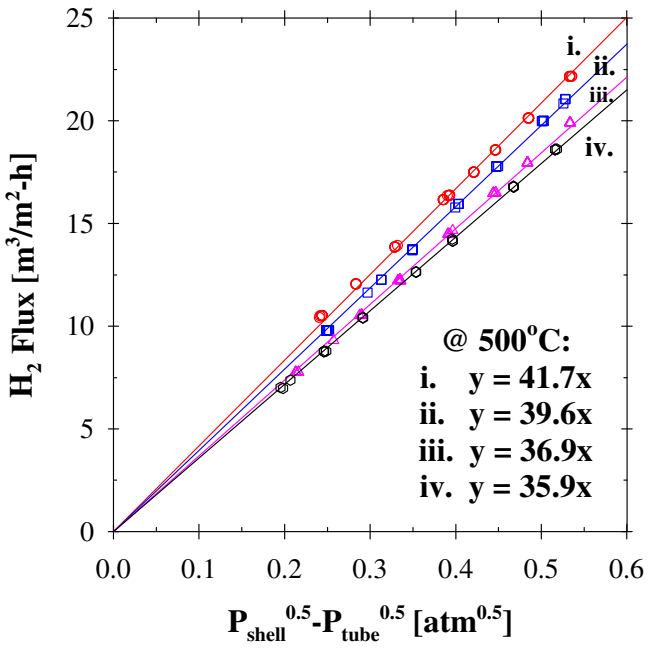

Figure 8-21: Sieverts' law plots for the membrane 013 (Ma-46)

Furthermore, it is noteworthy to mention that the H_2/He selectivity of membrane 013 (Ma-46) at 500°C was as high as 500 over a period of ~700, as shown in Figure 8-20. The formation of a noticeable helium leak at 500°C was observed only after ~700 hours. The final H_2/He selectivity at this temperature was ~80. Indeed, the activation energy measured during cooling-down from 500°C to 250°C in H_2 was 10.8 kJ/mol.

For the 11.6 μm thick Pd/Ag (31.7 wt% Ag) membrane 015, prepared on an oxidized Inconel support, the initial H_2 permeance at 350°C and 500°C were 16.9 and 34.8 m^3/m^2-h-$atm^{0.5}$, respectively. The activation energy in the temperature range of 350-500°C was 22.2 kJ/mol. The H_2 permeance history of membrane 015 is shown in Figure 8-22.

The long-term H_2 characterization of membrane 015 at 500°C (Figure 8-22) resulted in a stable H_2 permeance of 34.9 m^3/ m^2-h-$atm^{0.5}$, as shown by the Sieverts' law plots in Figure 8-23. More importantly, after a total testing period of ~800 hours at 500°C, the final H_2/He selectivity of membrane 015 remained as high as ~500.

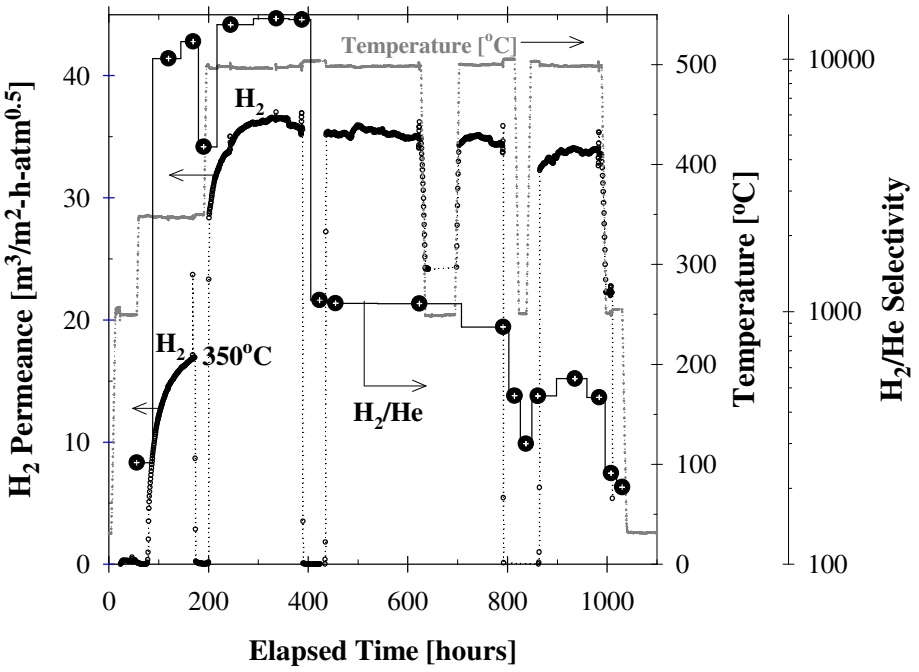

Figure 8-22: H_2 permeance history for the membrane 015 (H_2 permeance: y-axis on the left, Temperature: y-axis on the right and H_2/He selectivity: y-axis on the right offset)

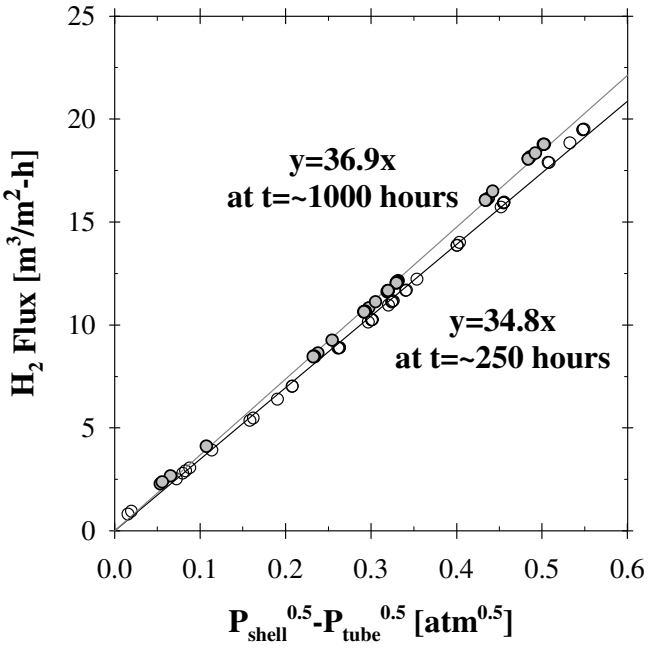

Figure 8-23: Sieverts' law plots for the membrane 015

Coupled with the 4.0 µm thick pure-Ag barrier layer, the Cr-rich oxide-layer formed at 800°C appeared to be extremely effective as an intermetallic diffusion barrier. The Cr-rich oxide layer for the membrane 015 can be seen clearly in the cross-sectional SEI micrograph shown in Figure 8-24.

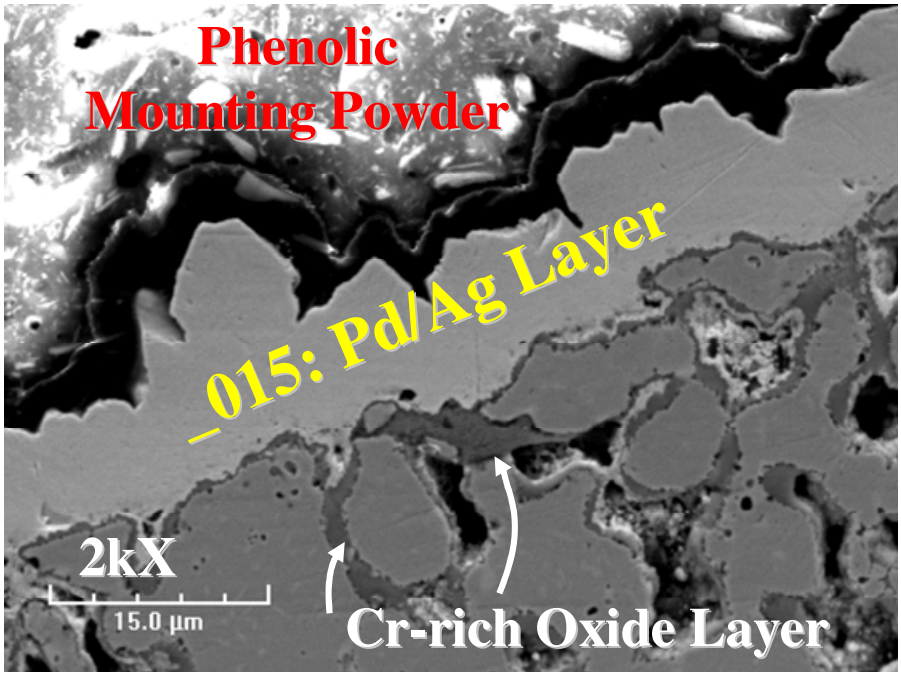

Figure 8-24: Cross-sectional SEI micrographs for the membrane 015

Furthermore, the effect of pure-Ag barrier layer on the thermal stability of membrane 015 was investigated via the EDX cross-section analysis as shown in Figure 8-25.

The interfaces between the support metal and the Pd/Ag layer in line scans A and B of Figure 8-25 were marked at 3.4-4.0 µm and 7 µm, respectively. In both cases, the Ag-rich barrier layer located at the support-membrane interface with a composition range of 20-30 wt% can be easily seen. It is also interesting to note that the region marked between 1.2 and 7 µm in line scan B indicated the presence of a Cr-rich oxide layer.

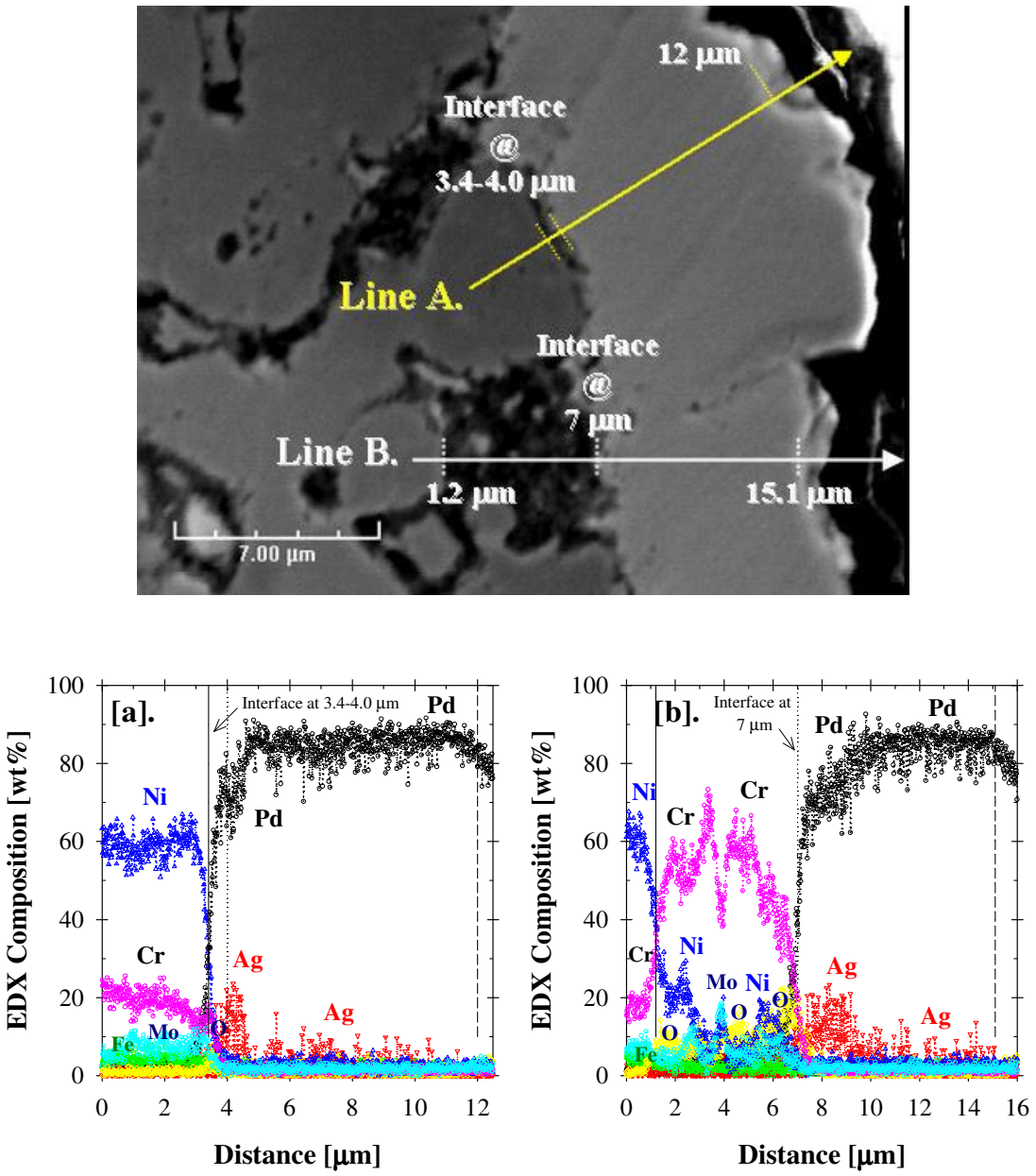

Figure 8-25: EDX cross-section line scans A and B for the membrane 015

The EDX line scans in Figure 8-25 also suggested that beyond the pure-Ag barrier layer, the excess Ag metal was distributed uniformly in the top Pd layer and formed a Pd/Ag alloy phase. The use of both the *in-situ* oxidation and the pure-Ag barrier layer deposition from a concentrated Ag plating bath, provided not only thermal stability over ~1,000 hours, but also, improved leak stability. Indeed, the presence of the oxide layer appeared to help the inter-diffusion to occur only between Pd and Ag metals resulting in

the formation of a relatively uniform Pd/Ag alloy phase throughout the membrane thickness.

8.8. Conclusions

The SEM and XRD analyses of the Pd/PHST, Ag/PHST and Pd/Ag/PHST systems, after high temperature annealing over a temperature range of 500-800°C in H_2 for 20 hours, resulted in similar morphological and phase transformations to that of the thin Pd and Ag deposits on PSS supports.

It was verified by the XRD patterns that the formation of the Pd/Ni alloy phase was started at 500°C. A Pd-rich Pd/Ni alloy phase, which was formed at 600°C, gradually transformed to a pure Ni-rich Pd/Ni alloy phase with the further increase in the annealing temperature to 800°C. Indeed, the formation of the Pd/Ni alloy phase was also evident from the SEI micrographs, which revealed that the morphology of the sample annealed at 800°C was noticeably different than the coupons annealed at lower temperatures (500-700°C).

The immiscibility of the Ag metal with the Ni was also verified by the XRD patterns of the samples annealed in the temperature range of 500-800°C. In order to recapitulate the effectiveness and the stability of the pure-Ag layer as an intermetallic diffusion barrier, the conventional Ag plating bath was modified to improve the deposition morphology and to achieve uniform Ag layers.

The pure-Ag barrier layer was successfully utilized for the syntheis of composite Pd/Ag membranes with Ag contents as high as 40 wt% on un-oxidized Inconel supports modified with the $Al(OH)_3$ grading procedure.

Coupled with the long-term H_2 permeation data for the membranes 014, 018, 019 and 020, detailed cross-sectional SEI and EDX analyses led to a conclusion that the pure-Ag barrier layer was effective against the intermetallic diffusion.

Furthermore, an *in-situ* oxidation study indicated that the formation of a Cr-rich oxide layer for the Ni-rich porous sintered metal supports was possible at an oxidation

temperature of 800°C, as evidenced by the weight gain, surface SEI micrographs and the XRD phase identification analyses.

The combined use of pure-Ag barrier layer, $Al(OH)_3$ grading technique and the support oxidation temperature of 800°C, for the synthesis of 11.6 μm thick Pd/Ag membrane (31.7 wt% Ag), provided a stable H_2 permeance of 34.9 m^3/ m^2-h-$atm^{0.5}$ and a good long-term chemical stability over a period of ~800 hours at 500°C. Indeed, the H_2/He selectivity of the membrane remained as high as ~500 after testing ~800 hours at 500°C.